Inoculation as grain refinement strategy for Wire Arc Manufacturing of Invar 36

Master of Science Thesis

Kevork Perez Bustos

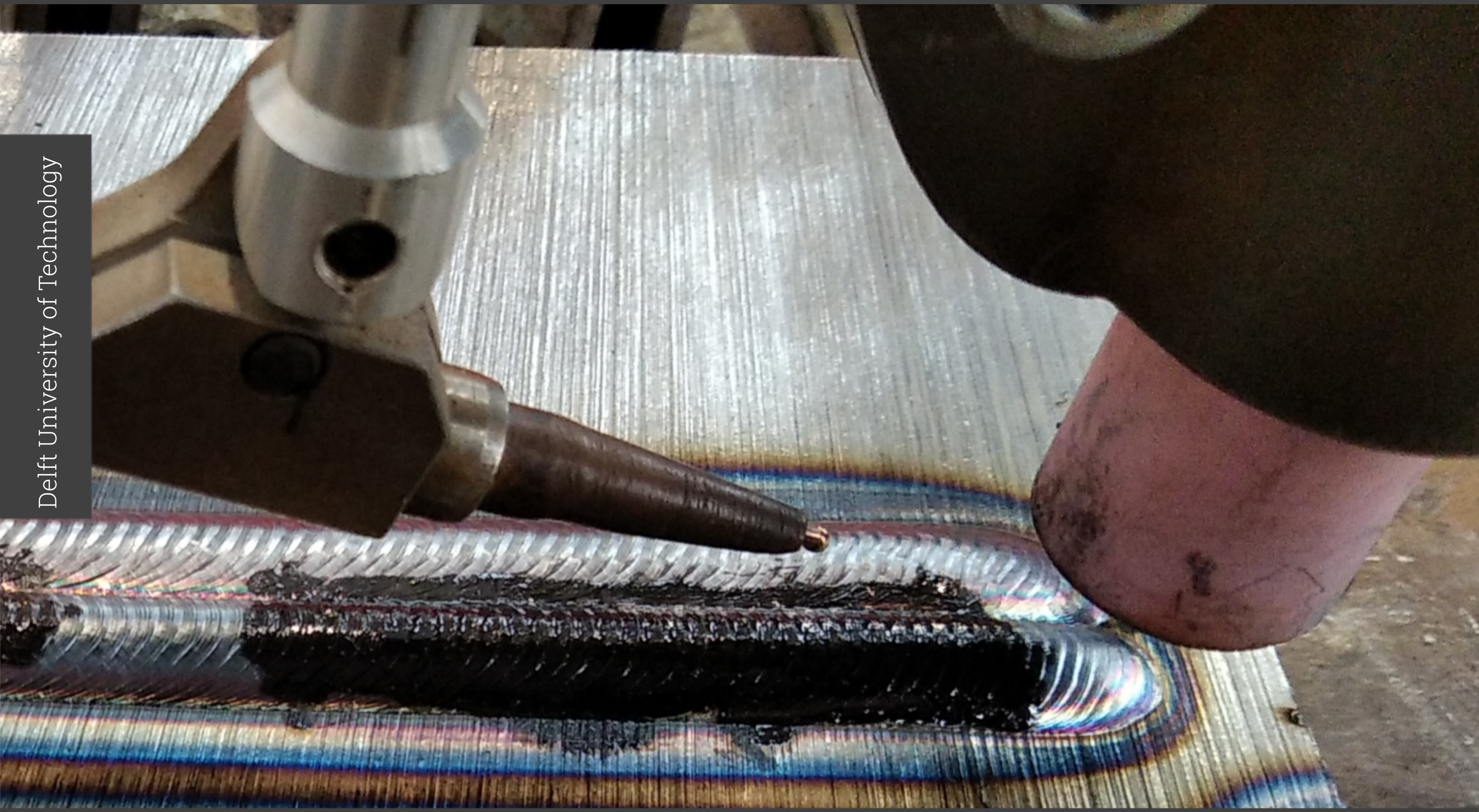

Delft University of Technology

TUDelft

Inoculation as grain refinement strategy for Wire Arc Manufacturing of Invar 36

by

Kevork Perez Bustos

to obtain the degree of Master of Science

at the Delft University of Technology,

to be defended publicly on Tuesday September 26th, 2023 at 1:00 PM.

Student number:	5266491	
Thesis committee:	Dr. M.J.M Hermans	TU Delft, supervisor
	Dr. Vera Popovich	TU Delft, supervisor
	Dr. Erik Offerman	TU Delft
	Ir. Arjun Sood	Tu Delft, daily supervisor

Cover: Partially deposited Invar 36 cuboidal specimen coated with a layer of inoculant-loaded suspensions.

Abstract

Additive manufacturing (AM) refers to a series of techniques in which parts are created by successive deposition of layers. Among the different technologies, Wire Arc Additive Manufacturing (WAAM) employs a welding system in combination with a motion mechanism to deposit layers of molten metal. This technology possesses high deposition rates and an unconstrained build envelope, limited only by the reach of the motion mechanism making it suitable for fabricating large-scale parts. The use of this technique to manufacture technologically interesting materials as Invar 36, a low thermal expansion alloy, could lead to reduced material waste and components with a geometrical complexity only attainable via AM. The high heat input associated with WAAM has been proven to induce columnar grain growth causing anisotropic behavior in the materials, and in the case of Invar 36, it also promotes cracking. In this work, the addition of nucleating agents, known as inoculation, has been implemented during the deposition process to induce grain refinement and mitigate the aforementioned effects. TiC and NbC were selected as possible inoculants based on the results from the implementation of the edge-to-edge matching model as selection criterion. The inoculants, in the form of powders, were mixed with an organic carrier to create suspensions at 50 wt.% and 75 wt.% which then were applied as a coating to each layer during the deposition process. Invar 36 cuboidal specimens with dimensions of 15x15x120 mm were fabricated using GTAW-based WAAM with a heat input of 550 J mm^2. Microstructural characterization showed that specimens with added inoculants achieved significant grain size reduction, reduced crack formation, and an increase in hardness. Defect-free depositions were attained in the specimens with inoculant-loaded suspensions at 75 wt.%.

Acknowledgements

First of all, I would like to thank my supervisors Vera Popovich, Marcel Hermans, and Arjun Sood, for allowing me to carry out this project, for their comprehension, and for their support throughout the whole experience. The knowledge gained here will serve as a strong foundation for the rest of my life.

I would like to offer special thanks to Jurriaan van Slingerland, Remko Seijffers, Durga Mainali, Ruud Hendrikx, and Hans Brouwer for all their support, availability, happy ideas, and for always being willing to lend a hand regardless of the situation. Special thanks to Ton Riemslag and Elise Reinton for the laughs, the support, and the motivation, for allowing me to complement and expand my experience, and above all for giving me the freedom to explore odd solutions to solve complicated problems. My time by your side has been invaluable.

Thanks also to all my friends, colleagues, and special people that I have encountered throughout this journey. I do not dare to try to name all of you. First, because I am afraid I will for sure forget a name, and second because only with your names I could fill this entire thesis. But trust me, I do carry all of you in my memories. Thanks to all of you for the support, for being there, and for always making me smile. Naveen, thanks for always staying by my side.

Finally, thanks Mom, thanks Dad, thanks beloved sisters, thanks Grandma. You have been there during the whole process, you all know the ups and downs. Thanks for always being there for me.

Contents

List of Figures

List of Tables

Nomenclature

Abbreviations

Abbreviation	Definition
AM	Additive manufacturing
ASTM	American Society for Testing and Materials
BCC	Body-centred cubic
CAD	Computer-aided design
CMT	Cold Metal Transfer
CTE	Coefficient of Thermal Expansion
DCEN	Direct current electrode negative
E2EM	Edge-to-edge matching
EBSD	Electron backscatter diffraction
FCC	Face-centred cubic
GMAW	Gas Metal Arc Welding
GTAW	Gas Tungsten Arc Welding
HAZ	Heat affected zone
LMD	Laser Metal Deposition
MGB	Migrated grain boundary
PAW	Plasma Arc Welding
Ra	Surface roughness
SEM	Scanning electron microscope
SLM	Selective Laser Melting
SGB	Solidification grain boundary
SSGB	Solidification subgrain grain boundary
STL	Standard tessellation language
WAAM	Wire Arc Additive Manufacturing
WFR	Wire feed rate
XRD	X-ray diffraction
XRF	X-ray fluorescence

1

Introduction

1.1. Motivation

Additive manufacturing (AM) refers to a series of techniques in which parts are manufactured by successive deposition of layers [1]. In comparison with traditional manufacturing, AM allows for less material waste, high design flexibility, and easy customization and tailorability of components [2]. With nowadays technologies, it is possible to employ AM to produce components out of polymers, ceramics, metals, and composites. However, AM is a relatively new concept and there are still numerous limitations. The exact limitations and their severity, depend on the technology and material being used. The most common limitations encountered can be summarized in limited dimensional accuracy, surface roughness, build speed, and build envelope [2, 3].

Among the technologies, Wire Arc Additive Manufacturing (WAAM) is a relatively economical technique that combines a welding system and a motion mechanism to deposit successive layers of weld beads [4]. The high heat input associated with the welding processes allows high depositions rates during the WAAM deposition process (5-30 g min^{-1}), and the build envelope is only limited by the reach of the motion mechanism [4, 5]. These characteristics make WAAM specially suitable for manufacturing large-scale parts and confer the technique a particular technological interest.

However, as with any manufacturing process, WAAM has its own drawbacks and limitations. Based on welding technologies, WAAM presents various major defects found in welding processes. The high amount of energy introduced during the deposition of each layer causes thermal gradients that may result in warping of the manufactured component [6, 7]. Inherent miss-alignment of the layers limits the dimensional accuracy and the surface roughness of the as-deposited part, requiring additional finishing steps. The layer-by-layer nature of the process also creates a direction of preferential heat extraction promoting columnar grain growth, typically aligned with the building direction. Such grain morphology tends to cause anisotropic mechanical behavior in materials and facilitates the formation of cracks during the solidification process [5, 8]. Different grain refinement strategies have been employed to mitigate the formation of such morphology and the detrimental effects on the materials [8–11]. However, the implementation and efficacy of these techniques are dependent on the process-material pair.

Low thermal expansion alloys, characterized for having low coefficients of thermal expansion, comprehend a group of technologically interesting materials for AM. These alloys are typically employed in high-precision applications where dimensional stability is critical for the correct functioning of the components fabricated [12, 13]. Achieving defect-free depositions, while maintaining the low thermal expansion properties, and a desired mechanical behavior, could lead to the fabrication of components with high geometrical complexity, that could not be obtained by traditional manufacturing methods, while reducing material waste and processing-related costs.

Previous studies on low thermal expansion alloys include a feasibility study and processing parameter optimization for gas tungsten arc welding (GTAW) based WAAM for the deposition of Invar 36 [14–16]. Even with optimized parameters, the formation of typical columnar grain morphology and crack formation during solidification could not be mitigated [17]. This works aims to study the effects of inoculation as a grain refinement strategy on the microstructure, during the deposition of Invar 36 using GTAW-based WAAM.

1.2. Report structure

This thesis is comprised of five chapters distributed as follows: Chapter 1 contains a brief introduction indicating the motivation and the general aim of this work. Chapter 2 comprehends a detailed literature review; topics addressed include the basic principles of AM, a detailed description of WAAM processes and their variants, an introduction to Invar alloys and Invar 36, and inoculation as the proposed grain refinement strategy. Conclusions and objectives derived from the literature review are also included in this chapter. Chapter 3 provides a description of the methodology employed for the selection of inoculants and for the fabrication of Invar 36 specimens, and their posterior characterization. The results and the discussion regarding the effects of the addition of inoculants on the microstructure are presented in chapter 4. Finally, conclusions drawn from this work and future recommendations are presented in chapter 5.

2

Literature Background

2.1. Additive Manufacturing

2.1.1. Overview

In traditional manufacturing, there are two approaches to build parts. The first approach is by using formative manufacturing, where near net shape components can be obtained by applying forces aimed to deform and modify the original shape of the raw material. In the second approach, known as subtractive manufacturing, instead of deforming the raw material, it is selectively removed until the desired net shape is achieved [1]. In contrast, the concept of additive manufacturing (AM), refers to a series of processes in which parts are created by means of joining materials in a layer-by-layer fashion [1, 3]. The layers are formed by depositing raw material on top of a substrate, or a previous layer, and fused together using thermal, chemical, or mechanical energy [3].

AM dates back as early as 1984 with the creation and patent of the first stereolithography by Charles Hull [18]. In this process, UV light was used to cure photosensitive polymeric resins into complex 3D shapes. First AM techniques were only capable of producing polymeric parts, but the technological advances have made it possible to develop new processes in which the AM of a broad range of materials is possible. Nowadays, AM of polymeric, metallic, and ceramic materials is possible when the adequate process is employed [18, 19]. AM technologies have been used to produce parts, among others, in fields such as biomedical industry [20–22], automotive industry [23, 24], aerospace industry [23, 25], and energy industry [26].

Even though AM is a relatively new concept, it has reached such broad range of applications due to its advantages. Among the most remarkable features, we can find the freedom in part complexity and design flexibility [2]. Since the parts are built in layers, limitations like the tooling size or the order of operations, both found in traditional manufacturing, are no longer an issue. Complex geometries, based on computer-aided design (CAD) models, can be adjusted, monitored, and manufactured without major complications [2, 3]. Achieving functional prototypes can be done in fewer iterations, saving resources and time. The lack of material removal reduces the waste generation, making the process cost-effective in terms of material usage [3]. In addition, AM can be employed to fabricate parts made out of different materials known as multi-material components. Mechanical properties of components can be improved by creating hierarchical structures during the deposition, and it is also possible to change the composition throughout the deposition to create components with variable properties known as functionally graded materials [3, 19].

The final characteristics of the parts depend on the combination of several aspects like the process selected, the material, the type and quality of the feedstock, and the processing parameters. In this regard, Table 2.1 depicts a summary of the different AM categories, their common names, the heat source employed, and the materials which can be processed.

Table 2.1: Classification of AM processes. Adapted from [1, 2, 27].

AM Process group	Typical commercial names	Energy source	Feasible materials
Vat Photopolimerization	Stereolithography, Digital Light Processing, Solid Ground Curing, Projection Stereolithography	Ultraviolet light	Photosensitive resin, ceramics
Powder Bed Fusion	Electron Beam Melting, Electron Beam Additive Manufacturing, Selective Laser Sintering, Selective Heat Sintering, Direct Metal Laser Sintering, Selective Laser Melting, Laser Beam Melting	Laser, electron beam	Polymers, ceramic and metallic powders
Direct Energy Deposition	Laser Metal Deposition, Direct Metal Deposition, Direct Laser Deposition, Laser Engineered Net Shaping, Electron-Beam Freeform Fabrication, Wire Arc Additive Manufacturing	Laser, elecron beam, electric arc	Metallic or ceramic powders, metallic wires
Binder Jetting	Powder Bed and inkjet Head, Plaster-based 3D Printing	Binder/thermal energy	Polymers, ceramic and metallic powders
Material Extrusion	Fused Deposition Modelling, Fused Filament Fabrication	Thermal energy	Thermoplastics
Material Jetting	Multi-Jet Modelling	Thermal energy	Photopolymeric resins, metals, ceramics, thermoplastics
Sheet Lamination	Laminated Object Manufacturing, Ultrasonic Consolidation	Laser	Plastic, metallic or ceramic foils

2.1.2. Basic fabricating principle

Despite the numerous categories and technologies, the basic steps required for fabricating parts via AM remains the same for all of them. The creation of a part using AM manufacturing can be summarized in an eight-step process (Figure 2.1) [2]. The first step is the creation of a solid 3D model using a computer-aided design (CAD) software [2, 4]; the nature of these processes allow for the creation of complex geometries, which are not feasible via traditional subtractive manufacturing [2].

Once the model is completed, it must be converted into a specific file, typically standard tessellation language (STL), that represents the surface geometry of the model using a grid [2, 4]. The model representation of the file is then sliced into layers. Depending on the slicing strategy, these layers can be of constant or adaptive thickness depending on the requirements and the geometrical complexity. The number of layers and the height of each layer contributes to the final accuracy of the component [4]. With the STL file, the toolpath, defined as the specific route employed by the AM equipment during the layer deposition, is selected. Before starting the manufacturing process, the toolpath is converted to a G-code format. The G-code represents a series of instructions that can be interpreted by the AM system to fabricate the desired parts; it contains, besides the toolpath, other relevant parameters to properly guide the system during the manufacturing process [2, 28].

Before producing any component, the setup of the AM equipment must be performed. In this step, the equipment parameters, among others, travel speed, type of material, layer thickness, and power are specified [2]. Most readily available commercial AM equipment does not require further operation and can function autonomously until the component is completed. The next step involves the part removal from the substrate; some technologies, like Fuse Deposition Modelling, only require to retrieve the part and remove the necessary scaffolding created to support the structure during the manufacturing process [2]. Others, like Binder Jetting, require an additional curing step before the part can be removed [3]. Finally, some technologies require further post-processing steps before their final application [28, 29]. The amount and the nature of said post-processing is also technique dependant. Parts produced using Selective Laser Melting and Direct Laser Deposition may require machining to improve surface roughness; parts produced by Stereolithograpy require UV-light curing; weld-based AM techniques also require further machining to improve final tolerances and surface roughness [2, 3, 29]. Use of heat treatments to modify and improve mechanical properties is also a common post-processing for AM of metallic materials [28]. Only after the required post-processing operations, the part can be employed in the desired application [2].

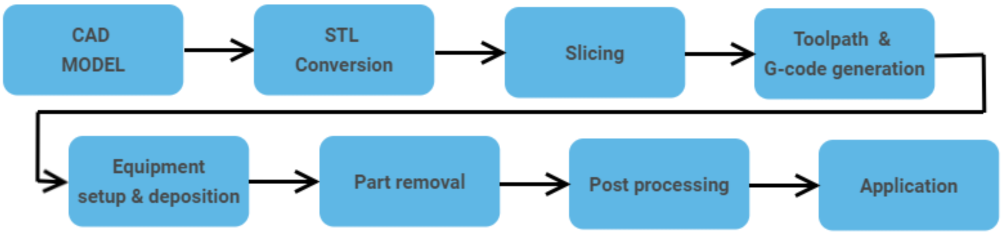

Figure 2.1: Diagram showing the eight steps involved in AM.

2.1.3. Current trends and limitations

Even though AM may offer relatively fast and tailored solutions to the fabrication of components, it is still a process in development and there are still a large number of limitations. Due to the layer-upon-layer nature, surface finish, dimensional accuracy, and maximum resolution are dependant on the technique and technology available [2]. In traditional subtractive manufacturing, typical surface roughness (Ra), after machining, oscillates around 3 μm and it can be further reduced with a finishing cutting pass down to 0.4 µm depending on the equipment used [30]. In AM, Ra is usually higher and comprehends a broad range of values. The final Ra depends on the feedstock, the equipment resolution and the processing parameters. Despite being limited, some AM technologies can achieve comparable Ra to those of traditional subtractive manufacturing. Some examples are Selective Laser Melting (Ra = 5-35 μm), Poly-Jetting (Ra = 3-30 μm), and Stereolithography (Ra = 2-40 μm) [3].

Traditionally speaking, commercial success of AM is owed to the ease of prototyping and creating components in applications where the large flexibility for customisation is preferred over large volume production [3, 31]. Compared to traditional manufacturing, AM has competitive advantage in lead time manufacturing (manufacturing of a component for the first time) of relatively geometrically complex parts [19]. However, the manufacturing cost becomes constant with an increase in the number of parts produced reducing competitiveness with respect to traditional manufacturing techniques [3]. Slow build rates also comprehend an important limitation in AM [3, 18]. Current trends have demonstrated that these limitations can be addressed. Technological innovation and the adoption of operations management practices atypical to AM, as design for volume and low-cost resource deployment, have been employed to achieve high-volume AM using Daylight Photo Printing [31]. Whereas technological innovation is specific of the AM method employed, operations management strategies are transferable. In this regard, the positive outcome of such approach could be use as a guideline to find suitable strategies increasing the output of other AM technologies in a similar fashion.

Limited build volume of some AM technologies also comprises an important limitation. According to the American Society for Testing and Materials (ASTM) [1], the build volume is defined as the total usable volume available in the machine for building parts. Such volume is determined by the characteristics of the equipment. Some technologies, limit their built up volume by constraining the feedstock, like in Powder Bed Fusion, where the maximum part size is given by the size of the powder bed and the range of motion of the AM equipment. Other technologies, where the feedstock is not constrained, like in Fusion Deposition Modelling, are only limited by the range of motion of the AM equipment [2, 23].

Even though modern AM process and technologies can be used to produce parts using a large variety of materials, it is still limited. AM technologies are highly specific with respect to which materials can be employed and further research is required to find adequate combinations of material-process which can be suitable for AM [3]. Furthermore, most of the technologies require a special preparation or, at least, a specific presentation of the raw material. Examples of these are the metallic powders for Metal AM, photosensitive resins, filaments, either metallic or polymeric, ceramic powders, etc. This high specificity of the feedstock also causes it to be more expensive than traditional raw materials [2, 3].

In metal AM, there are also additional limitations which must be taken into account. The production of a component by AM is a complex process in which numerous parameters are involved. Small changes in these parameters may alter the final properties of the component, and thus, the repeatability [2, 3]. Current approaches to overcome this limitation include the implementation of active in-situ monitoring with feedback control [2, 18]. Integration of such systems could allow to perform small adjustments during the manufacturing process, not only making it possible to achieve tighter geometrical tolerances but to increase the build speed without inducing additional defects.

Anisotropy in metal AM corresponds to another important limitation. Each new layer deposited, partially melts the previous one and causes microstructural changes during the solidification process. Furthermore, inadequate parameters selection may also cause an increase in the amount of defects. Due to this, mechanical properties in metal AM tend to differ depending on the direction in which they are measured [2]. The deposition of each new layer also causes rapid heating and cooling of the component being fabricated. With these successive thermal cycles, the components can develop relevant residual stresses which can cause distortion of the component [7, 32]. Both phenomena are currently being addressed by implementation of novel post-processing technologies [3].

Based on the above information, it can be said that, despite current technological advances, AM still has a large number of limitations to overcome. Furthermore, it can also be said that the general trends aim to increase productivity, increase quality and reproducibility of the components and increase the number of feasible materials suitable for AM.

2.2. Wire Arc Additive Manufacturing

2.2.1. Overview

Wire Arc Additive Manufacturing (WAAM) is an AM technology that belongs to the Direct Energy Deposition (DED) process category (Table 2.1). Technologies in this group are characterized, according to the American Society for Testing and Materials (ASTM), by using a directed heat source to simultaneously fuse and melt the feedstock materials while being deposited [1]. As it name indicates, WAAM is a wire-based feedstock technique, which uses electric arc as the heat source. First reports of this technique date back to 1925 with the introduction and patent, by Baker R., of a process that used the electric arc, in combination with metallic wire fillers, to produce ornaments [7]. Nowadays, WAAM has gained terrain in technological applications; several reports can be found where WAAM has been used to produce parts in naval [33], defense [34], aerospace [35], automotive [4], construction [36], and nuclear industries [37].

In its most basic format, a WAAM equipment can be built out of a conventional welding power source and a motion mechanism. Typical motion mechanisms comprise robotic arms or machine tools. Commercial equipment usually include integrated monitoring systems, improved control in terms of degrees of freedom and accuracy, and thermal monitoring systems to ensure the process occurs in optimal conditions [4]. Figure 2.2 depicts a simplified schematic representation of a WAAM process. As can be seen, the torch moves parallel to the previous layer and deposits a new layer of molten metal on top. Once the layer is complete, the torch is moved to the starting point of the next layer and the deposition starts again. Compared to powder-based methods, it can be seen that the build envelope is not limited by a container but by the reach of the motion mechanism [5, 7, 28].

In terms of feedstock material, wire-based technologies present an economical advantage compared to powder-based techniques. Typical feedstock costs for metallic wires are about 10% the cost of equivalent feedstock in metallic powder form, and a wide range of materials is easily obtainable [5]. Furthermore, WAAM possesses high deposition rates (50-130 g/min), and high energy efficiency (>80%) [5, 7]. Such combination of characteristics makes WAAM suitable for manufacturing near net shape, large-scale parts

In general terms, AM manufacturing processes are complex. They require accurate control and precise monitoring of a rather large number of aspects to be able to successfully manufacture components. Alteration of these aspects can cause a negative impact in the final appearance, macrostructure, microstructure, and mechanical properties [4, 28]. Given its relevance, these aspects are briefly intro-

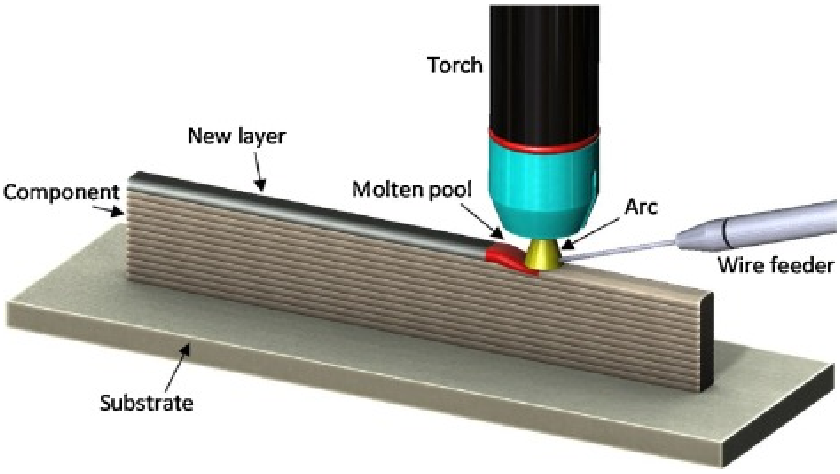

Figure 2.2: Schematic representation of a WAAM process [38].

duced bellow:

2.2.2. Heat input

The layer deposition of WAAM technologies is based on welding processes. Heat input is defined as the relative measure of the transferred energy per weld unit length and it represents one of the critical parameters of the process[5]. The equation 2.1 depicts the relation between the different process parameters that influence the heat input. As it can be seen, the heat input is proportional to the arc voltage (V), the current applied (I), and the thermal efficiency (η); at the same time, it is inversely proportional to the travel speed (TS) [39]. Only a small range of combinations of these parameters can be used to achieve constant and stable deposition [39].

$$Heatinput = \eta \cdot \frac{V \cdot I}{TS} \qquad (J \quad mm^{-1}) \tag{2.1}$$

A process with high heat input implies a large amount of energy deposited. This energy tends to accumulate in the form of heat and causes changes in the material properties; extreme cases can lead to excessive remelting of the previously deposited layers. The region around the weld that undergoes changes is known as the Heat Affected Zone (HAZ) and its microstructure and mechanical properties differ from the base metal [4, 5]. A schematic representation of the HAZ can be found in figure 2.3. A larger heat input creates a larger HAZ; however, If the heat input is too low, it may cause lack of fusion between the layers, uneven deposition, and an increased amount of spattering [4]. Typical industrial applications tend to chose low heat input processes due to the reduced HAZ, lower residual stresses, distortions, and the refined microstructure it provides [5].

A specific value of heat input can be obtained by different combinations of the parameters described in the equation 2.1. Nonetheless, due to the effect of each individual parameter, the morphology of the weld bead deposited will be different. The welding current controls the bead geometry, deposition rate, and fusion depth space[7]. Higher currents are associated with greater penetration, wider weld pool, and higher wetting angle [4]. The arc voltage also affects the bead geometry. High welding voltage induces flatter, shallow, and wider weld pools [41]. High travel speed, defined as the relative

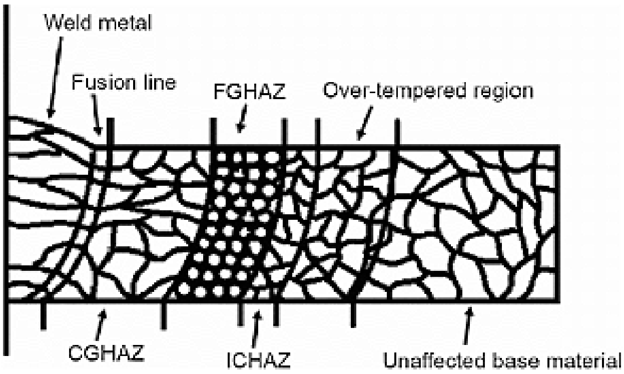

Figure 2.3: Schematic microstructure of the HAZ and the sub-zones formed during the welding process: the coarse-grain HAZ (CGHAZ), the fine-grain HAZ (FGHAZ), and the intercritical HAZ (ICHAZ) [40].

rate of travel between the electrode tip and the base metal, causes a decrease in the wetting angle, penetration depth, metal deposition, and the bead width [7, 41].

2.2.3. Consumables

The welding processes involved in WAAM require shielding gases. The main functions of the shielding gases are protecting the weld bead from oxidation and stabilizing the electric arc. They create a protective environment by displacing the preexisting gasses in the atmosphere and they can be either inert (do not react with the weld pool) or active (react with the weld pool) [42]. Table 2.2 shows the common shielding gases used, their reactivity, and some relevant remarks. Shielding gases can be used alone or as mixtures. Different combinations of gases may produce synergistic effects, improving the quality of the weld bead [7, 42]. The final selection of the shielding gas will depend on the process and the material being deposited [6]. In WAAM, the flow rate of the gas used is also an important parameter. Besides protecting the weld bead, the shielding gas dissipates the heat accumulated through forced convection. With proper selection of flow rate and gas type, the process can be optimized in terms of energy dissipation to avoid overheating of the component, bead geometry, and penetration depth [39, 43].

The feedstock, in form of wire, corresponds to the other consumable required. Without taking into account the composition, the most important parameters of the feedstock are the wire diameter and the wire feed rate (WFR). The wire diameter affects the deposition accuracy, the weld bead geometry, and the penetration depth. For a given set of parameters, a smaller wire diameter will achieve deeper penetration and a narrower weld bead. Additionally, wires of smaller diameter posses higher electrode-melting rate since they require less energy to melt, leading to an increased deposition rate for a set heat input [39, 42]. The WFR affects the deposition rate and the layer height. For a given heat input, higher WFR creates layers with increased aspect ratio and increased amount of material deposited per layer [39].

2.2.4. Path planning

Path planning refers to the series of instructions the equipment will follow to create the desired part, and it comprises two parameters. The first parameter is the slicing of the 3D model. In WAAM technologies, this process follows the same steps described in section 2.1.2 [7, 39]. The second parameter,

Table 2.2: Common shielding gases used in welding processes.

Gas	Reactivity	Remarks
Argon (Ar) [44, 45]	Inert	○ Most common gas employed due to low cost and can be used for most of materials ○ Reduced electrical resistance compared to He which implies lower operating voltage ○ Well suited for thin metals ○ Ionisation potential of 16 eV
Helium (He) [44, 45]	Inert	○ Approximately three times the price of argon ○ Ionisation energy of 25 eV ○ Requires higher gas flow due to lower density ○ Welding speed approximately 35-40% faster ○ Less penetration depth than Ar ○ Typically used in combination with Ar to improve arc stability
Carbon dioxide (CO_2) [44]	Active	○ Only used for welding ferrous metals ○ Similar penetration characteristics to those of He ○ Produces small amounts of oxygen in the metal ○ Sensitive to arc length due to electrical resistance ○ Requires currents approximately 20-30% higher than when Ar or O_2 is used
Oxygen (O_2) [44]	Active	○ Can be used up to a 10%, higher concentrations will yield porosity ○ Less penetration depth than CO_2 ○ Enhances arc stability ○ Reduces surface tension of the molten pool
Hydrogen (H_2) [45]	Active	○ Can lead to embrittlement ○ Increases arc temperature ○ Produces deeper penetration depth and higher welding speeds ○ Creates a slightly reducing atmosphere
Nitrogen (N_2) [44, 45]	Active	○ Used to weld high conductivity metals ○ Transfers more energy than Ar and He ○ Cannot be used with steels due to nitrogen pick-up ○ Commonly used as a carrier or mixing agent

the path strategy, defines how the material will be deposited onto these layers. It includes the external boundaries, the infill pattern, and the tool path instructions to complete the layers [39]. Different strategies can be used depending on the part geometry and complexity. Figure 2.4 depicts some examples of tool paths [7, 43].

2.2.5. Post processing

During the manufacturing process of a component by WAAM, each new layer deposited induces a thermal cycle on the layers below. These thermal cycles cause microstructural modifications, thermal fatigue, residual stresses, and distortions [6]. In order to mitigate these effects and obtain the desired functionality, post processing thermal treatments can be implemented [46]. The characteristics of the heat treatments used will depend on the material and the final properties desired. Typical heat treatments include thermal stress relief, annealing, solutionizing, and corresponding precipitation treatments [46]. The thermal treatment can also be applied while inducing isostatic-pressure in a treatment called Hot Isostatic Pressing (HIP). The addition of pressure reduces porosity related with internal

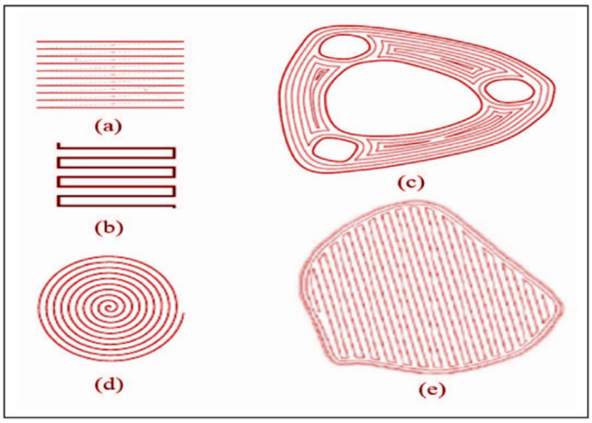

Figure 2.4: Schematic representation of different possible toolpaths. (a) Raster, (b) Zig-zag, (c) Contour, (d) spiral, (e) Hybrid [7].

defects which improves mechanical properties, reproducibility, and results in extended lifetime of the component [47].

WAAM is a near net shape process. After a part is manufactured, it requires additional steps to reach the desired properties [4]. Typically, traditional machining processes are used to adjust the dimensional tolerances, reduce surface roughness, and improve the surface finish of the material [4, 47]. Moreover, extra processes can be applied to further improve the quality of the component. Implementation of residual compressive stresses on the surface and sub-surface by ultasonic impact treatments and peening have been proved to increase the mechanical properties of WAAM components [4]. However, as it is the case with the heat treatments, the final selection of machining operations and additional treatments will depend on the material and final application.

2.2.6. Process variants

Deposition of layers in WAAM is done by melting the wire feedstock using an electric arc produced by a welding torch. These torches, each with their own features, can be based on Gas Metal Arc Welding (GMAW), Gas Tungsten Arc Welding (GTAW), or Plasma Arc Welding (PAW) [5, 39]. Figure 2.5 shows an schematic representation of the aforementioned process variants.

Gas Metal Arc Welding-based WAAM

In GMAW-based WAAM, the electric arc is formed between a consumable electrode and the substrate. This electrode, in the form of a wire spool, is continuously feed in a concentric manner through the torch by a feeding mechanism [6]. Depending on the voltage-current configuration, four different basic metal transfer methods, namely short-circuit, globular, spray, and spray pulsed, can be achieved [6, 39, 48]. GMAW-based WAAM has a high heat input and can reach average deposition rates up to 3-4 kg/hour [39]. The high heat input of these modes produces a large weld pool, limiting the wall thickness and the surface finish. These limitations can be overcome, up to a certain measure, by using more complex transfer modes. These modes implement cyclic changes in the current, voltage, and can include complex coordinated movement of the electrode [44, 48]. Cold Metal Transfer (CMT) is an example of a complex transfer mode in which the electrode moves back and forth in a precise motion, allowing for careful detachment of the molten metal droplet [42]. In doing so, it can achieve high

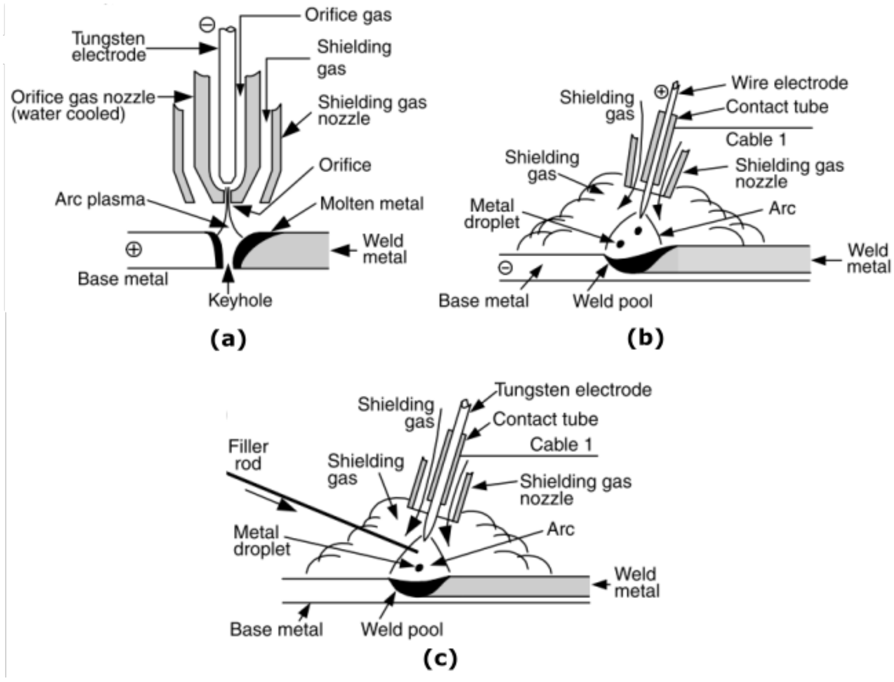

Figure 2.5: Schematic representation of welding torches: (a) PAW, (b) GMAW, and (c) GTAW. Adapted from [8].

deposition rates with a relatively low heat input [39, 42, 48].

Gas Tungsten Arc Welding-based WAAM

Contrary to GMAW-based WAAM, in GTAW-based WAAM, the electric arc is formed between a non-consumable tungsten electrode and the work piece [6]. The high amount of heat produced in GTAW may cause partial melting of the tungsten electrode, contaminating the weld pool [6]. The process yields an average deposition rate of 1-2 kg/hour and the feeding process occurs separately from the arc generation process. This fact allows GTAW to employ different wire feed orientation which influence the quality of the deposit [39, 48]. For Ti- and Ni-based alloys positioning the wire at the leading edge allows for higher feeding rate and produces better surface finish [48]. However, it has also been reported that feeding the weld pool from the back end is is more efficient and stable for aluminium [48]. Therefore, the exact effect of the wire orientation is material dependent.

Plasma Arc Welding-based WAAM

PAW-based WAAM also uses a non-consumable tungsten electrode. However, the electric arc is produced between the electrode and a constricted nozzle inside the torch instead of between the electrode and the substrate [6]. This contraption causes the hot zone of the plasma to be narrower than the ones found in GMAW and GTAW processes making it able to produce narrower weld beads, and has a average deposition rate of 2-4 kg/hour [48]. The energy produced by the plasma can exceed three times the energy produced by GTAW processes causing less distortions and smaller HAZ [39, 48]. In a similar fashion to GTAW-based WAAM, the feeding also occurs separately of the arc generation. In this regard, different electrode orientations are also possible in PAW-based WAAM [39].

2.2.7. Current limitations and challenges

WAAM is a relatively new technology, which means there are still numerous challenges and limitations. While certain factors are material specific, there are other common limitations and challenges which are inherent of the process [4]. WAAM utilizes welding techniques for the material deposition, therefore, typical defects encountered in welding can also be found in WAAM parts. During the welding processes, contaminants are volatilized and can dissolve into the weld pool. During the solidification, the difference in gas solubility forces the gases out of solution but they can get trapped forming porosity. The pore size can vary between microscopic scale to macroscopic and will depend on the presence of contaminants, and processing parameters [4, 7, 43].

Cracking and delamination are also common welding related defects encountered in WAAM. Cracking can occur in grain boundaries owing to variation in dissolution or formation of precipitates. Solidification cracks occur due to hindrance of grain growth or due to high strains created by the thermal gradients [4, 7]. Solid-state cracking is also possible in some materials and it is caused by different mechanisms. Some examples are ductility dip cracking and post-weld heat treatment cracking. Ductility-dip cracking occurs by a sharp reduction in ductility in some materials which, in combination with the thermal stresses of the process, causes the formation of cracks [47, 49]. In contrast, post welding heat treatment cracking can occur during any post processing heat treatment and its associated with the formation of precipitates [47]. Delamination, defined as the decohesion of layers, occurs due to insufficient temperature to induce proper layer re-melting [4]. Current research aims to reduce these defect to a minimum. Typical approaches include the implementation of substrate pre- and postheating, interpass rolling, and lowering the cooling rates [7].

Parts manufactured via WAAM possess a dimensional inaccuracy along the build direction called the ”stair-stepping effect” and it occurs due to an inherent miss-alignment of the layers along the build direction (Figures 2.6d and 2.6e). The magnitude of this defect is related to the layer thickness and reduces the accuracy of the deposited material [7, 48]. Surface roughness is another limitation of WAAM. Parts are manufactured by depositing a certain number of weld beads side by side; in order to create a structural-sounding component, these beads must be deposited with enough overlapping to create a continuous layer. Owing to this, bead geometry plays an important role. Dimensional accuracy is limited to ±0.2 mm and the surface roughness is limited to 200 µm [48]. Inconsistency in the wire feeding can also affect the final dimensional accuracy. If the feeding is not continuous, unmelted wire sections of the wire can get on the surface of the component (Figure 2.6b) [43]. Because of these reasons, WAAM is considered a near net shape process and requires additional post processing [7, 48]. Current approaches to mitigate these defects include appropriate selection and optimization of tool path, slicing strategy, and process parameters [7, 48].

The high amounts of heat transferred to the substrate owing to the high heat input, represents another relevant limitation of WAAM [6]. During the deposition process, the component being manufactured suffers from thermal expansion and contraction. Since this process is not homogeneous throughout the part, strain gradients are formed. These gradients may create residual stresses that can develop into warping of the component (Figure 2.6c) [4, 48]. Furthermore, the continuous accumulation of heat in combination with low heat dissipation may also cause side collapses (Figure 2.6a). Both of these phenomena are particularly important in large parts [7].

During the manufacturing process, the heat accumulated can also cause microstructural changes. Solidification rates are decreased a sa consequence of the heat accumulation and may induce columnar grain growth along the heat extraction direction [5]. This preferential grain growth enhances the inherent through-thickness anisotropy, characteristic of WAAM processes (Figure 2.6f) [7]. While there are some possible solutions to mitigate the microstructural evolution, not all of the techniques can be implemented to all materials, nor all geometries [9, 10]. In the following sections, this issue will be addressed in detail for the material considered.

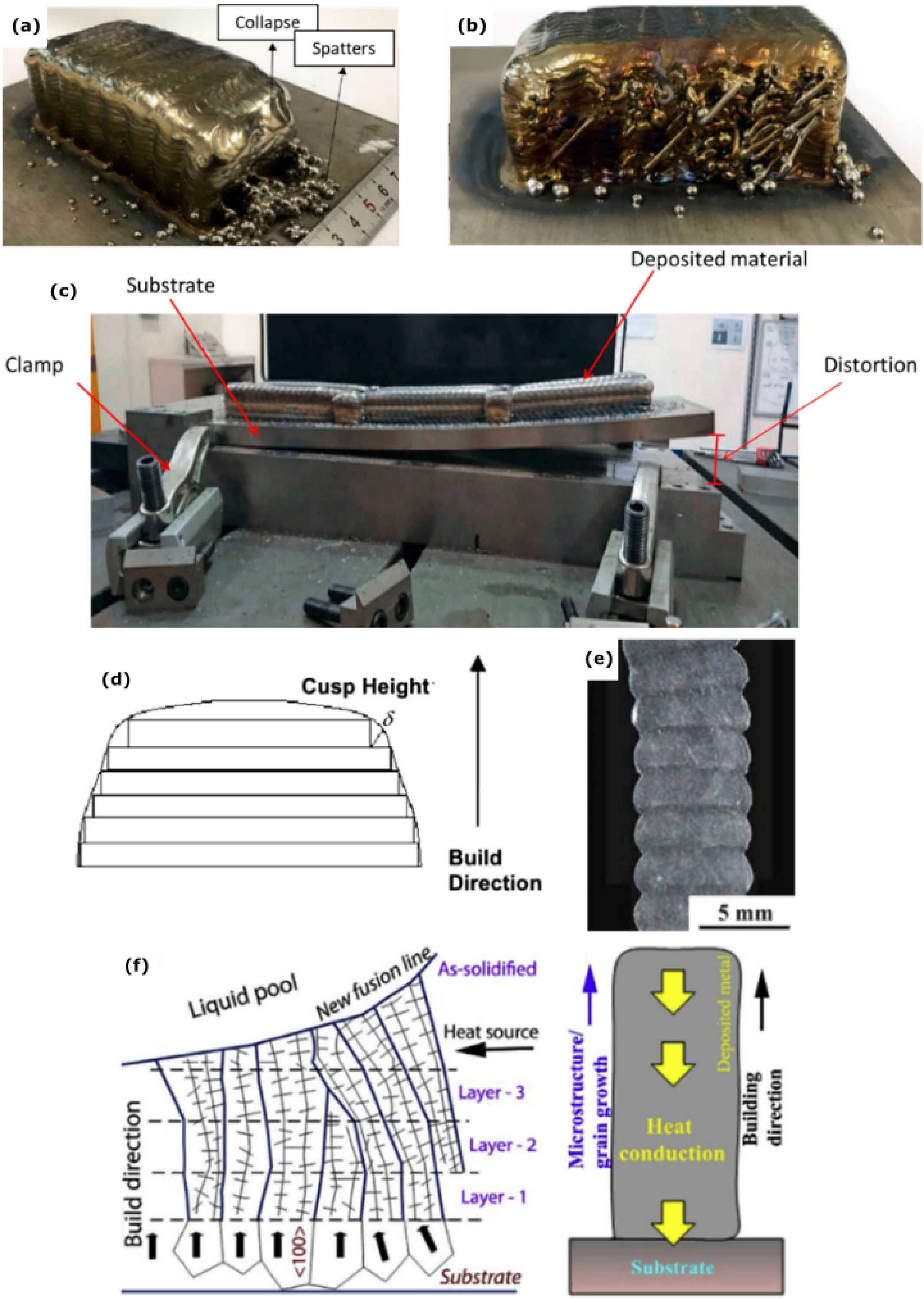

Figure 2.6: Common defects and limitations in WAAM. (a) Wall collapse and spatter [43], (b) unmelted wire sections stuck to the side of the part [43], (c) distortion of as-deposited component due to thermal gradients [43], (d) Schematic representation of the stair-step defect [48], (e) single bead wide wall, notice the stair step defect [5], and (f) schematic representation of the columnar grain growth due to preferential heat conduction direction [5].

2.3. Invar Alloys

2.3.1. Introduction and Invar effect

Invar alloys are metallic alloys characterized for having an extremely low coefficient of thermal expansion (CTE) over a wide range of temperatures around room temperature [12, 50]. This phenomenon was named ”the Invar effect” and it was discovered in 1861 by Charles Guillaume while studying the influence of composition on the CTE in the iron nickel system ($\mathrm{Fe}_{1-x}\mathrm{Ni}_x$). During his experiments, Guillaume reported a discontinuity in the CTE behaviour around the 30% Ni content. In the Fe-Ni system, the nickel acts as an austenitic stabilizer. Above 30% content in nickel the austenite becomes stable at room temperature and the crystalline structure of the alloy changes from body-centred cubic (BCC) to face-centred cubic (FCC). The change in microstructure also induces a change in the magnetic behaviour and the alloy becomes ferromagnetic. Further studies reported the behaviour of the CTE as function of the temperature. It was discovered that above the Curie temperature, the anomaly in the CTE disappeared and the material returned to have a normal behaviour [50, 51].

The change in the magnetic properties of the material and the recovery of the normal behaviour above the Curie temperature, suggested that the anomalous behaviour and the magnetic properties were correlated [12]. In ferromagnetic materials, a decrease in temperature increases the magnetic moment due to an alignment of magnetic domains. Magnetic properties are crystalline-orientation dependant, meaning that there are some preferential orientations which require less energy to align. Thereby, the material structure will be rearranged to align along these preferential orientations in order to reduce the free energy of the system. Since different crystalline orientations have different interplanar distances, its alignment will induce a small strain in the system; this phenomenon is called ”positive volume magnetostriction” [12, 52]. If its magnitude is large enough, it can counteract the conventional thermal-related expansion and contraction, yielding a material with almost no dimensional change upon heating or cooling [52].

Whereas it has been proved that the low CTE is the result of a strong positive volume magnetostriction, the origin of such magnetostriction is still in debate. Early studies assumed that the Invar anomaly was directly related with iron-rich systems, ferromagnetic behaviour, and with an FCC crystalline structure. This hypothesis have been proved to be wrong. The Invar anomaly has been observed in crystalline and amorphous materials, in structures different from FCC, in alloys without the presence of iron, in alloys with antiferromagnetic behaviour, and in ordered and disordered alloys [53, 54].

In the specific system of Fe-Ni Invar alloys, the first model intended to describe this phenomenon was proposed by J. Weiss. This model, named the two γ state, was based on thermodynamic calculations taking into account numerous iron alloys. In it, Weiss proposed the existence of two magnetic states within the FCC structure of the material, namely γ_1 and γ_2, These configurations have their own volume, energy associated, and magnetic moment. Out of the two, γ_1 refers to antiferromagnetically coupled iron atoms and this phase is characterised by a low magnetic moment and a low volume, but possess a higher energetic state. In γ_2, the iron atoms are ferromagnetically coupled and the behaviour is the opposite, i.e. high volume, high magnetic moment, and low energetic state [12, 50, 55]. According to this model, γ_2 corresponds to the ground state of the alloy owing to its lower energetic state. Thus, thermal excitation will induce a phase transformation from γ_2 to γ_1. In the process, the thermal expansion will be counteracted by the volume change due to the phase transformation and the change in magnetic moment from one phase to the other [55]. This model inspired further research and has been proved to be in good agreement with the observed experimental data. In fact, it was discover that the ground state is not only formed by one phase alone, γ_1 and γ_2 coexist in a mixed ground state [50].

2.3.2. Invar 36

Invar 36 is an Invar alloy which belongs to the Fe-Ni system and has a Ni content of 36 wt.%. The average complete composition is depicted in the table 2.3. Among the Invar alloys in the Fe-Ni system, Invar 36 possesses the lowest CTE with a nominal value of 1.58$\times 10^{-6}$ strain/$^\circ$C. Compared to regular alloys, which posses a CTE around 10^{-5}, the Invar 36 alloy deforms one-tenth (1/10) of the deformation occurred in conventional alloys per degree celcius [12]. Its high dimensional stability makes it ideal for high-precision applications as space equipment, automobile components and sensing equipment [12, 13, 56].

Table 2.3: Average composition of Invar 36 (wt.%). Si, C, and Mn are present as impurities. Data extracted from [57].

Alloy	**Fe**	**Ni**	**C**	**Mn**	**Si**
Invar 36	62-65	35-37	0-0.1	0-0.6	0-0.35

The intrinsic microstructure of Invar 36, depicted in figure 2.7, is relatively simple, it consists of a single phase that corresponds to an FCC Fe-Ni solid solution. The FCC structure confers the Invar 36 an excellent ductility, but it also possess relatively low hardness (147 HV), and limited mechanical properties [13, 56]. Common values of the mechanical properties, for traditionally manufactured Invar 36, include: yield strength between 230 and 350 MPa, and tensile strength between 400 and 500 MPa [56].

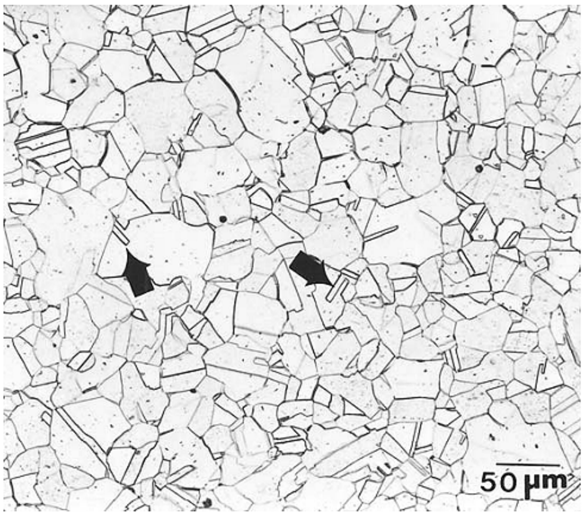

Figure 2.7: Typical microstructure of Invar 36 consisting of single FCC phase (austenite); arrows indicate annealing twins [58].

Traditional manufacturing of Invar 36 components is carried out by machining. The high ductility, in combination with the low hardness value, and pronounced work hardening, makes machining an expensive and complicated process [13, 15]. In this regard, AM offers an interesting technological opportunity. The reduced machining involved in additive manufacturing, due to the fact that it is a near-net shape process, could simplify and reduce costs in producing Invar 36 parts.

Concerning the effect of the processing method on the microstructure, and therefore the material properties, there have been numerous successful attempts to study the feasibility of producing Invar 36 parts via AM. Qiu et al. [13] employed selective laser melting (SLM) to additive manufacture Invar 36 specimens. The authors studied the influence of the scanner speed on the porosity and the microstructural evolution. In their results, they reported that under the right processing parameters, specimens with low porosity (<5%) can be successfully manufactured. The microstructural study revealed columnar grains oriented along the build direction of γ phase, decorated with nano precipitates of α phase. Texture analysis also revealed a preferential orientation of the <001> direction (figure 2.8). Mechanical testing showed an important anisotropy component due to the microstructure, and dependant on the build direction. Finally, studies on the CTE showed that despite being higher, it is still comparable to traditionally manufactured Invar 36.

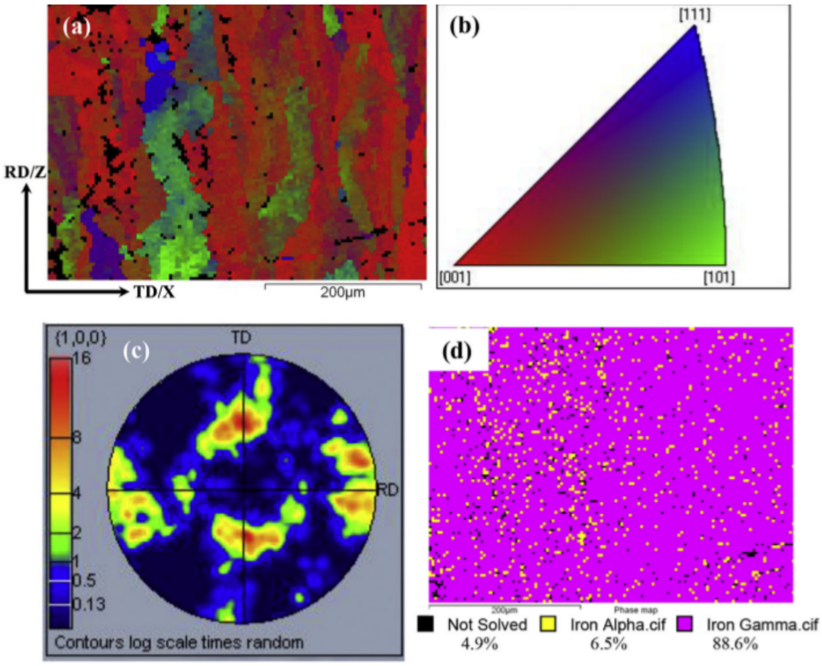

Figure 2.8: Results of texture analysis performed by Qiu et al. (a) EBSD image showing the as-deposited microstructure by means of SLM; (b) and (c) showing the inverse pole figure and pole figure obtained from EBSD mapping, respectively; (d) EBSD phase map showing the distribution and area fraction of different phases. The building direction is along Z direction [13].

Based on the work of Qiu et al., Harrison et al. [59] carried out further research on the effect of SLM processing parameters on the CTE of Invar 36. After optimization of the parameters, the authors managed to produce near-full-density components (>99.96%) with mechanical properties comparable to those of cold-drawn Invar 36. However, a microstructure composed of through-thickness columnar grains was still observed (figure 2.9a). Contrary to the work of Qiu et al., Harrison et al. reported additive manufactured Invar 36 specimens with a lower CTE than conventionally manufactured Invar 36.

Wei et al. [60] studied the influence of the scanning strategy on the microstructural evolution and mechanical properties. In their study, the authors employed SLM with an ”island scanning strategy” in order to reduce the residual stresses created during the manufacturing process. They reported that, under the proper conditions, the as-fabricated specimen showed a density of 99.5%, Vickers hardness of 1.8 GPa, and ultimate tensile strength of 480 MPa, values comparable to conventionally manufactured Invar 36. The microstructural analysis reported results in accordance with the previous studies commented. In a follow up study, Yang et al, [61] employed the method used by Wei et al. and performed a systematic characterization of the CTE and microstructure. X-ray diffraction (XRD) patterns revealed only the presence of austenite. The lack of BCC α phase peaks was attributed to the low relative concentration with respect to the austenite. Columnar grains along the building direction were again reported (figure 2.9c). Lastly, the CTE reported, with a value of 1.72-1.96 $\times 10^{-6}$ strain/°C, is slightly lower than conventionally manufactured Invar 36.

Besides SLM, laser metal deposition (LMD) has also been employed to produce additive manufactured Invar 36 components. Li et al. [62] carried out a study on the microstructural evolution and mechanical properties of additive manufactured Invar 36 using LMD. In their results, they reported having fabricated fully dense Invar 36 components with columnar grain structure. It was also reported that the size of the columnar grains decreased gradually along the building direction (figure 2.9b). Furthermore, the preferential crystal orientation of the columnar grains was discovered to be dependant on the heat extraction direction. Finally, Li et al. also reported to have achieved better mechanical properties in comparison with cast and wrought Invar 36 alloys.

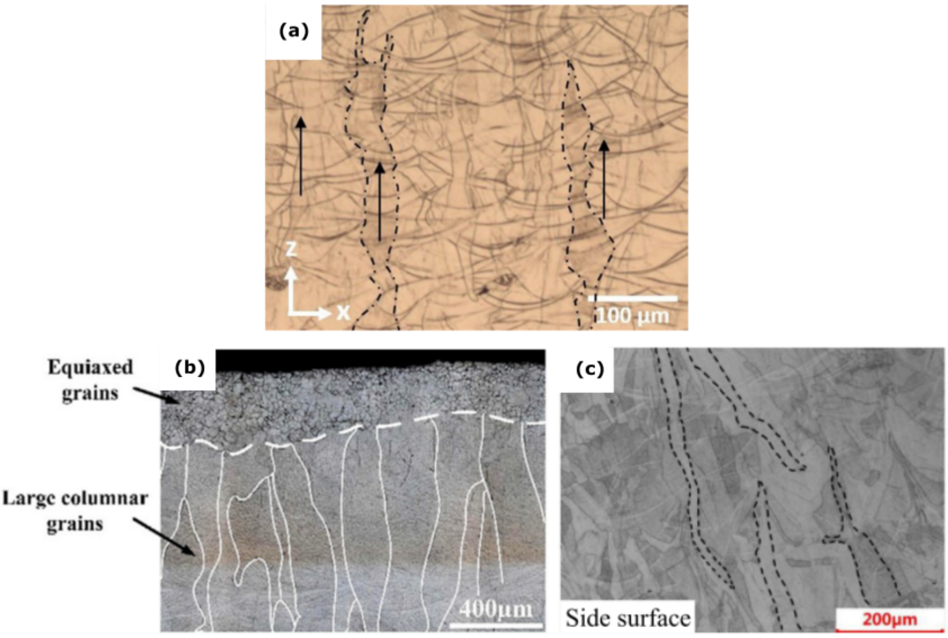

Figure 2.9: Microstructural morphologies of Invar 36 as reported by different authors: (a) Columnar grain growth morphology aligned with the building direction (Z) produced by SLM [59]; (b) Columnar grain growth and equiaxed grain morphology near the surface produced by LMD [62]; (c) Columnar grain growth morphology oriented along the building direction and produced by SLM [61].

Whereas many researches have been conducted using laser as the heat source for additive manufactured Invar 36 components, there is little research in the use of WAAM for the same purpose. Fowler et al. [14] carried out studies to determine the feasibility and optimal parameters for the deposition of Invar 36 using GMAW-based WAAM equipment. The experiments consisted in a series of systematic tests to determine the optimal deposition parameters for single beads, walls, tubes, infill patterns, and overhang components. The CTE of the as-printed specimens was also characterized. Despite being higher than the traditionally manufactured Invar 36, with a reported value of 3.5 $\times 10^{-6}$ strain/°C, the CTE still remained within acceptable values for high precision applications (figure 2.10). Veiga et al, [15] studied the effect of processing parameters on the bead geometry and implemented a monitoring system for the weld pool. The experimental procedure consisted of the utilization of a GMAW-based

WAAM equipment to produce single bead depositions on top of a substrate using different parameters. With the results obtained, the authors developed a regression model to determine the optimal processing parameters to achieve optimal and symmetric depositions. Under the proper conditions, a symmetry of 99% was reported. Finally, with the optimized parameters, a wall of 100 mm height and approximately 10 mm wide was manufactured with a symmetry of 99.8%. Figure 2.11 depicts the deposited wall.

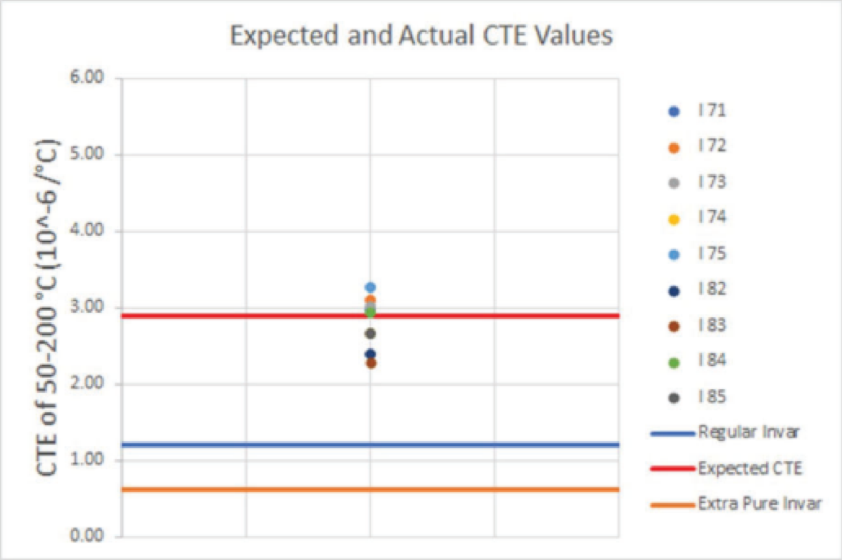

Figure 2.10: CTE of the as-manufactured Invar 36 walls as function of their height, produced by WAAM [14].

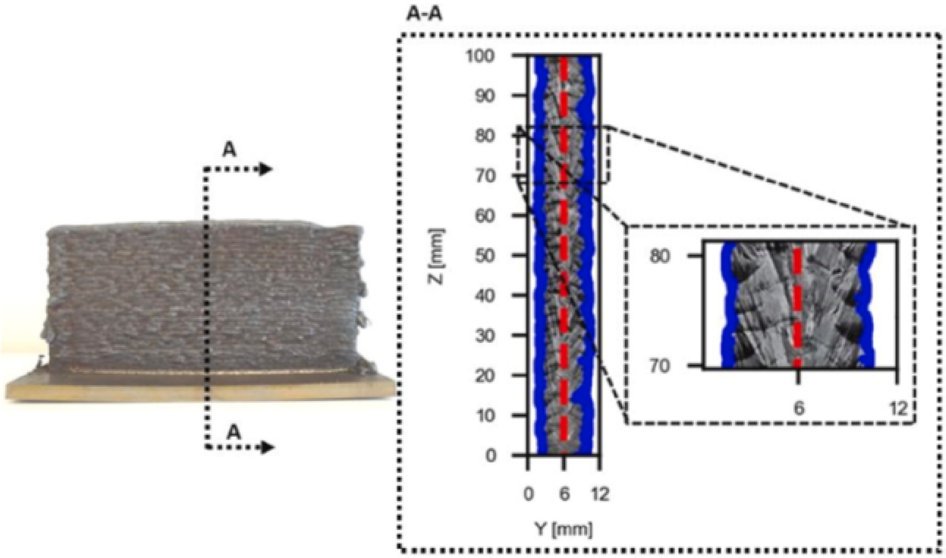

Figure 2.11: Invar 36 wall manufactured by means of WAAM. The deposition was carried out according to the optimized parameters found by the authors [15].

2.4. Grain Refinement

2.4.1. Typical microstructural morphology in WAAM

WAAM is a fusion welding-based process, meaning that the general behaviour of the solidification mechanisms and defects are similar to traditional welds. The substrate on top of which the metal is deposited acts as a nucleation surface. During the solidification process, the atoms will arrange on top of the substrate keeping a constant orientation and following a growth direction aligned with the heat extraction direction (typically perpendicular to the travel direction). This kind of growth is called epitaxial growth and the predominant crystallographic orientation developed is related to the ”easy-growth” direction of the crystallographic system [8]. Table 2.4 depicts the easy-growth direction for the most common crystallographic structures. If the microstructure of the substrate differs from the material being deposited, the new grains formed may or may not hold an orientation relation with the substrate depending: (1) on the phases present and (2) the planes parallel to the surface, but contrary to epitaxial growth, the grain orientation will be mostly random as a result of heterogeneous nucleation in the weld pool [8].

Table 2.4: Easy growth directions of common crystal structures [8].

Crystal structure	Easy-growth direction	Examples
Face-centred-cubic (FCC)	$< 100 >$	Aluminium alloys, austenitic stainless steels
Body-centred-cubic (BCC)	$< 100 >$	Carbon steels, ferritic stainless steels
Hexagonal-closed-packed (HCP)	$< 10\bar{1}0 >$	Titanium, magnesium
Body-centred-tetragonal (BCT)	$< 110 >$	Tin

This directional grain growth, in combination with the induced texture, have a significant effect on the mechanical properties and creates anisotropy in the material. At the same time, this microstructural morphology has been correlated with an increased susceptibility to solidification cracking. Fine equiaxed grains can accommodate the solidification stresses by deforming in an easier manner than columnar grains, thus reducing the possibility of cracking. Additionally, equiaxed microstructures contain a larger grain boundary area which allows distribution of the low-melting-point segregates that can be formed during the solidification process, which also reduces the possibility of solidification cracking [8].

In essence, WAAM can be considered as a successive deposition of weld beads on top of each other. Each new layer deposited, unless manufacturing dissimilar metals, will share the same crystalline structure, meaning that the epitaxial grain growth will occur throughout the entire component manufactured. Moreover, not only mechanical properties will be affected; preferential orientation of grains also affects functional properties as the CTE and corrosion resistance. In this regard, the implementation of grain refinement strategies offers a potential path to address this issue and improve the final component performance.

Numerous strategies have been successfully implemented in grain refinement, such as interpass rolling, electromagnetic stirring, arc pulsation, and forced convection. However, inducing plastic deformation via interpass rolling is limited to simple geometries and may be limited by the size of the component; a similar argument can be made for forced convection [9, 10]. The case of electromagnetic stirring and arc pulsation is slightly different, while its application is not limited by geometry, nor size, these parameters are extremely sensitive and may be complicated to control during the deposition processes [9]. Based on this, this literature review will focus on inoculations as grain refinement strategy, which can be applied to any part geometry and size.

2.4.2. Inoculation as grain refinement strategy

Inoculation can be defined as the addition of inoculants or nucleating agents into the weld pool. The inoculants, typically in the form of fine powders, act as nucleation centres and promote heterogeneous nucleation. The increased number of nuclei formed hinders the grain growth and produces a fine, equiaxed microstructure morphology [8]. The presence of inoculants can also locally alter the composition of the alloy which translates in variation of the material properties. The effect produced on the material, in terms of properties and microstructural morphology, is dependent on the inoclulant-substrate pair [8].

Since the effect of the inoculants is dependent on the specific inoclulant-substrate pair, the appropriate selection is not often evident. As aforementioned, the main objective of the inoculants is to promote heterogeneous nucleation across the whole molten material by increasing the number of nucleation sites. How well inoculants promote heterogeneous nucleation is referred to as the potency of the grain refiner [63]. According to the nucleation theory in solidification processes, heterogeneous nucleation is promoted when the energy on the newly formed interface between the substrate and the inoculant is lower than the energy of an equal area formed only by the substrate [32]. Quantification of these interactions and determination of interfacial energies is often a complex process. However, it has been demonstrated that good atomic matching across the interface is sufficient criterion for the formation of low-energy interfaces [32, 63, 64].

In an attempt to predict these interactions, numerous models have been created [32]. Among the models, the edge-to-edge matching model (E2EM) offers the advantage of giving a selection criterion based on only crystallographic parameters. The model assumes that there is a correlation between the orientation and morphology of two phases and the minimization of interfacial energy. Based on this assumption, the model establishes that the only necessary conditions for an inoculant to behave as a potent inoculant are the existence of matching rows of atoms across the interface, and that these rows must consist on close-packed or nearly close-packed crystalline directions. This model does not refer to atomic matching positions across close-packed planes but to the atomic matching positions across the interface of closed-packed or nearly closed-packed planes, along closed-packed or nearly close-packed directions [32, 63]. Figure 2.12 shows a schematic representation of the difference between both considerations.

In order to implement the model, only the crystallographic information of the species considered is necessary. The first step consists in the determination of the matching directions. This is done by finding the closed-packed or nearly closed-pack directions of both phases by calculating the atomic linear density. Then, the interatomic misfit between these directions is determined pair wise; if the interatomic misfit is less than a threshold value of 10%, it is possible that an orientation relationship between the two phases exist, meaning the resulting interfacial energy will be low enough to promote

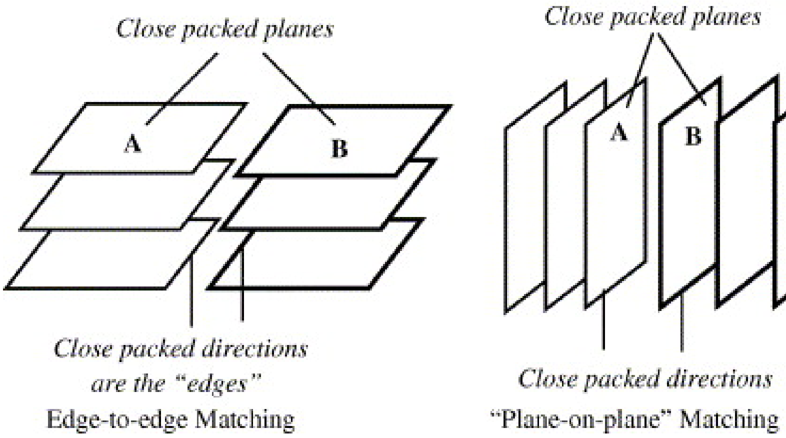

Figure 2.12: Schematic representation of the difference between edge-to-edge matching and plane-on-plane matching [32].

heterogeneous nucleation [32]. The next step involves finding the matching planes and the mismatch between interplanar distances of both phases. The matching planes are defined as the close-packed or nearly close-packed planes that contain the matching directions. Again, the criterion establishes that misfits under 10% are likely to form orientation relationships implying low interfacial energy, promoting heterogeneous nucleation. Both conditions must be met simultaneously for considering an inoculant as a potent inoculant [32].

Despite the simplicity of the model, the results predicted have been confirmed by several studies. Zhang et al. [32] employed the model to determine LaB_6 as a potent inoculant for $AlSi_{10}Mg$ alloys. With the information extracted from the model, the author employed nanoparticles of LaB_6 to manufacture fined-grained components with isotropic properties using SLM technologies. In a separate study, Li et al. [65] also identified LaB_6 as a potent inoculant for ferrite steels based on the E2EM. The addition of LaB_6 resulted in reduced equiaxed grain size and reduction in the fraction of columnar grains.

The misfit determined by the model can also be used as a relative measurement of the potency of an inoculant. In this regard, Zhang et al. [32] employed the E2EM to determine the feasibility of using TiC, Al_3Ti, TiB_2, and AlB_2 as inoculants for grain refinement in aluminium alloys. According to the results, the four possible inoculants actively behave as grain refiners, nonetheless, Al_3Ti presented the lowest misfit. According to the model, the lower the misfit implies lower interfacial energy, meaning that the refining effect of Al_3Ti should be larger than the other possible inoculants studied. The results predicted by the model were in agreement with the experiments carried by the author.

The E2EM model has shown good accuracy in predicting new grain refiners for several alloys. However, it is important to highlight that the model is based merely on the crystallographic information of the species. It has been stated and demonstrated that good atomic matching between the phases is criterion enough to predict the creation of new interfaces with lower interfacial energy, and thus inducing heterogeneous nucleation. Notwithstanding, the model does not take into account the possible interactions between the substrate and the inoculant. Reactivity of the inoculant with the substrate, possible dissolution of the particles in the molten liquid, formation of unforeseen phases, and local alteration of the composition are some key aspects that should be considered for the final selection of the inoculants. Furthermore, the E2EM model only predicts the feasibility of an inoculant to act as a grain refiner; It does not offer insights regarding the possible process parameters involved as the minimum concentration of the inoculant, size of the particles, influence of cooling rates, or influence on the molten pool behaviour due to the presence of the inoculants.

2.4.3. Use of inoculants in AM

Use of inoculants for microstructural refinement has been studied in many applications including AM processes. Langelandsvik et al. [66] employed TiC nanoparticles to successfully achieve grain refinement in aluminium alloy 5183 produced by WAAM. The addition of the inoculants was performed by mixing the particles with granules of aluminium alloy 5183 wire feedstock. The coated granules were then extruded into a new wire feedstock coated with TiC nanoparticles. As it can be seen in the figure 2.13, the effects orbserved include strong grain refinement (reduction in 93% of the grain area) and an increase in the mechanical properties due to the combined effect of grain refining strengthening and particle strengthening. In another study, Wang et al. [10] employed stripes of Al-5Ti-1B as grain refiner for WAAM of Al-Mg alloy. The stripes were added between layers of material deposition. The microstructural analysis revealed effective grain refinement in the samples containing the Al-5Ti-1B stripes. Further analysis revealed the formation of Al_3Ti phase in the matrix of the aluminium alloy. This phase holds a mismatch with the aluminium matrix of less than 5% meeting the necessary conditions for grain refinement according to the E2EM model, and Al_3Ti could be used as a potent grain refiner by its own. Finally, in agreement with previous studies, enhanced mechanical properties and ductility were reported [10].

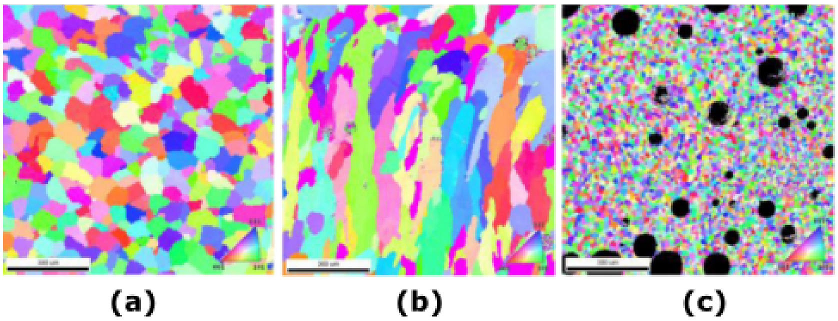

Figure 2.13: EBSD map of aluminium alloy 5183 (a) commercially acquired, (b) deposited using WAAM, and (c) Deposited using WAAM and mixed with TiC. Adapted from [66].

Zhai et al. [67] and Yin et al. [68], studied the effect of inoculants on the microstructure and mechanical properties of SS 316 L produced via SLM. Yin et al. employed W particles as grain refiners. The implementation method was by simply combining the the SS 316 L powder with the W powder until achieving a homogeneous distribution. The authors reported a significant grain refinement and increase in mechanical properties. With a 10 wt.% of W, an increase of 50% in the yield strength while keeping a 19% elongation was achieved, nonetheless, precipitation of ferrite was also detected. Aditionally, the authors also concluded that the addition of W particles improves the corrosion resistance of the alloy. However, large concentration of W particles lead to precipitation of ferrite, therefore, the W wt.% is not proportional to the corrosion resistance [68]. Zhai et al. employed Ti powder in combination with SS 316 L powder to form mixtures with differente Ti wt.%. As depicted in the Figure 2.14, the microstructural analysis showed that Ti has a powerful refining effect on SS 316 L. The average grain size was reduced with an increased Ti wt.% content and no undesired intermetallic phases were observed. Mechanical properties were also reported to increase with finer microstructure. However, reduced ductility was also reported and attributed to a suppression of twinning-induced plasticity mechanisms

[67].

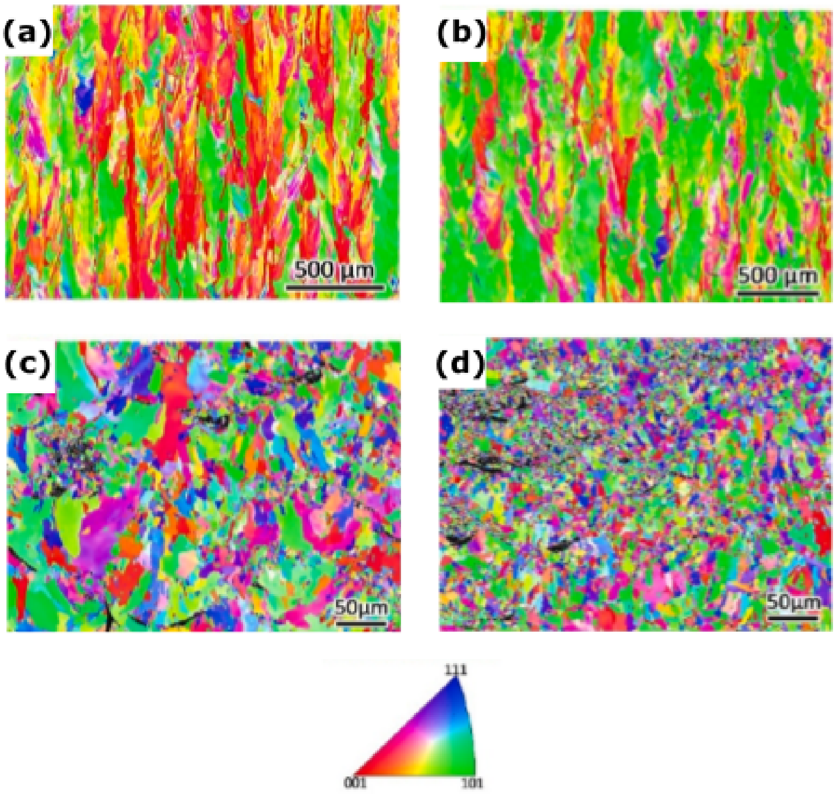

Figure 2.14: EBSD map of SS 316 L alloy specimens produced by SLM with (a) 0, (b) 0.3, (c) 1, and (d) 1.5 Ti wt. %. Adapted from [67].

2.5. Conclusions

AM is a powerful technology that allows manufacturing of parts with high degree of freedom with respect to the part complexity. Its working principle allows it to produce, modify designs, and deposit components with relative ease, saving time and resources. Among the technologies, WAAM combines high deposition rates (5-30 g min^{-1}), high material deposition efficiency (>80%), and a large build envelope making it ideal for manufacturing large-scale parts. However, due to its near-net-shape nature, components manufactured require additional post-processing steps before their final application.

The typical through-thickness columnar grain microstructural morphology of WAAM processes, represents one of the major limitations of the technique. Such morphology results in anisotropy of mechanical and functional properties, and facilitates crack formation during solidification. While this behaviour could be tailored for specific applications, typical industrial applications require homogeneous and isotropic materials.

Mitigation of the columnar grain growth forms part of the challenges being faced by WAAM. Current approaches involve optimization of process parameters, implementation of post-processing heat treatments, and incorporation of additional strategies. While optimization of the processing parameters may aid in reducing the columnar grain formation, there is still an inherent orientation relationship between each deposited layer and the previous one that will induce epitaxial growth. The implementation of post-processing operations, while effective, adds another step to the manufacturing process, increasing production time and costs. It could be argued that the incorporation of grain refining strategies would also lead to an increase in costs and time. Nonetheless, incorporation of these strategies during the deposition process could result in components with a more favorable microstructure without requiring additional post-processing steps besides the usual machining operations.

Based on the feasibility of including the refining strategies during the deposition process, and taking into account that the strategy selected must be compatible with the process, stable throughout the entire deposition, and applicable to the size and geometry of the part manufactured, inoculation has been selected as the most suitable grain refinement strategy.

Grain refinement via inoculation has been reported in powder-based processes and in WAAM. The incorporation of inoculants in powder-based processes is carried out by mixing the inoculants in the desired quantities with the substrate. In WAAM, according to the literature consulted, the method for adding the inoculants varies depending on the author. Some of them include coating the feedstock wire with the inoculant, co-extrusion of the feedstock with the inoculant, placement of inoculant stripes on top of the substrate, direct incorporation of the inoculant into the weld pool, and creating suspensions with the inoculants and placing them on top of the substrate. This diversity in the application method indicates a knowledge gap in the optimal way of adding the inoculants.

The effectiveness of an inoculant depends on the substrate-inoculant pair. Adequate selection of inoculants and finding new inoculants can be complicated. In this regard, the E2EM model has been proven to be a simple, yet effective, tool to predict possible new grain refiners. However, only the use of the model is insufficient to guarantee grain refinement. The model is based on crystallographic information only, and it fails to provide insights regarding metallurgical aspects. Interactions between the inoculant and the substrate are not accounted for and, despite having a positive prediction according to the model, an inoculant may not act as a grain refiner. Although, a thorough search yielded no further relevant correlations between the model predictions and metallurgical aspects that could aid in the final selection of inoculants, the implementation of the model remains being a good starting point for the selection of new inoculants.

As in traditional manufacturing, in AM there is a tight material-process correlation. Based on this, Invar 36 was chosen as the study object for this work. This alloy is characterized for having an extremely low CTE with a value of 1.58$\times 10^{-6}$ strain/$^{\circ}$C and is commonly used in applications requiring high dimensional stability.

Microstructural characterization of Invar 36 components manufactured via WAAM, revealed the characteristic columnar grain growth and the heavy texture inherent to this process. Despite the heavy texture, the degree of anisotropy, understood as the difference between the reported properties depending on the direction, differed throughout the different studies consulted.

The knowledge gaps encountered can be summarized as follows: There is little research regarding the use of WAAM for fabricating Invar 36 components. While it has been successfully deposited, the characteristic columnar microstructure has not been mitigated. Additionally, no reports were found where the WAAM has been used in combination with inoculation to improve the microstructure and reduce crack formation during solidification. Finally, there is no consensus with respect to the optimal way to incorporate inoculants into the manufacturing process.

2.6. Research objectives

Based on the conclusions drawn from this literature review, the following objectives were formulated in order to bridge the existing knowledge gap:

- Implementation of the E2EM model for the selection of possible inoculants for Invar 36.
- Implementation of inoculation as grain refinement strategy during the deposition of Invar 36 using GTAW-based WAAM.
- Characterization of the microstructure to determine the effects of the added inoculants on the grain morphology, grain size, presence of defects, and phases present.

3

Materials and Methods

3.1. Implementation of the E2EM model

As mentioned in the section 2.4.2, inoculants with less than 10% mismatch between close-packed or nearly close-packed directions and less than 10% mismatch between close-packed or nearly close-packed planes, with respect to the substrate, have been proved to act as efficient inoculants. It is important to highlight that the directions considered must be contained within the aforementioned planes. The table 3.1 shows the close-packed and nearly close-packed directions and planes for the different systems considered. Based on this information and the description of the E2EM model provided by Zhang et al. [32], a MATLAB script was written to determine the misfit between Invar 36 and the different possible inoculants considered.

Table 3.1: Miller indices of close-packed and nearly close-packed directions and planes for the crystalline structures considered [32, 69].

Crystal structure	Directions	Planes
FCC	<1 1 0> <1 0 0> <1 1 2>	{1 1 1} {2 0 0} {2 2 0}
BCC	<1 1 1> <1 1 0> <1 0 0> <1 1 3>	{1 1 0} {1 1 2} {1 2 3} {0 2 1} {1 1 1} {2 0 0}
HCP*	<1 1 0> <0 0 1> <$\overline{1}\overline{1}$ 1> <2 1 0>	{1 0 1} {1 0 0} {0 0 1} {1 1 0}
FCC (rock salt)	<1 0 0 > <1 1 0 > < 1 1 1>	{2 0 0} {2 2 0} {1 1 1}

* Indices for the HCP structure are expressed in Miller notation

Since the model is based on crystallographic information, the crystalline structure and the lattice parameters of each specie must be known and entered as inputs for the script. The model then determines the interatomic distance based on the equal-ratio method proposed by the author Fang et al. [70]. This method calculates the interatomic distance between atoms using analytical geometry principles and has the advantage that can be used for any crystallographic system, arbitrary directions, and does not require an auxiliary representation of the model to visualize the atomic distribution [70]. According to this method, any distance between two atoms can be determined according to the equation 3.1, where $d'_{[uvw]}$ corresponds interatomic distance from the atom (u, v, w) to the origin of the primary lattice of the crystal, also referred to as ”the interatomic spacing period”, and $1/r$ corresponds to the interatomic spacing coefficient and it is a correction coefficient that allows calculating the correct interatomic distance of structures with more than a single atom per unit cell. The specific solutions for the FCC, BCC and HCP crystalline structures, can be seen in the table 3.2.

$$d_{[uvw]}^{(1/r)} = d'_{[uvw]}/r \tag{3.1}$$

Table 3.2: Interatomic spacing coefficient and interatomic spacing for the different crystalline structures considered [70].

Crystal structure	u, v, w	Interatomic spacing coefficient ($1/r$)	Interatomic spacing ($d_{[uvw]}^{(1/r)}$)
FCC	Two odd, one even	1/2	$(u^2+v^2+w^2)^{(1/2)}a/2$
	All odd	1	$(u^2+v^2+w^2)^{(1/2)}a$
	Two even one odd	1	$(u^2+v^2+w^2)^{(1/2)}a$
BCC	All odd	1/2	$(u^2+v^2+w^2)^{(1/2)}a/2$
	Mixed	1	$(u^2+v^2+w^2)^{(1/2)}a$
HCP	u = 6e + 4 v = 6 f + 2 w = 6g + 3	1/6	$[(u^2+v^2-uv)a^2+w^2c^2]^{(1/2)}/6$
	u = 6e + 2 v = 6 f + 4 w = 6g + 3	1/6	$[(u^2+v^2-uv)a^2+w^2c^2]^{(1/2)}/6$
	The others	1	$[(u^2+v^2-uv)a^2+w^2c^2]^{(1/2)}$

The interplanar distance is then calculated by means of the equations depicted in the table 3.3. Both sets of calculations (interatomic distance and interplanar distance) are performed for all the close-packed or nearly close-packed directions and planes of both species, the inoculant and the substrate. The resulting interatomic distances are compared pairwise, and the mismatch between them is determined as depicted in the equation 3.2. In a similar fashion, the mismatch between the interplanar distances is determined (equation 3.3). The script then sorts the calculated mismatch and creates a matrix containing the possible directions and planes with a mismatch of equal or less than 10%.

$$\Delta_{direction} = \frac{d_{(uvw)matrix} - d_{(uvw)inoculant}}{d_{(uvw)matrix}} \tag{3.2}$$

$$\Delta_{plane} = \frac{d_{(hkl)matrix} - d_{(hkl)inoculant}}{d_{(hkl)matrix}} \tag{3.3}$$

Table 3.3: Interplanar distance for different crystalline structures [71].

Crystal system	Interplanar distance
Cubic	$d_{hkl} = \frac{a}{(h^2+k^2+l^2)^{(1/2)}}$
Hexagonal	$d_{hkl} = \frac{a}{\sqrt{\frac{4}{3}(h^2+k^2+hk)+\frac{a^2}{c^2}l^2}}$

As above mentioned, the directions must be contained within the plane. For a given family of directions, the interplanar distance is the same due to the crystal periodicity, the same occurs with the family of planes. However, not every direction is contained in every plane. To determine whether a direction is contained in a plane or not, the dot product between the direction and the plane is calculated. If this product returns a value of zero, it means the direction and the plane are orthogonal to each other, and since planes are described by their normal vector, being orthogonal implies the direction is contained within the plane. The script performs this operation for every possible direction-plane combination and returns only those who comply with the condition. Results are then reported as a matrix containing the corresponding direction-plane pair for the substrate and the inoculant, and the corresponding mismatch. A copy of the source code can be found in the appendix A.

3.2. Deposition of Invar 36 specimens with added inoculants

3.2.1. Experimental setup

Depositions were carried out using pulsed current GTAW-based WAAM. The equipment consisted of a power source Migatronic TIG commander 400 AC/DC operating in Direct current electrode negative mode (DCEN) mode, a Migatronic KT4 wire feed unit, and a 3-axis motion system. Tungsten electrodes type E3 (mixed with rare earths) with a diameter of 3.2 mm and a tip angle of 40° were employed. Argon with a purity ≥ 99.999% was used as shielding gas at a flow rate of 10 L/min.

Process parameters and deposition strategy were selected according to a previous study on the deposition of low thermal expansion Invar alloys using WAAM in which the authors performed a parameter optimization to accomplish defect-free depositions of Invar 36 alloys [16]. According to the results reported, even with the optimized parameters, only the specimens deposited with a heat input of 200 J mm^{-1} resulted in defect-free depositions. For the rest of the heat inputs, the specimens showed the presence of cracks, and the crack length showed a tendency to increase with an increase in the heat input. As mentioned in the chapter 2.4 grain refinement not only reduces the anisotropy in the material but also allows to accommodate solidification stresses, mitigating crack formation. Based on the assumption that grain refinement can be achieved by the proposed method for the highest heat input, lower heat inputs should yield similar results. the specimens were deposited using a heat input of 550 J mm^{-1}. A complete summary of the parameters can be seen in the table 3.4. As per the deposition strategy, weld beads were deposited unidirectionally along the X-axis, further referred to as the weld direction (WD), with front feeding of the filler wire. In addition, the following remarks were also taken into account for this work: The filler wire was positioned so it remained suspended in between the electrode and the substrate to mitigate lack of fusion; the height of the welding torch with respect to the workpiece was checked after each layer was deposited to ensure constant arc length and maintain the desired weld-bead geometry [16].

3.2.2. Incorporation of inoculants

As stated in the chapter 2.4.3, while the use of inoculants has been implemented in AM, there is no consensus regarding the optimal way of incorporating them during the deposition processes. Some of the strategies discussed include coating the filler wire, placing metallic thin-films on top of the deposited layer, and even direct mixing of the inoculant with the substrate in the case of powder-based

Table 3.4: Process parameters employed for the deposition of Invar 36 specimens [16].

Parameter	Value	Parameter	Value
Base current	135 A	Travel speed	3.3 mm s^{-1}
Peak current	150 A	WFR	49.5 mm s^{-1}
base time	0.2 s	Heat Input	550 J mm^{-1}
Peak time	0.2 s	Hatch distance	68 %
Arc voltage	11.9 V	Interpass temperature	80-100 ° C

AM technologies. Despite achieving grain refinement, implementation of these strategies may result in complicated logistics or, in the case of powder mixing, unsuitable for WAAM. In the specific context of WAAM, some authors have explored and accomplished grain refinement by mixing the inoculant powder with a carrier agent to form a suspension and applying it as a thin coating on top of the deposited layer [72, 73]. The carrier agent then is burned by the high temperatures produced during the deposition process and only the inoculants are incorporated into the weld pool. Owing to its relative simplicity this incorporation strategy was employed in this work.

The possible candidates to act as grain refiners (table 3.5) according to the E2EM model implementation were acquired and mixed with an ARALDITE® 2028-1 ISOCYANATE two-component adhesive, manufactured by Huntsman Corporation. A detailed description of the selection process can be found in the chapter 4.1.2. As above mentioned, the function of the adhesive is to act as a carrier for the powder, therefore, the powders were only mixed with the polymer and not with the catalyst to avoid undesired curing and, consequently, hardening of the suspension. A common remark highlighted by the authors Kennedy et al, [73], and Bermingham et al. [72] was to keep the amount of carrier to a minimum to keep the concentration of the inoculants as high as possible maximizing the grain refinement, and minimizing possible weld pool contamination during the burning of the adhesive. However, in an attempt to determine the potency of the possible inoculants, suspensions with a 50 wt% and 75 wt% inoculant content were prepared. The procedure followed to create the suspensions consisted of weighing the corresponding amounts of adhesive and inoculant on a plastic tray and mixing them thoroughly until achieving a homogeneous suspension.

Table 3.5: Acquired inoculants for Invar 36 alloys.

Inoculant	Manufacturer	Average particle size [μm]	Purity
NbC	Nanografi	1-3	99.95%
TiC	Sigma Aldrich	44	98%

As discussed in chapter 2.4.2, grain refining by the addition of inoculants is dependent on the inoculant-substrate pair. According to the previous work consulted on the deposition of low thermal expansion Invar alloys, the nickel content during the deposition of the first two layers is lower than the nominal composition of the Invar 36 alloy due to dilution with the substrate [16]. To ensure the reported effects of inoculant addition are only due to the interactions between the Invar 36 alloy and the inoculants, the suspensions were incorporated only after the second layer where the nickel concentration stabilizes to the nominal Invar 36 composition.

3.2.3. Manufacturing specifications

To keep consistency with the previous work consulted, cuboidal multi-layer specimens with a cross section of 15x15 mm and a length of 120 mm of Invar 36 were deposited on top of an SJ690 structural steel plate. The filler wire used for all the depositions was a 1.2 mm in diameter, 3Dprint AM Mold 36, Invar 36 alloy, manufactured by Voestalpine Böhler Welding. Compositions for both, the filler wire and substrate can be found in tables 3.6 and 3.7 correspondingly.

Table 3.6: Composition of wire filler 3Dprint AM Mold 36 as stated by the manufacturer in wt.%.

Alloy	C	Si	Mn	Cr	Mo	Co	P	S	Ni	Fe
Invar 36	0.05	<0.1	0.2	<0.50	<0.50	<1.0	<0.01	<0.01	34-38	Bal.

Table 3.7: Composition of structural steel S690 in wt.%.

Alloy	C	Mn	P	S	Cu	Ni	Fe
S690	0.17	1.4	0.035	0.035	0.55	0.012	Bal.

For the addition of the inoculants, the specimens deposited were subdivided into two regions of 55 mm starting from opposite extremes. Each of those regions was then coated with a different concentration of inoculant-loaded suspension. This methodology facilitated the manufacturing of the different specimens, saving time and material. The 10 mm remaining at the center of the cuboidal specimens were left uncoated to avoid cross-contamination between the two concentrations. A schematic representation of the specimens deposited can be seen in the figure 3.1.

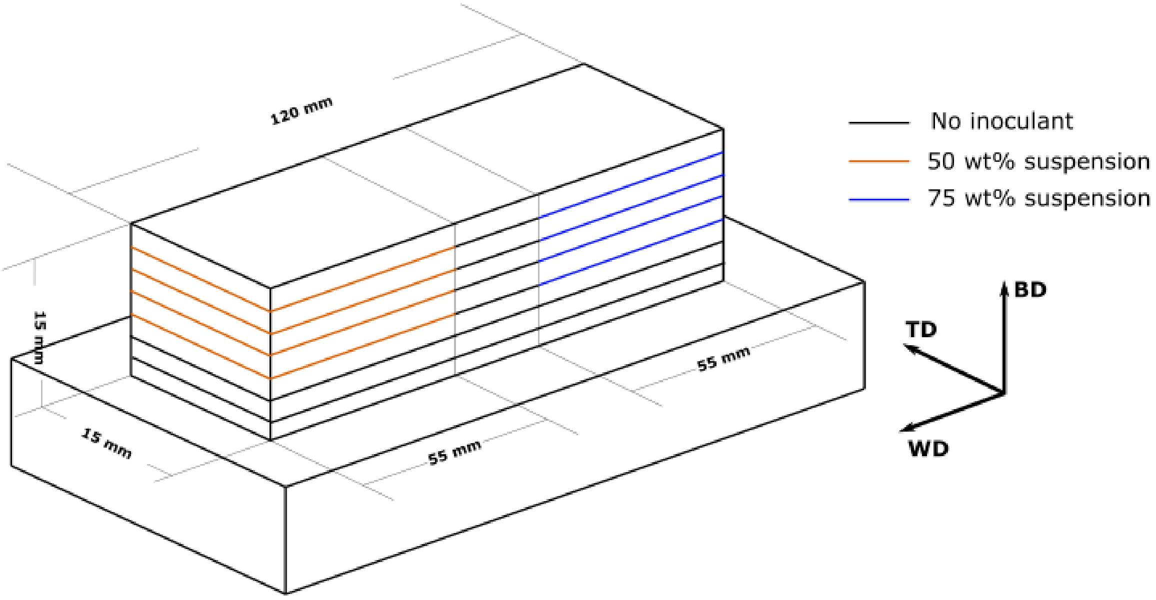

Figure 3.1: Schematic of deposited specimens. The Reference system indicates the build direction (BD), the transverse direction (TD), and the welding direction (WD).

3.3. Microstructural characterization

In order to verify the homogeneity of the process and the effects of the added inoculants, two transverse cross sections were extracted from each concentration deposited. To ensure the metallographic samples are representative of a stable deposition process, the transverse cuts were made at 35 mm and 45 mm from their corresponding extremes. Figure 3.2 depicts a schematic representation showing the location where the metallographic specimens were extracted.

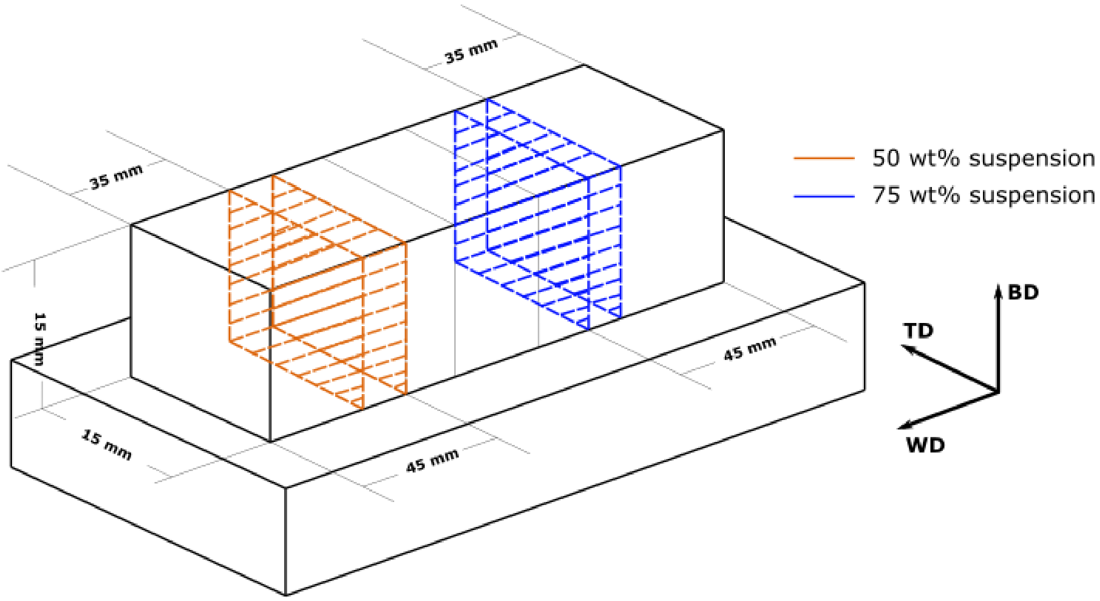

Figure 3.2: Schematic indicating the location where metallographic samples were extracted. The Reference system indicates the build direction (BD), the transverse direction (TD), and the welding direction (WD).

the resulting cross sections were embedded using conductive resin and the surface preparation was performed as follows: (1) samples were sanded using SiC sanding paper from grit 320 up to 1200, (2) polishing diamond suspensions of 3 μm and 1 μm were used in succession to achieve a mirror polish. Samples were then immersed in isopropanol and left to soak in an ultrasonic bath for 5 minutes to remove residual particles from the diamond suspensions. Microstructural features were revealed using Adler's reagent; composition can be seen in the table 3.8. The etching process consisted of submerging the samples in the reagent for 3 seconds and rinsing them thoroughly with distilled water to avoid over-etching.

Table 3.8: Adler's reagent composition.

Reactant	Amount
Copper ammonium chloride	9 g
Hydrochloric acid	150 ml
Ferric chloride, hydrated	45 g
Distilled water	75 ml

General aspects, grain morphology, grain boundary morphology, directional grain growth, microstructural features, crack presence, and substructures formed during the solidification process were observed and characterized using a Keyence VHX-500 digital microscope. High-resolution imaging, phase identification, and phase distribution were studied using a scanning electron microscope (SEM) model Jeol JSM IT-100.

EBSD inverse pole figure maps to determine the effect of the inoculants on texture formation were performed on the specimens with inoculant-loaded suspensions at 75 wt.% using a Helios G4 PFIB UXe SEM coupled with an EDAX detector. The specimens used consisted of a cross section with a thickness approximately of 1.5 cm extracted from the corresponding sections of the deposits, in between the metallographic specimens indicated in figure 3.2. The cross sections were then sliced perpendicularly to the build direction at 10 mm from the top. In addition to the surface preparation above described, samples for EBSD measurements were further polished using a colloidal silica solution with a particle size of 0.04 µm for a total of 40 minutes. Measurements were performed on the surface normal to the build direction. In addition to the EBSD inverse pole figure maps, the average grain size was estimated using the Hilliard single-circle procedure according to the ASTM standards E112-13 [74]. For the measurements, six fields of convenient size for the studied regions, at 1X magnification were used.

3.4. Chemical composition and structural characterization

From the remaining deposited specimens, an additional cross section, for each concentration and inoculant, was extracted at 25 mm from the extremes. The samples were then sanded using SiC sanding paper from 320 grit up to 1200 grit to achieve a smooth surface finish.

X-ray fluorescence (XRF) analysis was performed on both sides of each sample to determine the effect of the added inoculants on the chemical composition and the homogeneity of the process. Measurements were carried out using a Panalytical Axios Max WD-XRF spectrometer and data evaluation was done with SuperQ5.0i/Omnian software. Carbon content was determined with a combustion analyzer model CS844 manufactured by LECO.

Complementarily, X-ray diffraction measurements (XRD) were performed to determine the crystalline structures formed during the deposition process. The equipment used was a Bruker D8 Advance diffractometer Bragg-Brentano geometry. Samples with NbC as inoculant were analyzed using a Lynxeye position sensitive detector, Cu Kα radiation, divergence slit V12, scatter screen height 5 mm, 45 kV 40 mA. Samples with TiC as inoculant were analyzed using a graphite monochromator and Vantec position sensitive detector, Co Kα radiation, divergence slit var12, scatter screen height 8 mm, 40 kV 40 mA. The recorded data was evaluated using Bruker software DiffracSuite EVA vs 6.1. The lattice parameter was determined by finding the Y-axis intercept from the estimated lattice parameter for each peak found vs. the Nelson-Riley function plot.

3.5. Hardness measurements

A hardness tester Struers Durascan 70 was used to determine the Vickers hardness as an indicator of change in the mechanical properties of the materials deposited. The measurements were performed using HV1 method (9.807 N of downforce) and the spacing in between indentations was kept as 3 times the diagonal. For each specimen, indentations were distributed in two horizontal rows perpendicular to the building direction. Rows were positioned at 5 mm and 10 mm from the substrate. Figure 3.3 depicts a schematic of the methodology described.

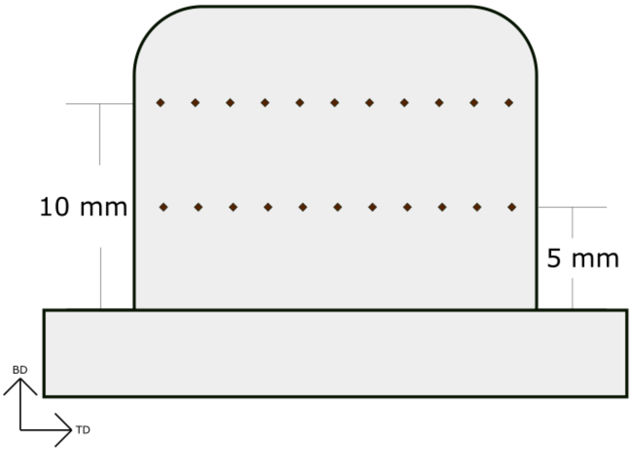

Figure 3.3: Schematic showing the location of the indentations.

4

Results & discussion

4.1. E2EM model implementation

4.1.1. Model validation

The script developed combines the original E2EM model fundamental steps of determining the close-packed or nearly close-packed directions and planes and calculating the mismatch between them with the equal-ratio method for interatomic spacing determinations, both described in chapter 3.1. Since this approach has not been reported before, the correct functioning of the model was verified by comparing the output from the model with the results reported by Zhang et al. Table 4.1 depicts the inoculant substrate pairs used in the validation, their corresponding crystalline structures, and their lattice parameters.

Table 4.1: Crystallographic information of inoculant-substrate pairs used for model validation [32, 69].

Inoculant	**Crystalline structure**	**Lattice parameter [nm]**	**Substrate**	**Crystalline structure**	**Lattice parameter [nm]**
TiC	FCC (Rocksalt)	a=0.46	Al	FCC	a=0.40494
TiB_2	HCP	a=0.3038 c=0.32392	Al	FCC	a=0.40494
Ti-Cr α	HCP	a=0.29564 c=0.46928	Ti-Cr β	BCC	a=0.325

Tables 4.2, 4.3, and 4.4 show the results obtained from the model and the corresponding reported values by the authors Zhang et al. For the pair TiC-Al, it can be seen that the calculated mismatch between the directions is in good agreement with the values reported. The difference encountered in the direction pairs <110>||<111> and <112>||<110> can be explained as follows: when determining the interatomic spacing mismatch, depending on the crystalline structure parameters, the inoculant-substrate pair can have a lower mismatch respect to the second nearest neighbor than to the first one.

The script computes all of these possibilities and selects the lower mismatch available. The reported mismatch values of -39.1% for the <110>||<111> and 34.4% for the <112>||<110> direction pairs are obtained by only considering the nearest neighbor. While these values are also computed by the script, the lowest mismatch value for <110>||<111> direction pair is 30.4% when two interatomic spaces of the matrix match one interatomic spacing of the inoculant. Analogously, the lowest mismatch value between the <112>||<110> direction pair corresponds to -31.2% considering that two atomic spaces of the inoculant match one atomic spacing of the matrix. The direction pairs also show good agreement with the reported values. The only difference encountered corresponds to the {220}||{200} plane pair. Despite computing the value as two interplanar spacings in Al matching one interplanar spacing in TiC, as stated by the authors, the misfit calculated corresponds to 19.7% instead of the 9.2% reported.

For the inoculant-substrate pair TiB_2-Al the observed trend is similar, the lower mismatch values among the directions corresponds to: considering a single atomic spacing match between the inoculant-substrate pair of the <110>||<$\overline{1}\overline{1}1$> direction pair; considering two atomic spacings of TiB_2 inoculant matches one atomic spacing of Al for the <112>||<110> and <112>||<001> direction pairs. Differences in interplanar mismatch can be explained similarly. The model considers two interplanar spacings of Al match one interplanar spacing of TiB_2 for the {111}||{001} and {220}||{101} plane pairs, and considers that two interplanar spacings of TiB_2 match one interplanar spacing of Al for the {111}||{110} plane pair.

Only the misfit values for some direction pairs were reported for the Ti-Cr(α)-Ti-Cr(β) system. However, it can be seen that the absolute values of the mismatch coincide (table 4.4). The difference in sign is indicative of the direction of relative displacement between the inoculant and substrate atoms.

From these results, it can be said that the model tends to underestimate the value of some mismatches. However, it is important to highlight that the values affected correspond to values that were already outside the 10% threshold considered. Furthermore, even with the underestimation, the new values remain outside the threshold. For a given inoculant-substrate pair, this could lead to an over-optimistic estimation of the potency of the inoculant. Nevertheless, for the purpose of this work, the model provides accurate enough mismatch values to be used as a criterion for inoculant selection.

Table 4.2: Mismatch values of direction and plane pairs for TiC-Al inoculant-substrate pair. Reported values extracted from [32].

Direction pairs				**Plane pairs**			
Substrate	**Inoculant**	**Model** [%]	**As reported** [%]	**Substrate**	**Inoculant**	**Model** [%]	**As reported** [%]
< 1 1 0 >	< 1 0 0 >	19.7	19.7	{ 1 1 1 }	{ 2 0 0 }	1.6	1.6
< 1 1 0 >	< 1 1 0 >	-13.6	-13.6	{ 1 1 1 }	{ 2 2 0 }	30.4	30.4
< 1 1 0 >	< 1 1 1 >	30.4	-39.1	{ 1 1 1 }	{ 1 1 1 }	-13.6	-13.6
< 1 0 0 >	< 1 0 0 >	-13.6	-13.6	{ 2 0 0 }	{ 2 0 0 }	-13.6	-13.6
< 1 0 0 >	< 1 1 0 >	19.7	19.7	{ 2 0 0 }	{ 2 2 0 }	19.7	19.7
< 1 0 0 >	< 1 1 1 >	1.6	1.6	{ 2 0 0 }	{ 1 1 1 }	-31.2	-31.2
< 1 1 2 >	< 1 0 0 >	7.2	7.2	{ 2 2 0 }	{ 2 0 0 }	19.7	9.2
< 1 1 2 >	< 1 1 0 >	-31.2	34.4	{ 2 2 0 }	{ 2 2 0 }	-13.6	-13.6
< 1 1 2 >	< 1 1 1 >	19.7	19.7	{ 2 2 0 }	{ 1 1 1 }	7.2	7.3

Table 4.3: Mismatch values of direction and plane pairs for TiB$_2$-Al inoculant-substrate pair. Reported values extracted from [32].

Direction pairs				Plane pairs			
Substrate	Inoculant	Model [%]	As reported [%]	Substrate	Inoculant	Model [%]	As reported [%]
< 1 1 0 >	< 1 1 0 >	-6.1	-6.1	{ 1 1 1 }	{ 1 0 1 }	12.6	12.6
< 1 1 0 >	< 0 0 1 >	-13.1	-13.1	{ 1 1 1 }	{ 1 0 0 }	-12.5	-12.5
< 1 1 0 >	< $\bar{1}$ $\bar{1}$ 1 >	22.5	-55.1	{ 1 1 1 }	{ 0 0 1 }	30.7	-38.6
< 1 1 0 >	< 2 1 0 >	8.1	8.1	{ 1 1 1 }	{ 1 1 0 }	-29.9	35.0
< 1 0 0 >	< 1 1 0 >	25.0	25,0	{ 2 0 0 }	{ 1 0 1 }	-0.9	-0.9
< 1 0 0 >	< 0 0 1 >	20.0	20,0	{ 2 0 0 }	{ 1 0 0 }	-29.9	-29.9
< 1 0 0 >	< $\bar{1}$ $\bar{1}$ 1 >	-9.7	-9.6	{ 2 0 0 }	{ 0 0 1 }	20.0	20.0
< 1 0 0 >	< 2 1 0 >	-29.9	-29.9	{ 2 0 0 }	{ 1 1 0 }	25.0	25.0
< 1 1 2 >	< 1 1 0 >	-22.5	38.7	{ 2 2 0 }	{ 1 0 1 }	28.7	-42.6
< 1 1 2 >	< 0 0 1 >	-30.6	34.7	{ 2 2 0 }	{ 1 0 0 }	8.1	8.1
< 1 1 2 >	< $\bar{1}$ $\bar{1}$ 1 >	10.5	10.5	{ 2 2 0 }	{ 0 0 1 }	-13.1	-13.1
< 1 1 2 >	< 2 1 0 >	-6.1	-6.1	{ 2 2 0 }	{ 1 1 0 }	-6.1	-6.1

Table 4.4: Mismatch values of direction pairs for Ti-Cr(α)-Ti-Cr(β) inoculant-substrate pair. Reported values extracted from [69].

Direction pairs			
Substrate	Inoculant	Model [%]	As reported [%]
< 1 1 1 >	< 1 1 0 >	-5.0	5.0
< 1 0 0 >	< 1 1 0 >	9.0	9.0
< 1 1 3 >	< 1 1 1 >	-2.9	2.9
< 1 1 3 >	< 2 1 0 >	5.0	5.0

4.1.2. Inoculant selection

From the implementation of the model, it can be deduced that inoculants with similar crystalline structures and lattice parameters to the substrate have a higher likelihood to comply with the mismatch criteria discussed. Additionally, given the high temperatures achieved during the deposition processes, thermal stability of the inoculants is also required so they can provide a nucleation surface.

According to the literature consulted, inoculation has not been implemented as grain refinement technique during the manufacturing of Invar 36 alloys. However, alloy modification has been used for the same purpose in several studies. Addition of Y, Mg, Ce, Zr-Ti,Ti, Nb and Ti-Ce have been proven to act as grain refiners [75–78]. The microstructural characterization revealed that these elements reacted forming inclusions in the form of oxides, sulfides, carbides, and complex compounds with multiple elements which then acted as nucleating surfaces promoting heterogeneous nucleation. Since the grain refinement was attributed to the formation and presence of the inclusions rather than the alloying elements, the direct addition of these inclusions in the form of particles should yield similar results. Among these inclusions TiC, and NbC were identified. Both of these carbides possess an FCC-rocksalt crystalline structure and a high melting point, making them good candidates as inoculants.

For the final selection, the corresponding crystallographic parameters of TiC, NbC, and Invar 36 were collected and applied to the model implemented (table 4.5). To ensure the most accurate prediction, XRD analysis was used to determine the lattice parameter of the filler wire. Measurements revealed that

Table 4.5: Crystallographic parameter for the species considered.

Specie	Crystalline structure	Lattice parameter
Invar 36	FCC	a=0.3595
TiC	FCC-rocksalt	a=0.4600 [32]
NbC	FCC-rocksalt	a=0.4469 [79]

the Invar 36 filler wire is composed of a single FCC phase with a lattice parameter of 0.3595±0.0003 nm. The mismatch calculated according to the implemented model can be seen in the tables 4.6 and 4.7.

Table 4.6: Direction and plane pairs mismatch between Invar 36 (a= 0.3595 nm) and NbC (a= 0.4469 nm) as calculated by the implemented model.

Direction pairs			Plane pairs		
Substrate	Inoculant	Mismatch calculated [%]	Substrate	Inoculant	Mismatch calculated [%]
< 1 1 0 >	< 1 0 0 >	12.1	{ 1 1 1 }	{ 2 0 0 }	-7.7
< 1 1 0 >	< 1 1 0 >	-24.3	{ 1 1 1 }	{ 2 2 0 }	23.9
< 1 1 0 >	< 1 1 1 >	23.9	{ 1 1 1 }	{ 1 1 1 }	-24.3
< 1 0 0 >	< 1 0 0 >	-24.3	{ 2 0 0 }	{ 2 0 0 }	-24.3
< 1 0 0 >	< 1 1 0 >	12.1	{ 2 0 0 }	{ 2 2 0 }	12.1
< 1 0 0 >	< 1 1 1 >	-7.7	{ 2 0 0 }	{ 1 1 1 }	28.2
< 1 1 2 >	< 1 0 0 >	-1.5	{ 2 2 0 }	{ 2 0 0 }	12.1
< 1 1 2 >	< 1 1 0 >	28.2	{ 2 2 0 }	{ 2 2 0 }	-24.3
< 1 1 2 >	< 1 1 1 >	12.1	{ 2 2 0 }	{ 1 1 1 }	-1.5

Table 4.7: Direction and plane pairs mismatch between Invar 36 (a= 0.3595 nm) and TiC (a= 0.4600 nm) as calculated by the implemented model.

Direction pairs			Plane pairs		
Substrate	Inoculant	Mismatch calculated [%]	Substrate	Inoculant	Mismatch calculated [%]
< 1 1 0 >	< 1 0 0 >	9.5	{ 1 1 1 }	{ 2 0 0 }	-10.8
< 1 1 0 >	< 1 1 0 >	-28.0	{ 1 1 1 }	{ 2 2 0 }	21.6
< 1 1 0 >	< 1 1 1 >	21.6	{ 1 1 1 }	{ 1 1 1 }	-28.0
< 1 0 0 >	< 1 0 0 >	-28.0	{ 2 0 0 }	{ 2 0 0 }	-28.0
< 1 0 0 >	< 1 1 0 >	9.5	{ 2 0 0 }	{ 2 2 0 }	9.5
< 1 0 0 >	< 1 1 1 >	-10.8	{ 2 0 0 }	{ 1 1 1 }	26.1
< 1 1 2 >	< 1 0 0 >	-4.5	{ 2 2 0 }	{ 2 0 0 }	9.5
< 1 1 2 >	< 1 1 0 >	26.1	{ 2 2 0 }	{ 2 2 0 }	-28.0
< 1 1 2 >	< 1 1 1 >	9.5	{ 2 2 0 }	{ 1 1 1 }	-4.5

For the Invar 36-NbC system, it can be seen that direction pairs <100>||<111> and <112>||<110>, and plane pairs {111}||{200} and {220}||{111} comply with the mismatch criteria of equal or less than 10%. Results for the Invar36-TiC system shows direction pairs <110>||<100>, <100>||<110>, <112>||<100>, and <112>||<111> and plane pairs {200}||{220}, {220}||{200}, and {220}||{111} have mismatch values of less than 10%. Whether these direction pairs are contained in the plane pairs was checked and the possible orientation relationships for both systems were reported in the table 4.8. As showcased, only one possible orientation relationship was determined for the Invar36-NbC system. In contrast, six possible orientation relationships were estimated for the Invar36-TiC system. From these results, it can be concluded that these carbides could act as grain refiners according to the criteria discussed. Furthermore, with more possible orientation relationships, the potency of TiC as inoculant should be higher than NbC.

Table 4.8: Possible orientation relationships of the studied systems.

System	Possible orientation relationships
Invar36-NbC	$[\,\bar{2}\;1\;1\,]_{Invar36} \parallel [\,0\;1\;0\,]_{NbC}\,,\;(\,1\;1\;1\,)_{Invar36} \parallel (\,0\;0\;2\,)_{NbC}$
Invar36-TiC	$[\,1\;1\;0\,]_{Invar36} \parallel [\,1\;0\;0\,]_{TiC}\,,\;(\,0\;0\;2\,)_{Invar36} \parallel (\,0\;2\;2\,)_{TiC}$
	$[\,0\;1\;0\,]_{Invar36} \parallel [\,0\;1\;\bar{1}\,]_{TiC}\,,\;(\,0\;0\;2\,)_{Invar36} \parallel (\,0\;2\;2\,)_{TiC}$
	$[\,0\;1\;\bar{1}\,]_{Invar36} \parallel [\,0\;1\;0\,]_{TiC}\,,\;(\,0\;2\;2\,)_{Invar36} \parallel (\,0\;0\;2\,)_{TiC}$
	$[\,1\;0\;0\,]_{Invar36} \parallel [\,1\;1\;0\,]_{TiC}\,,\;(\,0\;2\;2\,)_{Invar36} \parallel (\,0\;0\;2\,)_{TiC}$
	$[\,2\;1\;\bar{1}\,]_{Invar36} \parallel [\,0\;1\;0\,]_{TiC}\,,\;(\,0\;2\;2\,)_{Invar36} \parallel (\,0\;0\;2\,)_{TiC}$
	$[\,1\;0\;0\,]_{Invar36} \parallel [\,0\;1\;\bar{1}\,]_{TiC}\,,\;(\,0\;2\;2\,)_{Invar36} \parallel (\,1\;1\;1\,)_{TiC}$

4.2. Deposition of Invar 36 specimens with added inoculants

4.2.1. Macrostructure of deposited specimens

As described in the chapter 3.2.2 two layers of Invar 36 were deposited before the incorporation of the inoculants. Thin layers of the suspensions were thoroughly applied to the surface of the previously deposited layer with the aim to make them as homogeneous as possible. During its application, the elevated temperature of the workpiece caused a reduction in the viscosity of the polymeric suspension aiding in achieving a uniform coating. Figure 4.1 shows the partially deposited Invar 36 specimen with the NbC-loaded suspension applied. The coating had a smooth appearance, showed no lumps, and the solidification ripples from the previously deposited layer could still be appreciated.

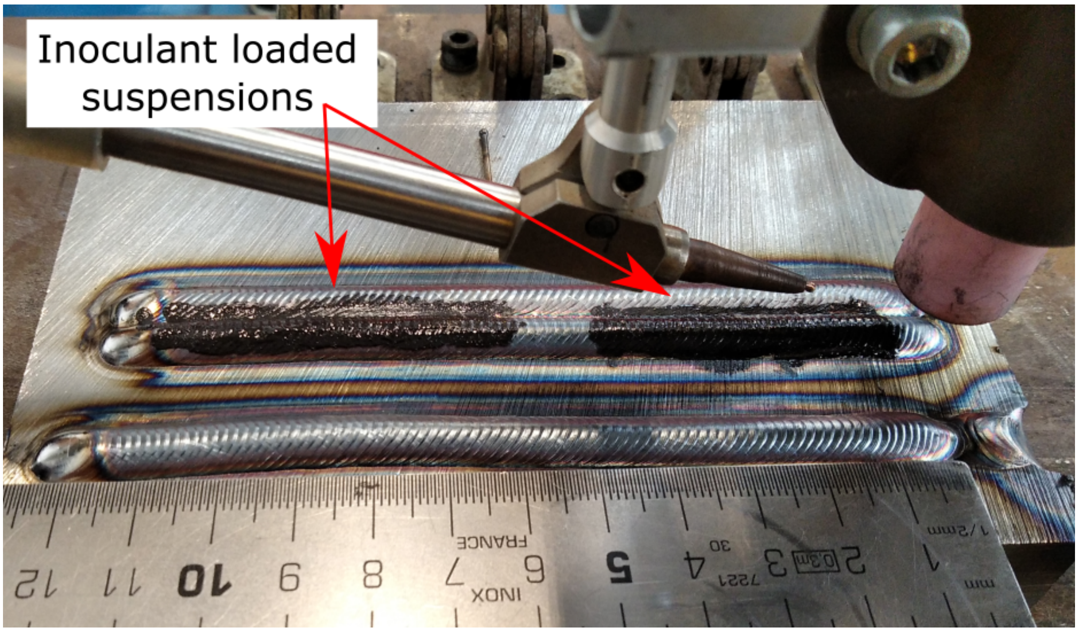

Figure 4.1: Partially deposited Invar 36 cuboidal specimen coated with a layer of inoculant-loaded suspension.

Before and after the application of the inoculants, the deposition process remained unchanged. No additional spatter was formed, no arc instability was detected, and no apparent change in the weld-pool behavior was observed. The macrostructure of the deposited specimens can be seen in the figure 4.2. Visual inspection revealed the presence of the stair-stepping effect and the start-stop defects characteristic of WAAM processes. However, none of the specimens showed cracks, macro porosity, or delamination. Furthermore, the weld bead geometry was uniform and constant throughout the whole length of the depositions. Overall, it can be concluded that the application methodology was successful and that it did not cause any unfavorable effects on the deposition process.

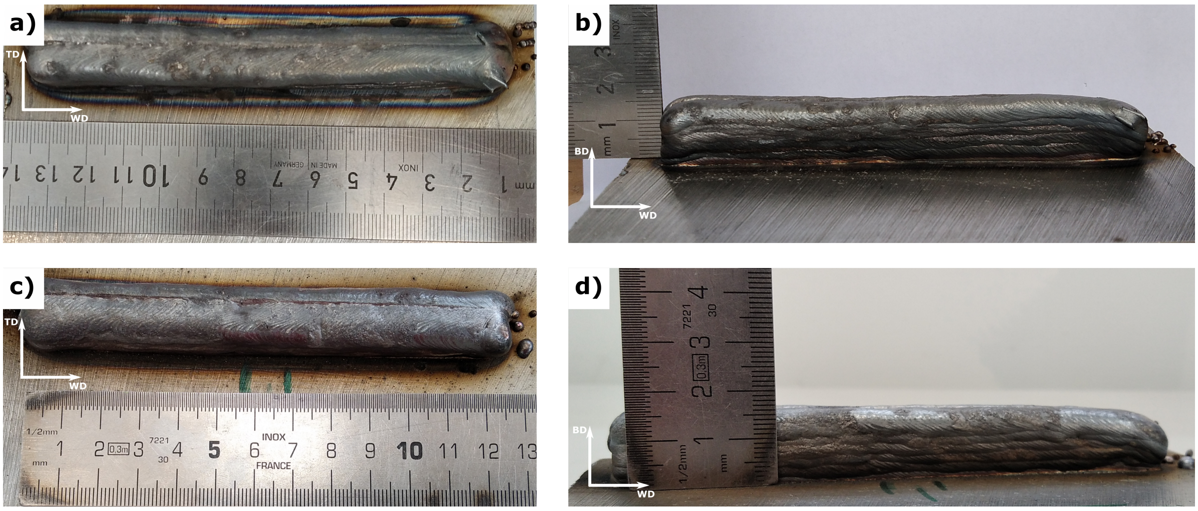

Figure 4.2: Macroscopic appearance of deposited Invar 36 cuboidal specimens inoculated with NbC-loaded suspension (a) and (b), and TiC-Loaded suspension (c) and (d).

4.2.2. Microstructural characterization

Figure 4.3 depicts the microstructure of the four different specimens. As can be seen, despite the addition of the inoculants, the microstructures still exhibit a predominant columnar grain morphology with preferential orientation along the build direction. Details on the presence of defects, microstructural morphology, longitudinal columnar grain size, and grain boundary character are presented below.

Presence of defects

According to the previous study consulted, cracks and voids were observed along the grain boundaries [16]. In this work, these phenomena were only observed in specimens inoculated with 50 wt% loaded suspensions. In the Invar 36 with NbC-loaded suspension at 50 wt%, cracks were encountered near the middle region with respect to both, the build direction and the transverse direction (figure 4.4a, b, and c), and no voids were detected. In a similar way, in the specimen with TiC-loaded suspension at 50 wt% the majority of the cracks and voids were located near the center of the specimen. From a simple visual inspection, the number and size of cracks were inferior compared to the ones encountered in the specimens inoculated with NbC. Specimens inoculated with TiC-loaded suspension at 50 wt.% also showed the presence of voids along the GBs (figure 4.4d, e, and f). Overall, the addition of inoculants proved to have a favorable effect on the reduction of crack formation during the manufacturing process.

Additionally, both specimens inoculated with TiC showed a lack of fusion defect in the middle top region. This lack of fusion was attributed to a small misalignment of the welding torch during the deposition process resulting in a reduction of the optimal hatch distance.

During the deposition process, porosity can be formed due to gas entrapment. However, no porosity

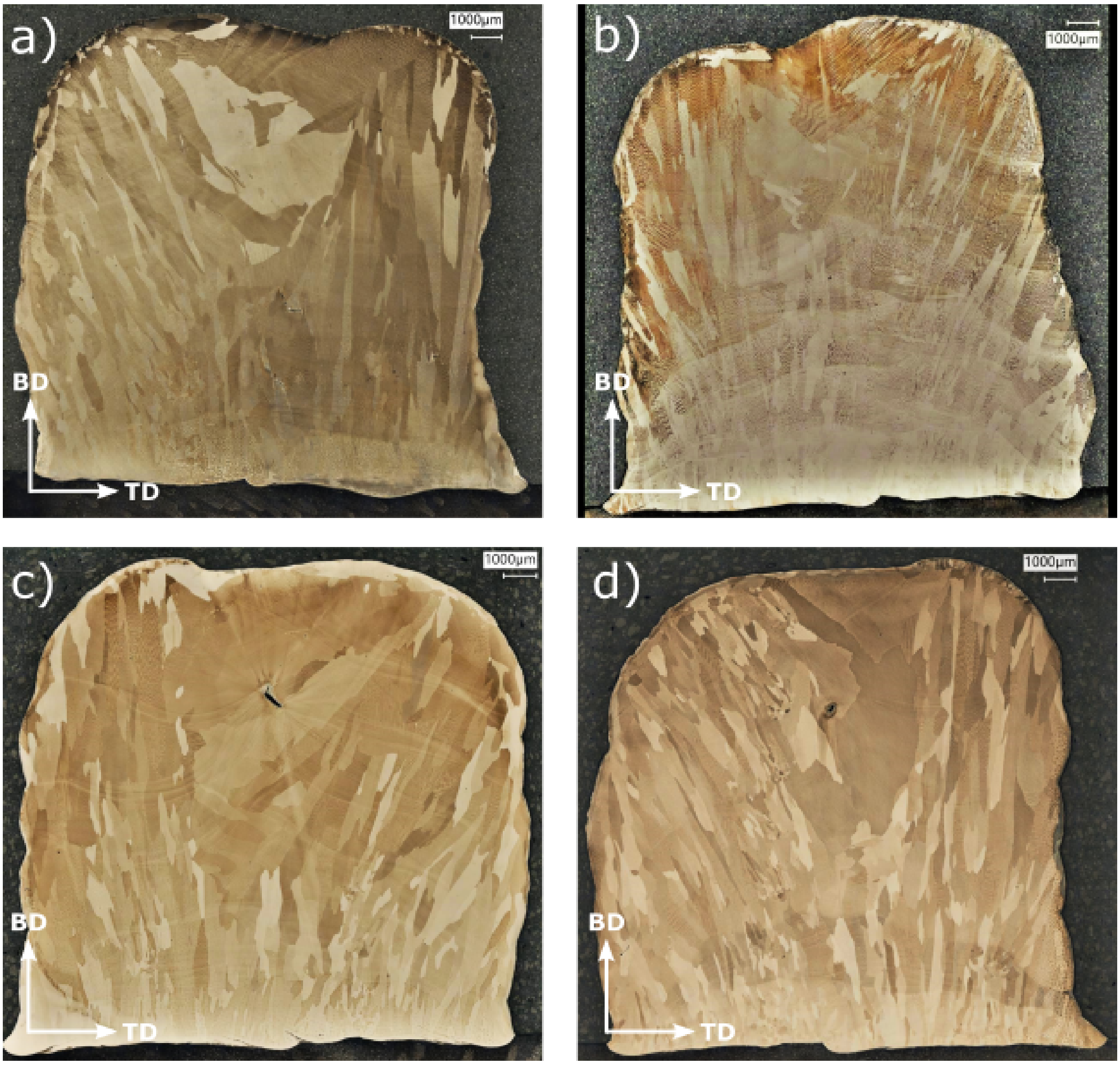

Figure 4.3: Microstructure of deposited specimens. a) Invar 36 + NbC at 50 wt%, b) Invar 36 + NbC at 75 wt%, c) Invar 36 + TiC at 50 wt% and d) Invar 36 + TiC at 75 wt%

was encountered in any of the specimens. This implies that the extra gas generated from the thermal decomposition of the polymeric resin, during the deposition process, did not affect the component quality.

Microstructural morphology

As already mentioned, the four specimens depict the characteristic preferential epitaxial columnar grain growth of WAAM processes. A closer examination of these columnar grains revealed the formation of several distinct substructures, namely, cellular, columnar dendritic, cellular-dendritic, and equiaxed dendrites. The development, size, and distribution of microstructural features are dependent on the chemical composition and solidification conditions (temperature gradient and solidification rate) [80, 81]. The presence of such an elevated number of substructures indicates a complex and heterogeneous solidification process across the whole specimen. Such substructures were observed in all four specimens and appear to have no preferential location across the samples. Furthermore, some

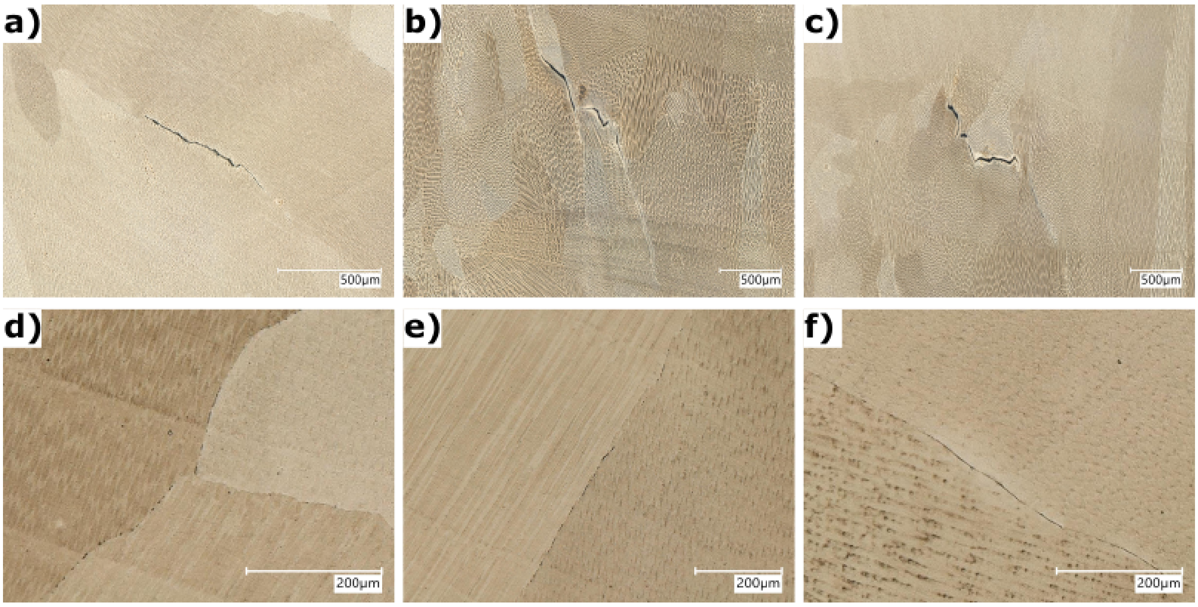

Figure 4.4: Cracks and voids encountered in the specimens with added inoculant-loaded suspensions at 50 wt.%. a), b), and c) inoculated with NbC; d), e), and f) inoculated with TiC.

of these substructures coexist within the same grain which, again, is an indicator of a complex and inhomogeneous solidification process. Cellular, cellular-dendritic, and columnar dendritic were the predominant substructures encountered in all four specimens. Figure 4.5 showcases the substructures mentioned.

Both samples inoculated with 50 wt.% loaded suspensions possess a similar microstructural morphology composed of mainly slender columnar grains. On the contrary, samples inoculated with 75 wt.% loaded suspensions show a completely different microstructural morphology, among them, and with respect to the lower concentration of the same inoculant. The sample with NbC-loaded suspension at 75 wt% depicts a rather heterogeneous microstructure combining long columnar grains with smaller almost-equiaxed grains distributed across the whole area of the specimen. The most remarkable feature corresponds to the change in the grain boundary character from smooth and straight to tortuous. The sample inoculated with TiC-loaded suspension at 75 wt% shows, from a qualitative point of view, an increased number of columnar grains with respect to the sample with TiC at 50 wt%. and the presence of equiaxed grains clusters located near the fusion lines.

Whereas the addition of inoculants was not enough to induce a columnar to equiaxed transition on the microstructure, the long axis length of the columnar grains differs from one specimen to another. In an attempt to quantify these differences, grain size measurements on the long axis of the columnar grains were made. Figure 4.6 shows the average measured length and the largest feature encountered on the specimens compared to a reference sample from [16].

Although samples inoculated with the NbC-loaded suspension at 50 wt.% showed a 17% reduction in the average long axis length of columnar grains with respect to the reference, the largest feature encountered corresponds to this specimen with a 4% difference in length. The same concentration of TiC suspension achieved a 30% reduction in the long axis length and showed a 16% smaller largest feature. Samples with added NbC-loaded suspension at 75 wt.% suspension achieved the largest long axis reduction in columnar grain size with a value 45% smaller, and a smaller largest feature by

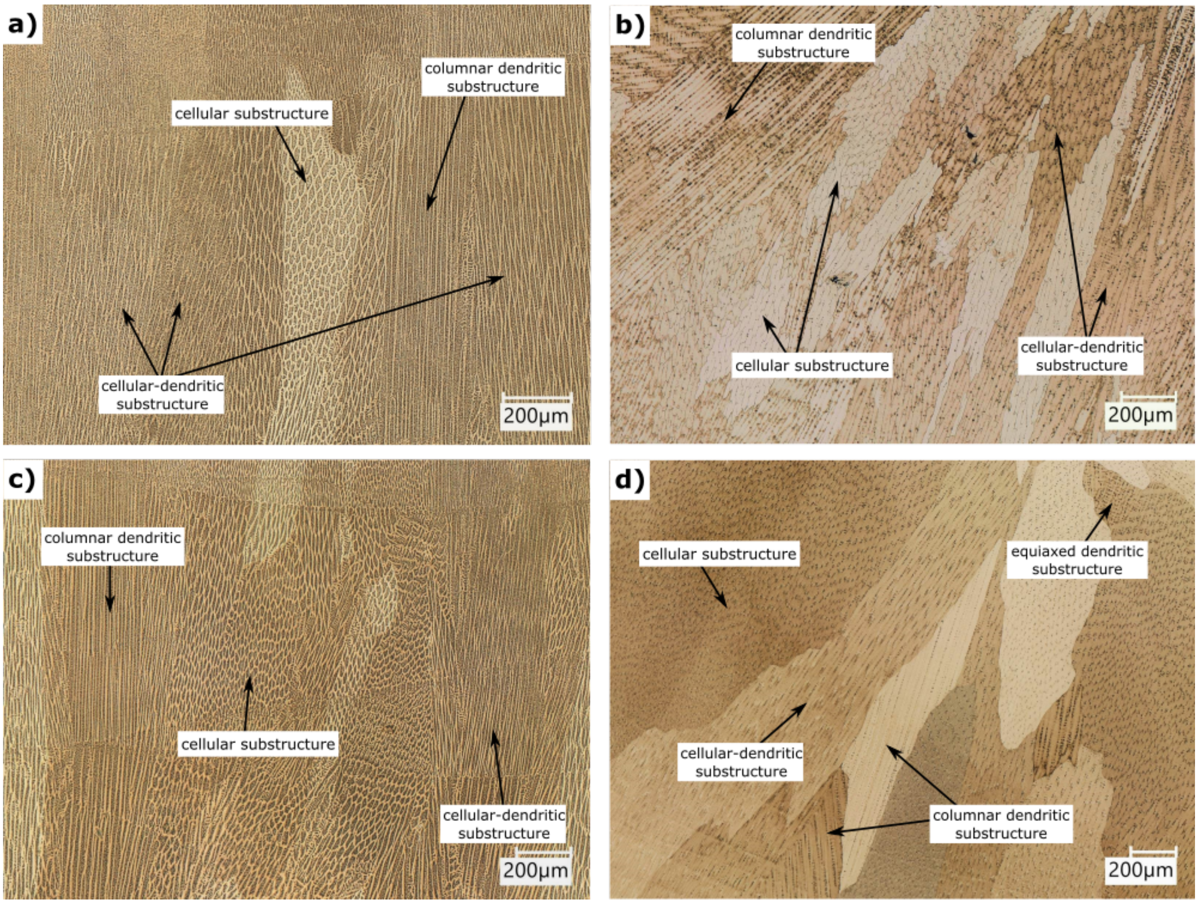

Figure 4.5: Observed substructures on the deposited specimens. a) Invar 36 + NbC at 50 wt%, b) Invar 36 + NbC at 75 wt%, c) Invar 36 + TiC at 50 wt% and d) Invar 36 + TiC at 75 wt%

42%. On the other hand, samples inoculated with TiC-loaded suspension at 75 wt.% depicted only a 30% reduction in the long axis length of columnar grains and a 25% smaller largest feature. As above mentioned, these measurements were only performed on the columnar grains; the equiaxed regions observed in the samples inoculated with TiC-loaded suspension at 75 wt.% were not accounted for. In this regard, despite not having the smallest average columnar grain size reported, the presence of equiaxed grains on the samples inoculated with TiC-loaded suspension at 75 wt.% is a good indicator of a greater refining effect than.

Due to the non-equilibrium nature of the solidification conditions during the deposition process, the presence of a single larger feature on the microstructure is not conclusive and an extensive statistical analysis should be carried out to properly establish a significant value, the results of the present measurements are only an indicator of the general trend observed. A similar argument could be made for the difference in the average long axis length of columnar grains, however, from the measurements and the microstructural analysis, it can be stated that all the specimens with added inoculants developed a smaller average long axis length of columnar grains compared to the reference, indicating that the addition of inoculants accomplished a refining effect. These results are in agreement with the predictions made based on the results obtained from the implemented E2EM model.

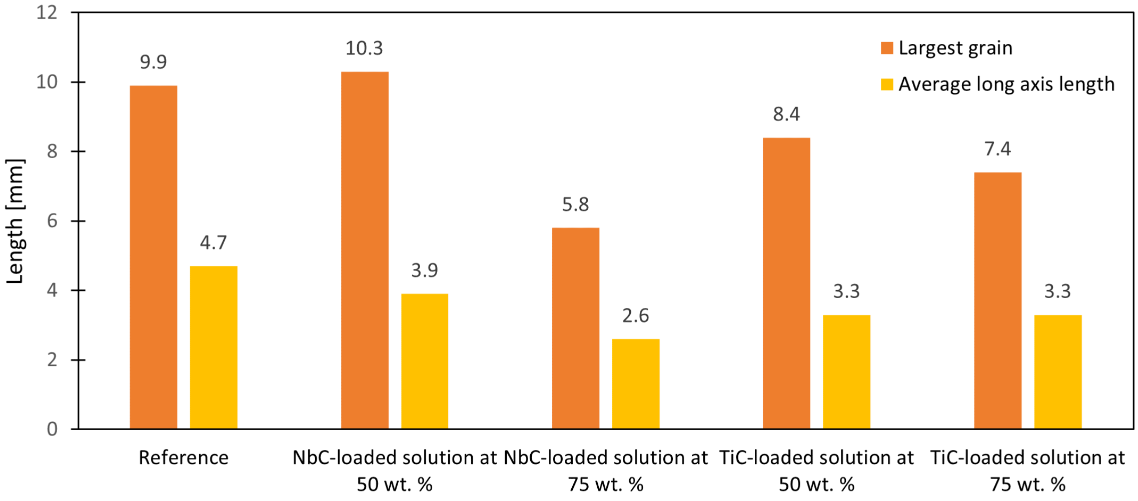

Figure 4.6: Largest feature and average long axis length of columnar grains measured on the deposited specimens.

4.3. Effect of inoculant addition to Invar 36

Coarse columnar grains and cracking are two common features reported in the manufacturing of Invar 36 components. Furthermore, it has also been reported that the cracking issue can be exacerbated by the presence of such microstructural morphology [16, 75, 76]. The reduction in average columnar grain size, the presence of equiaxed grains in some samples, and the reduced presence of cracks are good indicators that the addition of the selected inoculants had a positive effect on the microstructural development and solidification structure of the specimens produced. However, the differences between the different inoculants also suggest that different mechanisms are responsible for the observed phenomena.

In order to fully understand the effects of inoculant addition, and therefore explain the mechanisms behind the observed phenomena, SEM imaging, EDS, XRF, and XRD measurements were collected. The results and the corresponding discussion are presented below.

4.3.1. Effect of NbC Addition

Solidification structure

SEM imaging of the specimens containing the 75 wt.% loaded suspension revealed a microstructure composed of two distinctive phases (figure 4.7a). As can be seen, the brighter phase solidified preferentially across the solidification grain boundaries (SGB) and the solidification subgrain boundaries (SSGB). As observed in figure 4.7b, a higher magnification showed the brighter phase arranged in a lamellar morphology characteristic of eutectic invariant reactions. No particles were observed in any of the specimens studied.

EDS measurements were taken at the indicated points in figure 4.7 to check for composition differences; results of the different point scans can be seen in the tables 4.9 and 4.10. In table 4.9, point scans 4, 5, and 6 correspond to the primary phase, despite the different shades observed in the SEM imaging, results indicate there is no significant difference in composition. Points 2 and 3 were taken

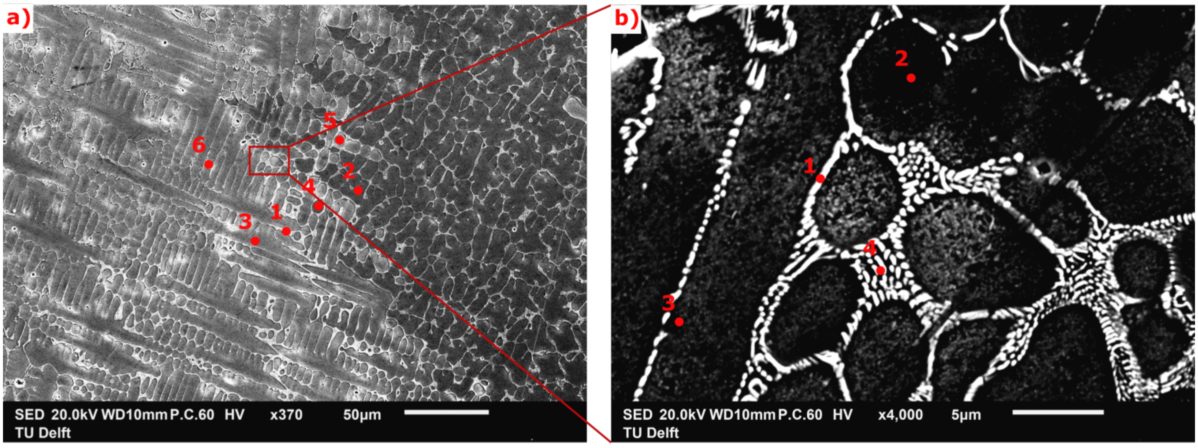

Figure 4.7: SEM images of: (a) microstructure of WAAM Invar 36 specimen with NbC at 75wt.% suspension, and (b) detail showing the lamellar structure encountered. Red dots indicate EDS point scan locations.

near the SSGB and they depict a small concentration of silicon. In Invar 36 Si, Mn, and C are encountered as impurities, detection of such elements near the SGB and SSGB suggests solute redistribution, characteristic of alloy solidification processes [80]. Finally, point 1 was taken directly over the secondary phase formed at SSGB revealing the presence of Nb, Si, and Mn. The Si and Mn can, again, be correlated to solute redistribution. Additionally, Nb enrichment in SGB and SSGB, the absence of particles, and the presence of a lamellar morphology suggest the dissolution of NbC particles and posterior solidification in a eutectic constituent.

The composition determined from the point scans in figure 4.7b shows similar results. Point scans 2 and 3 from table 4.10 correspond to the primary phase. Presence of Nb and Mn encountered in point scan 3 can be attributed to the proximity to the SSGB. Points 1 and 4 were measured directly on top of the secondary phase and the results are in agreement with the analogous region analyzed in the figure 4.7a. Differences in Nb, Si, and Mn, can be explained by the relative size of the point scan with respect to the microstructural feature. The smaller size of the secondary phase in point scan 3 may have caused a larger area of the scan to coincide with the primary phase resulting in a lower Nb content. Figure 4.8 shows an EDS elemental map distribution of the same region considered in figure 4.7b and its corresponding spectrum. The elemental distribution found is in agreement with the point scans performed and Nb can be preferentially found along the SGB and SSGB.

Table 4.9: EDS point scan composition in wt.% from figure 4.7 a.

Point scan	Si	Mn	Fe	Ni	Nb
1	0.22	0.75	60.16	32.25	6.61
2	0.17	-	67.19	32.63	-
3	0.20	-	67.28	32.53	-
4	-	-	67.36	32.62	-
5	-	-	67.59	32.41	-
6	-	-	66.43	33.57	-

Table 4.10: EDS point scan composition in wt.% from figure 4.7 b.

Point scan	Si	Mn	Fe	Ni	Nb
1	0.25	0.57	62.40	33.69	3.07
2	-	-	67.69	32.29	-
3	-	0.56	64.49	33.57	1.38
4	0.44	-	60.09	32.83	6.49

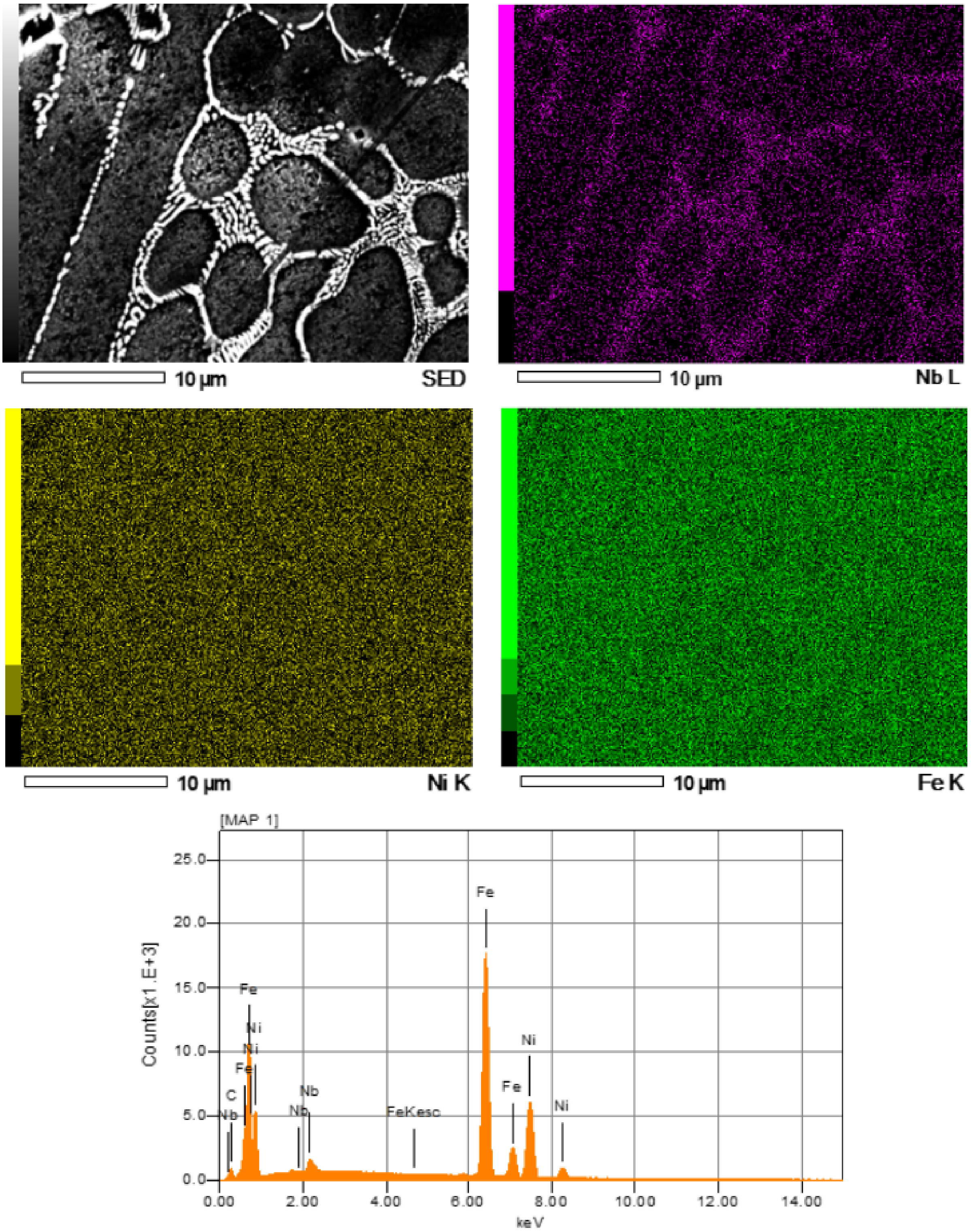

Figure 4.8: EDS elemental map and corresponding spectrum of Invar 36 with added NbC at 75wt.% suspension.

The average determined composition of the specimens inoculated with NbC is shown in table 4.11. As can be seen, an increment of 25 wt.% of NbC in the solution, resulted in a Nb increase of approximately 0.3 wt.%. According to the manufacturer, the filler wire has a carbon content of 0.05 wt.%; combustion analyzer measurements after the deposition revealed a carbon content of 0.04±0.01 wt.% for both concentrations of NbC-loaded suspensions. Such low concentration after the deposition confirms the hypothesis that the thermal decomposition of the polymeric resin used to incorporate the inoculants did not have detrimental effects on the deposition process, nor caused additional carbon absorption into the system.

Table 4.11: Average composition in wt.% of Invar 36 specimens inoculated with NbC according to XRF measurements.

	NbC-loaded suspension concentration	
Element	**50 wt.%**	**75 wt.%**
Fe	63.1 ± 0.4	62.6 ± 0.4
Ni	36.1 ± 0.4	36.3 ± 0.4
Nb	0.13 ± 0.01	0.46 ± 0.02
Si	0.21 ± 0.01	0.25 ± 0.02
Mn	0.27 ± 0.02	0.36 ± 0.03
Mo	0.042 ± 0.006	0.036 ± 0.006
Cr	0.040 ± 0.008	0.038 ± 0.008
P	0.005 ± 0.002	-
Al	0.052 ± 0.007	0.028 ± 0.005

XRD spectra from the reference material and the inoculated specimens are depicted in figure 4.9, and the corresponding calculated lattice parameter can be seen in table 4.12. The three spectra depict a single phase which was identified as an FCC structure. Similar 2Θ values and width for the identified peaks indicate no additional strain was introduced into the material due to the addition of inoculants. Between the reference sample and the samples containing inoculants, a clear change in relative peak intensity can be observed. Among other factors, peak intensity in XRD analysis is correlated with the occurrence of crystallographic planes [82]. Therefore, the high quotient between the intensity of {111} planes with respect to the other observed planes in the reference pattern, suggests a preferential orientation of the {111} planes parallel to the weld direction. By the same reasoning, the shift in relative intensity observed in the samples with added NbC as inoculant indicates a reduction in the preferential plane orientation, and consequently a reduction in the material texture, characteristic of WAAM processes.

Table 4.12: Calculated lattice parameter for Invar 36 specimens inoculated with NbC-loaded suspensions.

Specimen	**Lattice parameter [nm]**
Reference	0.3592 ± 0.0006
NbC at 50 wt.%	0.3598 ± 0.0006
NbC at 75 wt.%	0.3596 ± 0.0005

EBSD inverse pole figure maps and estimated average grain size of the reference specimen and the specimen inoculated with NbC-loaded suspension at 75 wt.% are shown in figure 4.10 and table 4.13 correspondingly. Average grain size measurements of the middle regions depicted in the figure 4.10, namely 1.B and 2.C, were not carried out since it was not possible to draw circumferences that comply with the ASTM standards. Comparisons made for these regions are from a qualitative point of view.

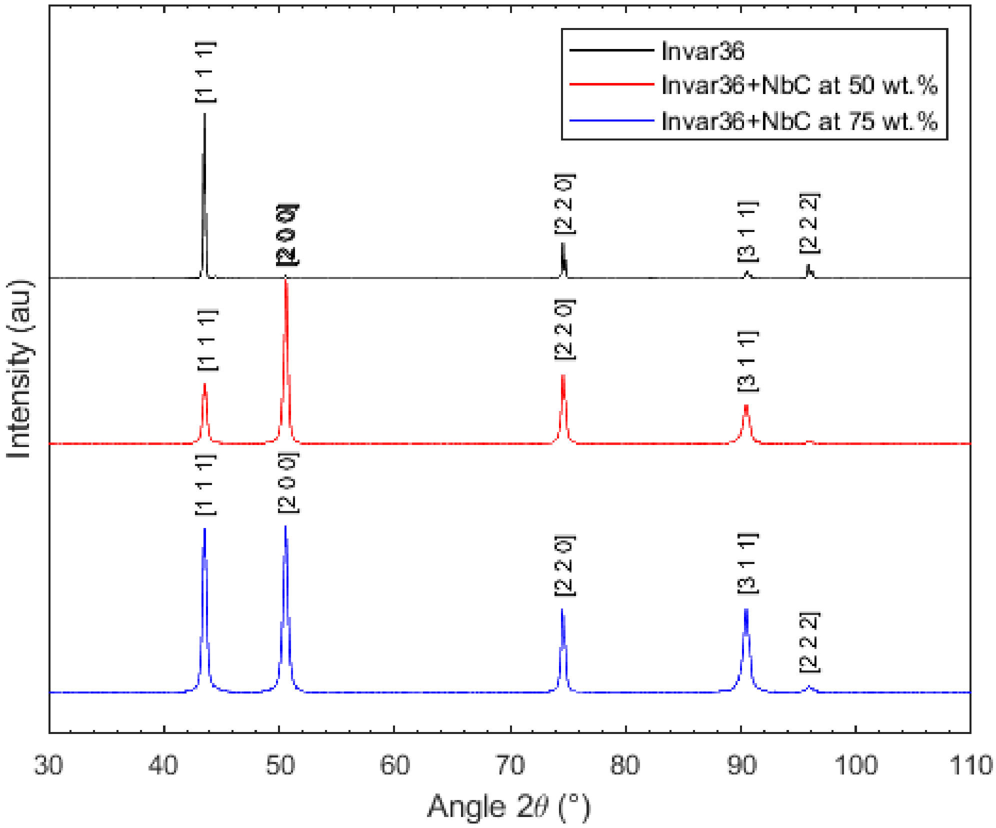

Figure 4.9: XRD patterns of Invar 36 reference and NbC-inoculated specimens.

The two samples show clear differences with respect to grain size, grain morphology, and GB character. The reference sample (figure 4.10-1) shows a microstructure composed of rather large grains, most of them exhibit an elongated nature, some of them approximate to be equiaxed, and the grain boundaries throughout the whole specimen have a strong straight character depicting little to no tortuosity. On the other hand, the microstructure of the specimen inoculated with NbC-loaded suspension at 75 wt.% (figure 4.10-2) is composed of a combination of small almost-equiaxed grains, large elongated grains, and intermediate-sized grains with a nature ranging from almost-equiaxed to elongated. Moreover, the tortuous GB character is clearly visible in all the grain morphologies and sizes described. It can also be seen that the different grain morphologies described are located in specific regions of the respective specimens. The coarsest grains can be found near the middle region in both specimens. Region 1.B, on the reference specimen, has a length of approximately 5.8 mm, and region 2.C, on the specimen with added inoculants, has a length of approximately 3.8 mm. During the solidification and cooling process, the middle portion of the specimens experiences the lowest cooling rates promoting grain growth as opposed to grain nucleation, and grain coarsening with successive layer depositions [16]. The elongation along the transverse direction can be attributed to the directional heat extraction. Heat dissipates along the build direction and from the extremes of the transverse direction towards the middle portion, this causes the material to form columnar grains along the build direction and, at the same time, directional growth across the transverse direction. It is worth noting that this region containing coarse grains is not only smaller by approximately 2 mm in the specimen with added inoculants, but also the grains encountered are smaller across the TD and the WD. Regions 1.A and 1.C of the reference sample, with lengths of 4.8 mm and 2.8 mm respectively, are located on the extremes of the deposited specimen and have estimated average grain areas of 0.3348 mm^2 and 0.5045 mm^2 accordingly. Analogously, regions in the specimen with added inoculants 2.A (3.8 mm) and 2.D (3.0 mm) are also located near the extremes of the deposited specimen and have similar morphologies among them. Comparing these regions, it can be seen that in region 2.A, with an average grain area of 0.0942 mm^2, experienced an area reduction of approximately 255% with respect to region 1.A. In a similar trend, in region 2.D, with an average grain area of 0.1596 mm^2, the accomplished area reduction was approximately 216% with respect to region 2.D.

Contrary to the reference specimen in which only three distinctive regions can be appreciated, the specimen with added inoculants shows four distinctive regions. This fourth region, namely 2.B, with a length of approximately 1.2 cm, contains the smallest grains of the sample with an average area of 0.0206 mm^2. Compared to the region with the smallest grain size from the reference image, region 1.A, the grain size reduction attained corresponds to approximately 1500%. The existence of this region can be explained and attributed to the manufacturing process. Each layer of the fabricated specimens is formed by depositing two weld beads side-by-side. During the deposition process, and according to the orientation seen in figure 4.10, the first weld bead of each layer was deposited on the right side. Since the application of the inoculant-loaded suspensions was carried out before each individual weld bead, it is most likely that the corner formed by the first weld bead and the previously deposited layer caused the suspension to accumulate in a higher concentration than in the rest of the weld bead. Thus, it is most probable that the increased suspension concentration induced greater localized grain refinement in the sample. However, this level of refinement and grain morphology was not observed on the transversal cross-section of the specimens studied (figure 4.3b). These observations suggest that despite the increased number of nuclei formed, epitaxial growth predominated during the solidification process. Lastly, while it may seem that no strong texture is present in either of the specimens, some orientations appear to be preferential. Nonetheless, from the EBSD inverse pole figure maps presented no further conclusions can be drawn.

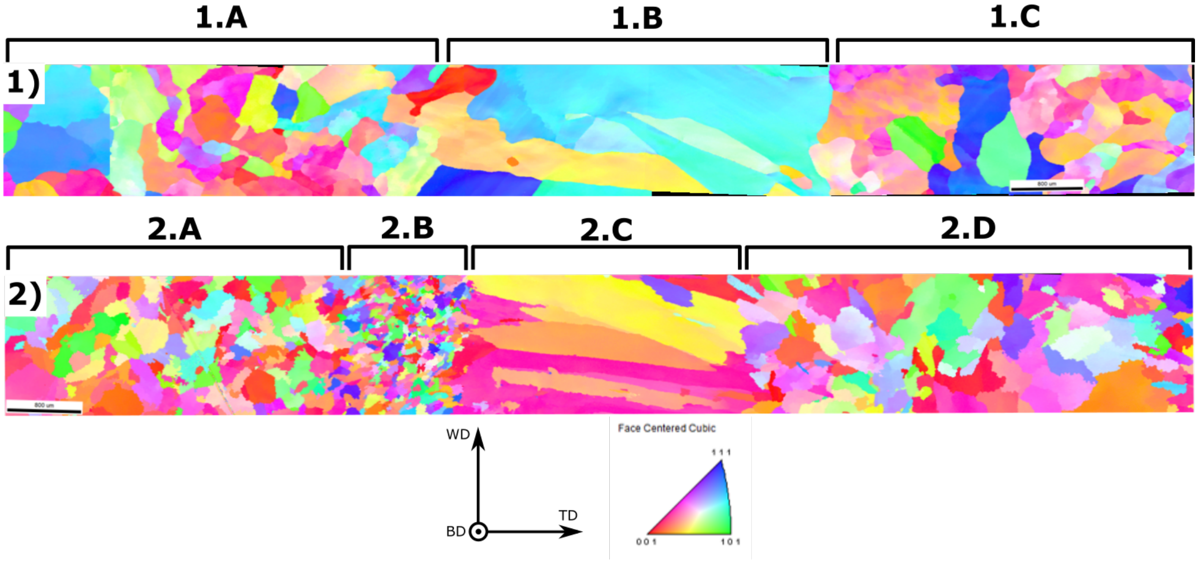

Figure 4.10: EBSD inverse pole figure map of (1) Invar 36 reference specimen and (2) Invar 36 specimen inoculated with NbC-loaded suspension at 75 wt.%. Regions denoted by the letters above the images indicate zones with different grain morphology.

Table 4.13: Estimated average grain size of the reference sample and the sample inoculated with NbC-loaded suspension at 75 wt.%. Regions indicated in the table correspond to the regions depicted in the figure 4.10.

Specimen	Region	Mean intercept [mm]	Confidence interval 95% [%]	Relative accuracy [%]	ASTM grain size [G]	Average grain area [mm^2]
REF	1.A	0.51 ± 0.05	[0.47 , 0.56]	9.3	-1.4	0.3348
	1.C	0.63 ± 0.06	[0.57 , 0.69]	9.6	-2.0	0.5045
Invar36	2.A	0.27 ± 0.02	[0.25 , 0.30]	9.4	0.5	0.0942
+	2.B	0.13 ± 0.01	[0.12 , 0.14]	8.4	2.7	0.0206
NbC	2.D	0.36 ± 0.03	[0.32 , 0.39]	9.2	-0.3	0.1596

Further analysis of the XRD patterns revealed the presence of NbC in the specimen inoculated with NbC-loaded suspension at 75 wt.% (figure 4.11). From the confirmed presence of NbC, in combination with the lamellar morphology, it can be concluded that the Invar 36 FCC phase forms a eutectic structure with the NbC during the solidification process. Osuki et al. [83] performed a series of experiments to study the solidification process on Invar 36 alloy in weldments with crystallization of NbC. Among their findings, the following conclusions are relevant to this study: (1) NbC crystallizes during the final stage of solidification in localized zones with a Nb content of 4 wt.% or more, and only if enough carbon is present; (2) crystallization of the NbC during the solidification process causes a reduction in the liquid/solid coexistence range reducing the solidification cracking susceptibility; (3) an increase in carbon content shifts the crystallization temperature of NbC closer to the solidification onset temperature, this effect is increased with an increase in Nb concentration [83]. In this work, the specimens studied have a carbon content of 0.4 wt.%. Based on the conclusions from Osaka et al. the higher concentration of carbon should increase the NbC crystallization onset temperature, reduce the solidification temperature range, and the formation of solidification cracks. While solidification cracks have been reported as a common issue in the manufacturing process of Invar 36 components, this type of cracks was not observed in this work, nor in the previous study consulted; further details on this matter are presented below. Notwithstanding, These considerations offer an explanation for the formation of the eutectic constituent along the SGB and SSGB in the specimens inoculated with NbC-loaded suspension at 75 wt.%. On the other hand, in the specimen inoculated with NbC-loaded suspension at 50 wt.%, despite having the same carbon content, the lack of eutectic constituent, and the absence of NbC according to the XRD measurements suggests that a Nb content of 0.13 wt.% is below the minimum concentration required to achieve the aforementioned effects.

The addition of inoculants was intended to promote heterogeneous nucleation, however, based on the findings, the refining mechanism observed corresponds to grain growth restriction. The particles incorporated, rather than acting as nucleating surfaces, appear to have dissolved in the melt and were segregated during the solidification process. When alloys solidify, solute is rejected into the melt pool, this process is diffusion-controlled and forms an enrichment-depletion zone ahead of the solidification front, the solid/liquid interface. Solute segregation causes constitutional undercooling which may induce new nucleating events generating new grains [84–87]. At the same time, changes in the solute concentration in the melt alter the diffusivity of the elements reducing the velocity of the solidification front in a phenomenon called solute growth restriction; with a reduced growth velocity, the constitutional undercooling increases [85, 86]. Attractive interactions between solute elements with high affinity for

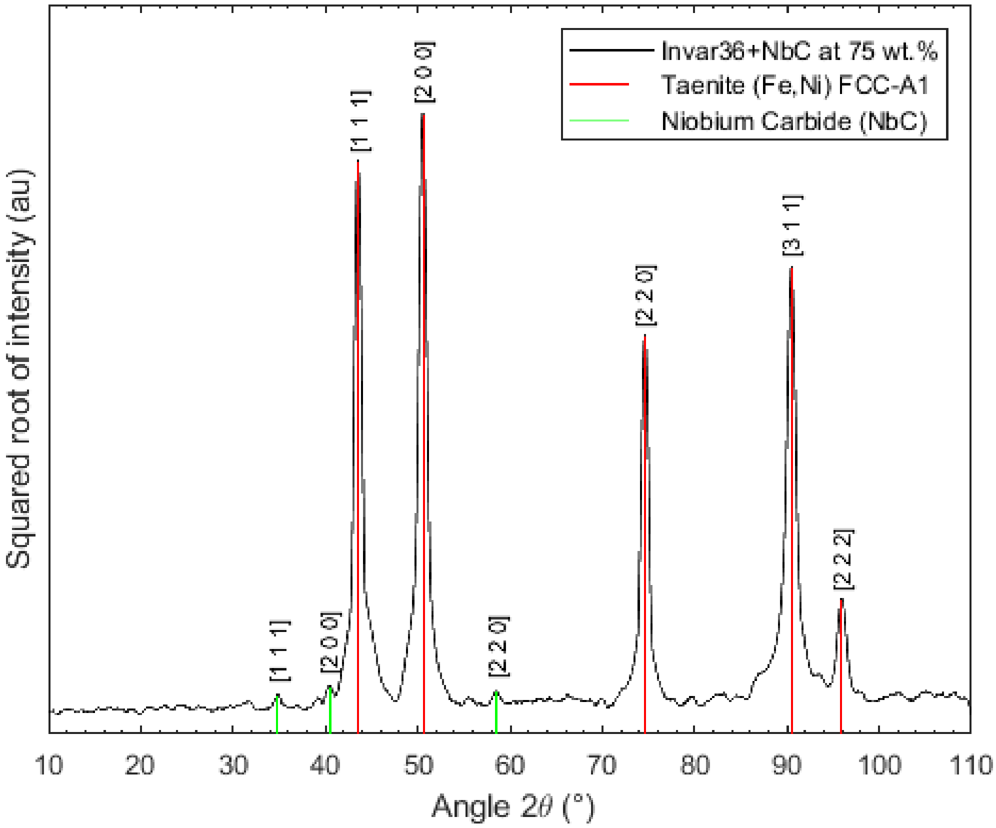

Figure 4.11: XRD pattern of Invar 36+NbC at 75 wt.%. The squared root of intensity has been used to highlight low-intensity peaks and the signal has been processed to reduce the noise.

each other further reduce the diffusion coefficients achieving higher solute growth restriction [84, 88]. The synergy between both phenomena induces grain refinement and it is consistent with the findings reported in this work.

Crack formation

Crack formation is a complex phenomenon that may be caused by several factors. In order to understand the effect of the inoculant on crack formation, the identification of the responsible mechanisms is of utmost importance. In this regard, further analysis of the cracks encountered on the specimen inoculated with 50 wt.% was performed, and the following observations are noteworthy to mention: (1) cracks are of intergranular nature; (2) most of them appear to have originated or ended on a triple point; (3) their appearance is mostly straight; (4) they propagate along migrated grain boundaries (MGB). These characteristics have been depicted and highlighted in figure 4.12. According to the literature, these characteristics, in combination with the grain boundaries of straight character, and being Invar 36 a single-phase FCC material, are good indicators of DDC [89–93].

As briefly commented in chapter 2.2.7, DDC is a solid-state cracking phenomenon that occurs, as its name indicates, due to a decrease in ductility in combination with thermal stresses. Ductility dip cracks are of intergranular nature and are formed in a range of temperatures between 0.5 to 0.8 times the melting temperature where some susceptible alloys experience a sharp decrease in ductility [89, 92]. Materials that solidify in single-phase FCC crystalline structure, with low impurity levels, have been

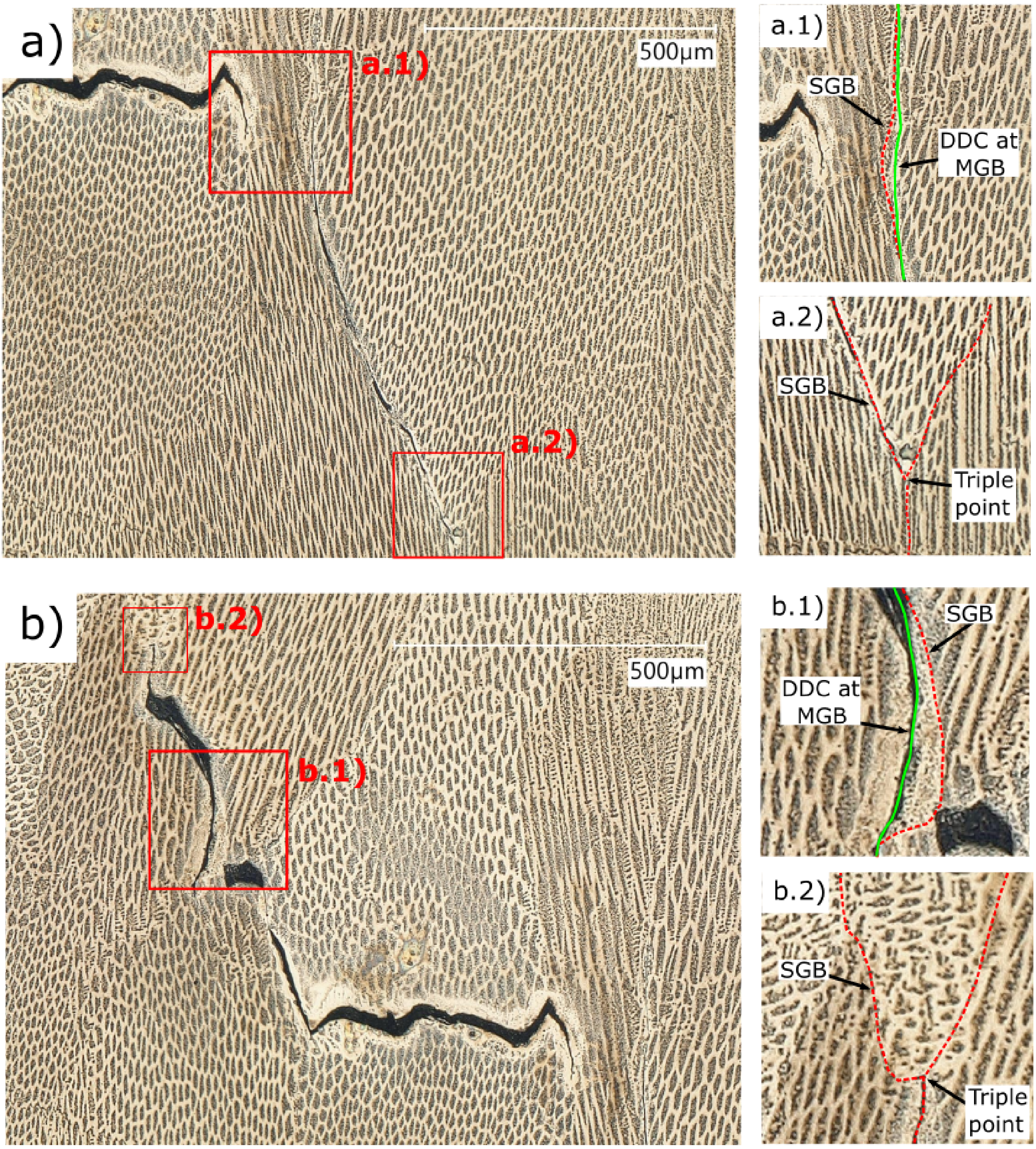

Figure 4.12: Ductility dip cracks encountered in the Invar 36 specimen inoculated with NbC-loaded suspension at 50 wt.%. (a) and (b) represent different cracks; (x.1) and (x.2) are details on MGBs and triple points.

proven to be especially susceptible to this type of cracking [89, 94]. To date, the exact mechanism responsible is still a matter of debate, current theories suggest it is a creep-like phenomenon which involves GB sliding due to thermal stresses [94, 95]. It has also been found that DDC occurs along MGBs. GB migration occurs to reduce the overall energy in the system; since the energy of a grain boundary is associated with its area, the MGBs tend to be of a straight character. Long and straight GBs are more susceptible to experiencing GB sliding, and the overall reduced GB area difficults the accommodation of thermal stresses leading to voids formation that can develop into cracking [92, 95]. Furthermore, it has also been found that triple points hinder GB sliding mechanisms and act as stress concentration sites, becoming preferential locations for initiation of ductility dip cracks [91, 95]. Modifying the GB from straight to a more tortuous character and reducing the grain size has been used as an effective DDC mitigation strategy [91–93]. Presence of impurities and second phase precipitates on the GB, pin the GB migration, hindering the tendency to become straight; the tortuous character creates a mechanical interlocking effect, impeding GB sliding, and therefore, mitigating DDC. Finer microstructures have similar effects. On one hand, the increased number of GBs due to the presence of finer grains allows to accommodate the thermal strains produced during the solidification and, at the same time, GB sliding is limited by the increased number of grains.

In chapter 4.2.2, the change in GB character from straight to tortuous, and the absence of cracks in the sample inoculated with NbC-loaded suspension at 75.% was already highlighted. During the solidification process, as already stated, NbC is segregated into the melt. Once the liquid composition reaches the eutectic composition, the remainder liquid fraction solidifies along the SGBs and SSGBs. The higher solidification rate and the formation of the eutectic constituent are responsible for the formation of a finer microstructure and pinning of the GBs. In single-phase FCC metals, DDC occurs along MGBS [80]. Therefore the effects of NbC addition, in enough quantities, are the following: (1) mitigation of solidification cracking due to reduced solid/liquid coexistence during the solidification process; (2) GB pinning due to second phase solidification resulting in DDC mitigation.

Hardness measurements

The average hardness measurement of the samples inoculated with NbC can be seen in figure 4.13. Each bar represents the average hardness calculated, and the error bars show the corresponding standard deviation. As can be seen, both specimens with added inoculants exhibit an increase in hardness. According to Sood et al. [16] grain coarsening is expected to occur for the selected heat input during the manufacturing process owing to the lower cooling rate, resulting in the Invar 36 alloy specimens experiencing elevated temperatures over prolonged amounts of time. The grain coarsening increases with the height of the deposited specimens and it was correlated to a decrease in hardness as can be observed in the reported hardness values of the reference. In this work, the grain coarsening and the reduction of hardness as a result of the aforementioned phenomenon were also observed, and showed a good correlation with the previous work. Between the two concentrations, specimens inoculated with NbC-loaded suspensions at 75 wt.% showed, with a difference of 10.0%, the largest increase in hardness. The hardness values accomplished on the aforementioned specimen are comparable with the values reported by Sood et al. [16] for the specimens manufactured with a heat input of 200 J mm^{-1}. Assuming that the microstructural changes observed do not have deleterious effects on the mechanical properties, this outcome indicates that the use of inoculants could lead to fabricating components with higher heat inputs, and thereby higher production rates, without compromising their structural integrity. A thorough study of the mechanical properties of the manufactured specimens presented in this work should be carried out to corroborate this.

The results presented are good indicators that the increase in hardness of specimens with added inoculants is most likely attributable to a combination of grain size reduction and second phase strengthening due to the FeNi-Nbc eutectic formation. EDS measurements showed the main phase is composed mostly of Fe and Ni. While it may be true that the concentration of other solute elements could lay below the detection limits of the equipment, the small difference in lattice parameters with respect to the reference (table 4.12) suggests that solid solution is not among the main mechanisms responsible for the observed change in hardness.

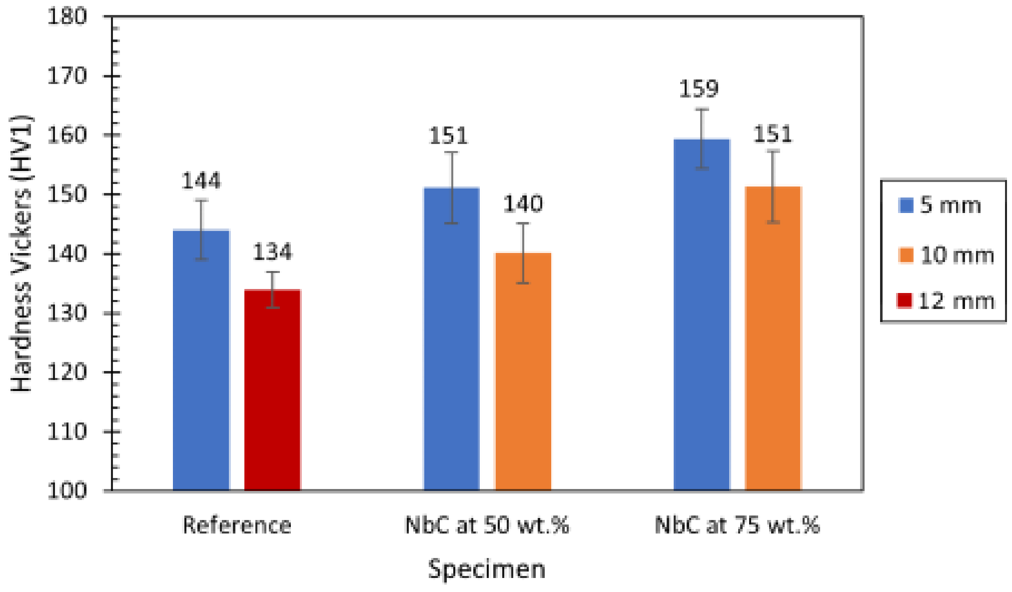

Figure 4.13: Average Hardness of Invar 36 inoculated with NbC-loaded suspensions compared to the reference sample. Reference hardness values were extracted from [16].

4.3.2. Effect of TiC addition

Solidification structure

Contrary to the samples inoculated with NbC-loaded suspensions, a first inspection of SEM imaging of specimens inoculated with TiC-loaded suspensions did not reveal any distinctive microstructural feature. Secondary electron and backscattered electron detectors revealed that the microstructure consisted of a homogeneous single phase (figure 4.14). The bright spots that can be seen on the images correspond to superficial oxides product of sample corrosion. EDS point scan measurements were performed on different grains, SGB, and the bright spots to confirm the initial observations made. The selected regions and the results can be seen in figure 4.15 and table 4.14 correspondingly. Presence of oxygen, and the absence of Ti on point scans 1, 2, and 7 confirm that the spots are superficial oxides and not TiC particles. Point scans 3, 4, and 5 show that indeed the composition is rather homogeneous. Point scan 6, taken directly on top of the SGB, shows, in addition to the Fe-Ni composition of Invar 36, the presence of Si. As explained in chapter 4.3.1 presence of Si at the GB can be attributed to solute redistribution.

Table 4.14: EDS point scan composition in wt.% from figure 4.15.

Point	Fe	Ni	Si	O
1	64.94	32.01	-	2.90
2	66.29	32.04	-	1.64
3	66.54	33.39	-	-
4	67.82	32.12	-	-
5	67.01	32.96	-	-
6	67.27	32.46	0.22	-
7	65.34	32.86	-	1.70

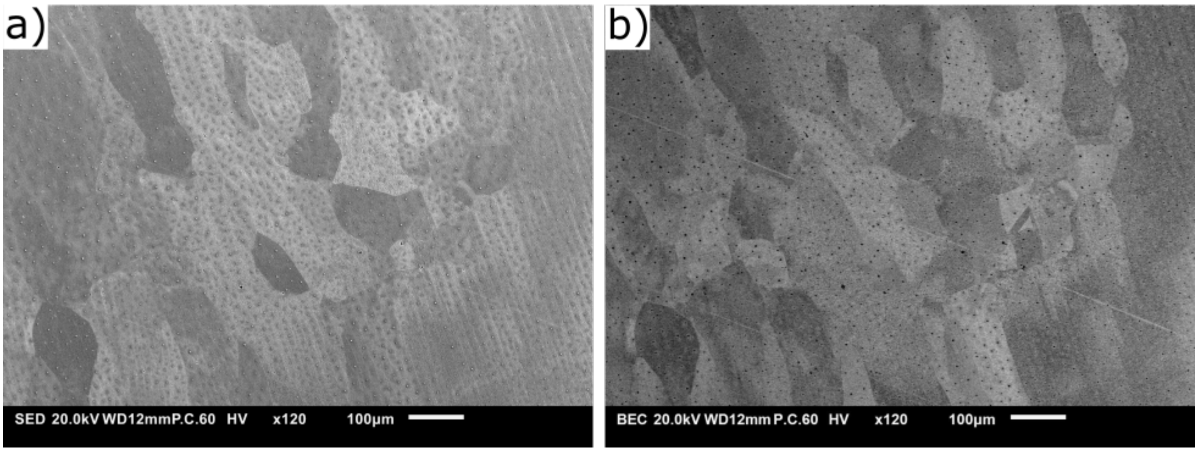

Figure 4.14: SEM images of Invar 36 inoculated with TiC-loaded suspension at 75 wt.%. (a) secondary electrons detector; (b) backscattered electrons detector.

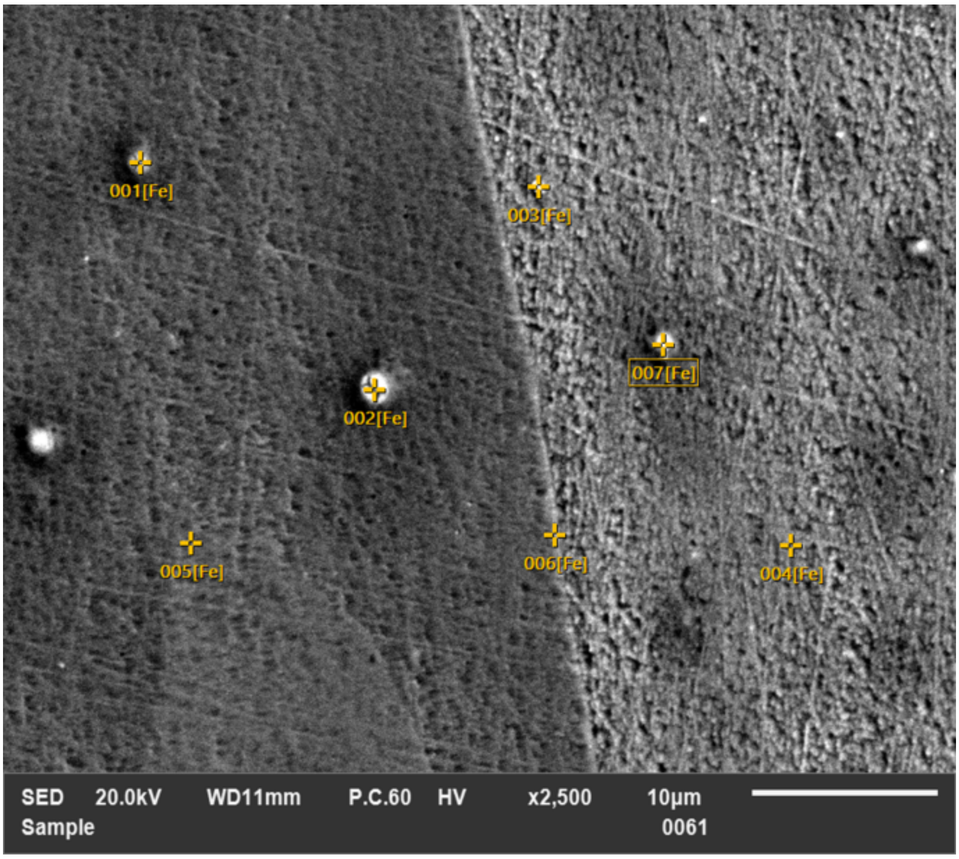

Figure 4.15: High magnification SEM images of Invar 36 inoculated with TiC-loaded suspension at 75 wt.%. Yellow markers indicate EDS point scans location.

Further inspection at high magnifications using backscattered electrons detector, to gain some deeper insight regarding the composition of the samples, was carried out [96]. Figure 4.16 depicts a series of particles encountered. The particles did not appear to have a preferential location but they were rather distributed across the entirety of the grains. Furthermore, no precipitates were found on the grain boundaries. EDS point scans were taken on the particles, the determined composition can be seen in table 4.15. Ti content, confirms that the precipitates are most likely TiC particles. While the average particle size of the added powder was 44 µm, the measured diameter of the precipitates was approximately 1 µm. It is unclear whether the reduction in size is owed to the partial dissolution of the particles or to complete dissolution and precipitation during the solidification process. The latter phenomenon has been reported by [78], however, the reported composition of the precipitates differs from the ones encountered in this study. The regions with the equiaxed grain showed no extra feature besides the ones already described. The existence of these regions could be explained by a localized increase in the TiC concentration due to a non-uniform distribution of the suspensions during its application. The higher concentration of particles could have resulted in increased heterogeneous nucleation and, thus, the formation of equiaxed grains. No particles were observed on the samples inoculated with TiC-loaded suspension at 50 wt.%. Nevertheless, given the grain size reduction, it is possible that the particle size lies below the resolution limits of the equipment.

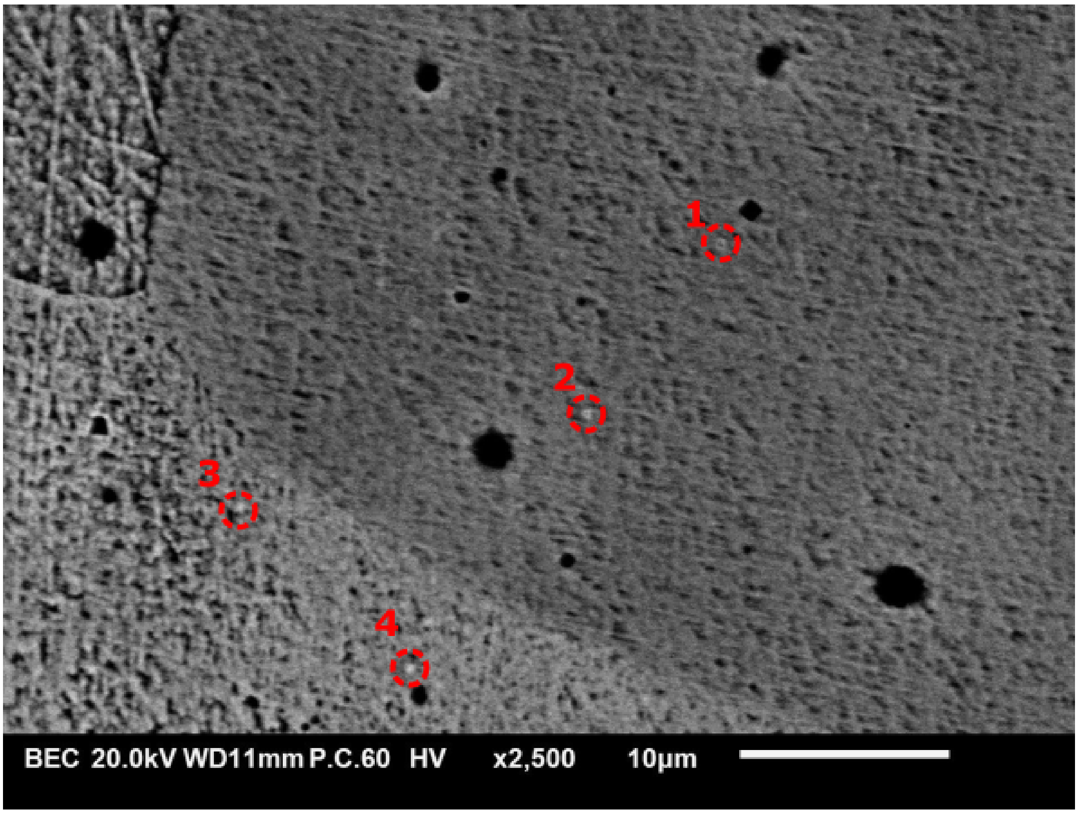

Figure 4.16: High magnification SEM backscattered electrons image of Invar 36 inoculated with TiC-loaded suspension at 75 wt.%. Red circles highlight the precipitates found.

Table 4.15: EDS point scan composition in wt.% from figure 4.16.

Point	Fe	Ni	Ti
1	63.95	34.02	1.94
2	64.11	33.05	2.69
3	61.80	34.79	3.35
4	63.35	33.69	2.87

The results from the XRF measurements can be seen in table 4.16. The average Ti concentration was 0.09±0.01% and 0.14±0.01% for specimens inoculated with 50 wt.% and 75 wt.% suspensions correspondingly. These relatively low concentrations could explain the absence of observed particles on the specimens inoculated with Tic-loaded suspension at 50 wt.%.

Table 4.16: Average composition in wt.% of Invar 36 specimens inoculated with TiC according to XRF measurements.

	TiC-loaded suspension concentration	
Element	**50 wt.%**	**75 wt.%**
Fe	63.1 ± 0.4	63.1 ± 0.4
Ni	36.0 ± 0.4	36.0 ± 0.4
Ti	0.09 ± 0.01	0.14 ± 0.01
Si	0.33 ± 0.02	0.31 ± 0.02
Mn	0.27 ± 0.02	0.34 ± 0.03
Mo	0.050 ± 0.007	0.042 ± 0.006
Cr	0.05 ± 0.01	0.07 ± 0.02
Al	0.020 ± 0.004	0.016 ± 0.004

XRD measurements showed only a single FCC structure corresponding to Invar 36 for both concentrations of TiC-loaded suspensions. The XRD spectra and the determined lattice parameters can be seen in figure 4.17 and table 4.17 accordingly. Albeit the presence of particles was detected via SEM imaging, no TiC was observed in the spectra, it is most probable that the concentration is below the detection limits of the equipment. Nevertheless, as with the specimens inoculated with NbC, no peak showed a predominant intensity, indicating that no preferential plane orientation solidification occurred. The difference in lattice parameters reported is also not significant and no extra information can be derived from it.

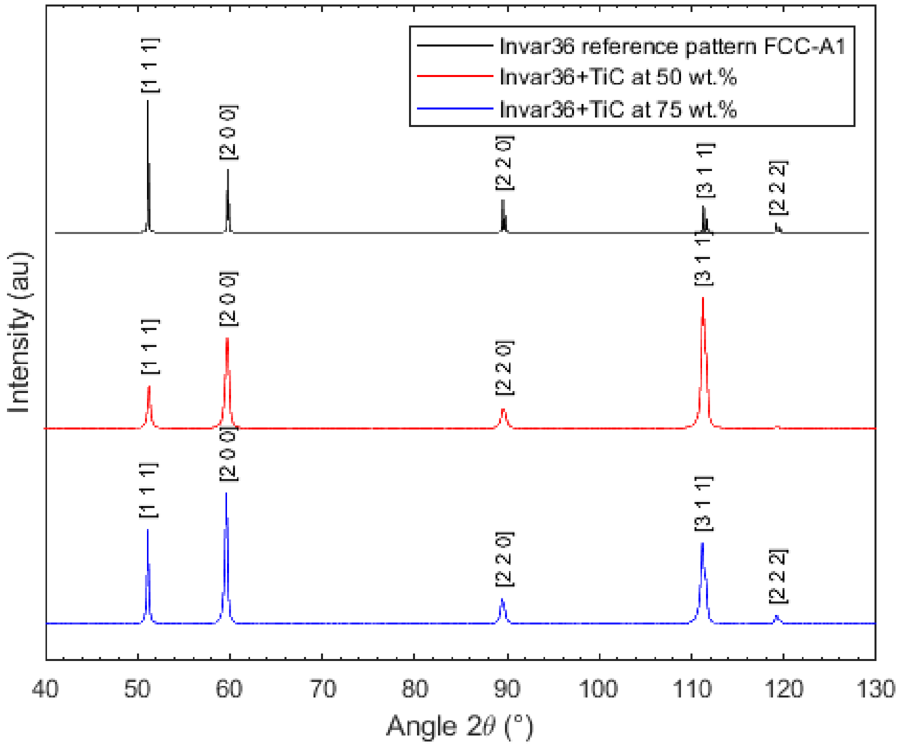

Figure 4.17: XRD spectra of Invar 36 reference pattern and specimens inoculated with TiC-loaded suspensions.

EBSD inverse pole figure map of the sample inoculated with TiC-loaded suspension at 75 wt.% is presented in figure 4.18-2. For ease of comparison, the reference sample has also been presented in the same figure (figure 4.18-1). The corresponding estimated average grain sizes can be seen in the

Table 4.17: Calculated lattice parameter for Invar 36 specimens inoculated with TiC-loaded suspensions.

Specimen	Lattice parameter [nm]
Reference	0.3592 ± 0.0006
TiC at 50 wt.%	0.3597 ± 0.0006
TiC at 75 wt.%	0.3595 ± 0.0003

table 4.18. In a similar fashion to the sample inoculated with NbC, the sample inoculated with TiC shows four distinctive regions with different grain morphologies. Given that the manufacturing specifications used were the same for both types of inoculants, the justifications regarding the different morphologies encountered in the specimen inoculated with TiC are analogous to the ones described for the specimen inoculated with NbC. The grains encountered in the regions 2.A and 2.D with lengths of 4.0 mm and 4.9 mm, and average grain areas of 0.2532 mm^2 and 0.2774 mm^2 accordingly, have a morphology ranging from slightly elongated to almost equiaxed. Interestingly enough, while a slight tortuous GB character was observed in the transverse cross section of the specimens inoculated with TiC-loaded suspension at 75 wt.%, this feature is not that clear in the EBSD inverse pole figure map presented. Some grains show certain tortuosity, while others appear to be of a straight character. Compared to the analogous regions from the reference sample, the grain size reduction in region 2.A corresponds to approximately 32% with respect to region 1.A, and the grain size reduction in region 2.D was estimated to be approximately 84% with respect to region 1.C.

The middle region of the specimen with added inoculants, the region 2.C, again exhibits an increased number of grains, and of a smaller size compared to the region 1.B in the reference sample. With a size of 3.2 mm, this region is 2.6 mm shorter than the equivalent region of the reference sample. Region 2.B of the specimen with added inoculants has a length of 1.2 mm and an average grain area of 0.0579 mm^2. This region depicts a collection of small almost equiaxed grains, similar to the ones encountered in the figure 4.10-2, and the average grain area compared to region 1.A of the reference sample is approximately 478% smaller. The presence of this region in the same location as in the specimen inoculated with NbC-loaded suspension, confirms that the manufacturing process and the methodology established for the deposition of the specimens are responsible for the formation of this grain morphology. In the case of the specimen inoculated with TiC-loaded suspension at 75 wt.% this degree of grain refinement and morphology was indeed observed in the transverse cross section (figure 4.2d). The location of the cluster of equiaxed grains on the transverse cross section corresponds to the location observed in the EBSD map presented. Lastly, while the orientation distribution maps do not depict a strong texture, some orientations seem to appear preferentially. As already mentioned, no further conclusions can be elaborated from the EBSD inverse pole figure maps alone.

While the results discussed may seem inconclusive with regard to the effects of TiC addition as an inoculant, the reduced grain size and the presence of regions with equiaxed grains are clear indicators of strong grain refinement capabilities. Compared with the samples inoculated with NbC, the effective increment in Ti content on the sample inoculated with TiC-loaded suspension at 75 wt.% is approximately 1/4 of the amount of Nb incorporated into the material from the NbC-loaded suspension of the same concentration. The presence of precipitates and their non-preferential location suggest that, in addition to solute redistribution, the refining mechanism is indeed heterogeneous nucleation as intended. The

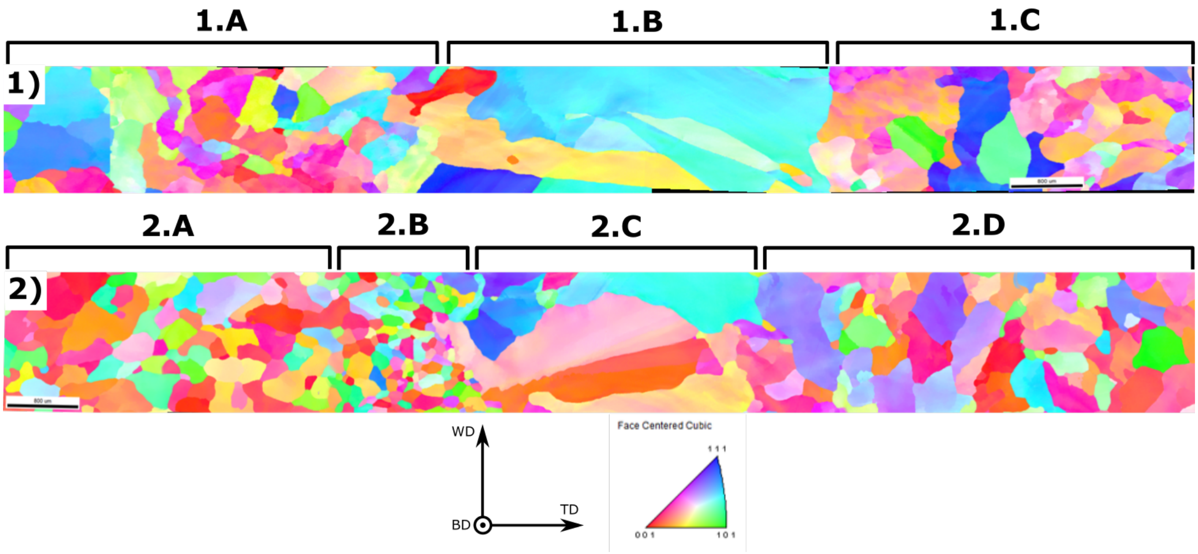

Figure 4.18: EBSD inverse pole figure map of (1) Invar 36 reference specimen and (2) Invar 36 specimen inoculated with TiC-loaded suspension at 75 wt.%. Regions denoted by the letters above the image indicate zones with different grain morphology..

Table 4.18: Estimated average grain size of the reference sample and the sample inoculated with TiC-loaded suspension at 75 wt.%. Regions indicated in the table correspond to the regions depicted in the figure 4.18.

Specimen	Region	Mean intercept [mm]	Confidence interval 95% [%]	Relative accuracy [%]	ASTM grain size [G]	Average grain area [mm^2]
REF	1.A	0.51 ± 0.05	[0.47 , 0.56]	9.3	-1.4	0.3348
	1.B	0.63 ± 0.06	[0.57 , 0.69]	9.6	-2.0	0.5045
Invar36	2.A	0.44 ± 0.04	[0.40 , 0.49]	9.7	-1.0	0.2532
+	2.B	0.21 ± 0.02	[0.20 , 0.23]	8.1	1.2	0.0579
TiC	2.D	0.47 ± 0.04	[0.42 , 0.51]	9.5	-1.1	0.2744

lack of precipitates along the grain boundaries further supports this hypothesis. Owing to the small size of the precipitates and overall low concentration of the inoculant, a more accurate description of the mechanisms involved would require the use of techniques with higher resolution power e.g. electron probe microanalysis for quantitative analysis of composition [97], and transmission electron microscope to be able to resolve the structures of the precipitates and understand, to a greater extent, the effects of the added inoculants in the structure of the matrix [98].

Crack Formation

As with NbC inoculated specimens, the cracks encountered in the specimens inoculated with TiC-loaded suspension at 50 wt.% showed indicators of ductility dip cracks. Figure 4.19 displays one of the cracks encountered. As can be seen, it is of straight character and propagates along MGB. The GB character, while it is still predominantly straight, there is a certain tortuosity that suggests GB pinning owing to the presence of precipitates (figure 4.4c). The presence of these precipitates on the GB could not be confirmed and it is believed the size and concentration of the precipitates are below the detection limits and resolution power of the techniques employed.

In contrast, no cracks were found in the samples inoculated with TiC-loaded suspension at 75 wt.%.

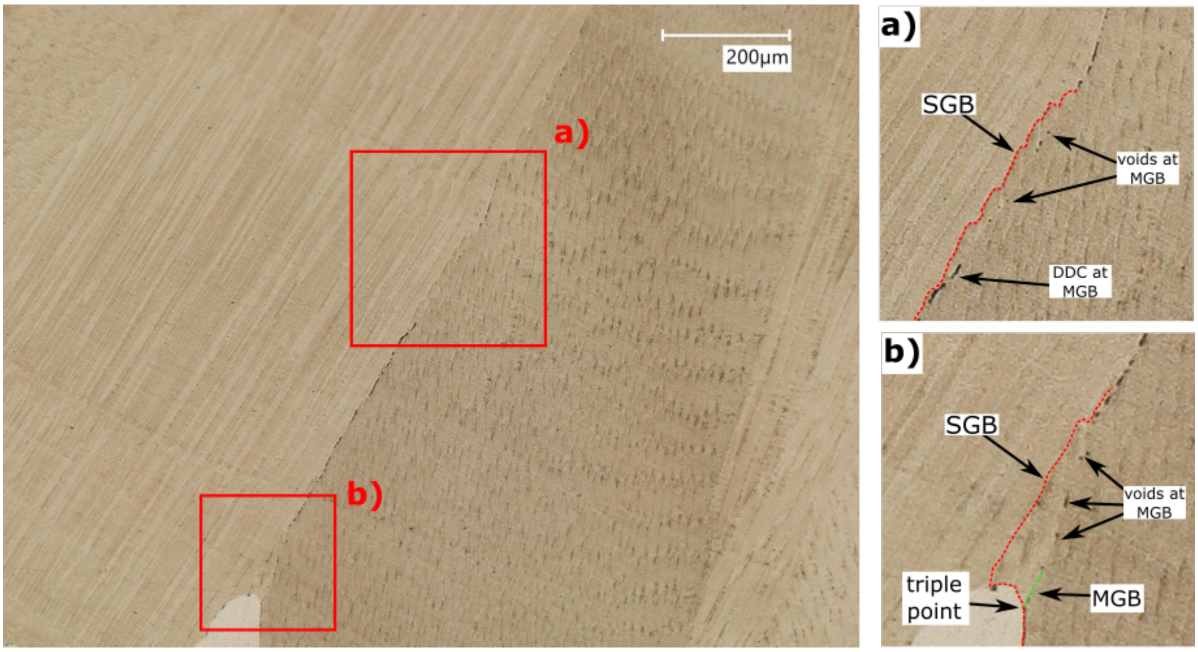

Figure 4.19: Ductility dip crack in Invar 36 inoculated with TiC-loaded suspension at 50wt.%. a) and b) are details of the crack showing the different characteristics.

The grain boundaries showed a more prominent tortuous character than samples with TiC-loaded suspension at 50 wt.% (figure 4.5d), but lower than the one observed in the sample with NbC-loaded suspension at 75wt.%. The increase in tortuous character can be explained by an increased number of precipitates due to a higher TiC concentration. Additionally, no MGBs were observed. These results lead to believe that the Ti concentration achieved of 0.14±0.01 wt.% is enough to create a number density of precipitates capable of pinning GBs. Therefore, the effect of TiC addition on crack formation is that of DDC mitigation by (1) GB pinning owing to the presence of precipitates and (2) GB sliding hindrance due to the increased number of grain GBs product of the grain refinement effect.

Hardness measurements

TiC average hardness measurements and the corresponding standard deviation compared to those of the reference specimen can be seen in figure 4.20. From the figure, it can be seen that specimens inoculated with TiC-loaded suspension at 50 wt.% depict a small increase in hardness of approximately 3.6% with respect to the reference. As with the specimens inoculated with NbC, the specimens inoculated with TiC-loaded suspension at 75 wt.% depict the highest hardness values with an increase of nearly 5.9%. The same tendency of a decrease in hardness values with an increase in the deposit height due to grain coarsening can also be appreciated. Compared to the results reported from [16], the hardness values attained with a heat input of 550 J mm^{-1} combined with the use of inoculants are comparable to the specimens manufactured with a heat input of 250 J mm^{-1}. Finally, the overall increase in hardness is slightly lower than the one accomplished by inoculating the specimens with NbC.

The similar lattice parameters (table 4.17), in addition to the EDS measurements not showing the presence of Ti on the matrix, suggest that the effect of solid solution strengthening is also not significant in the increase of the material hardness. Thereby, the increase in hardness on the specimens inoculated with TiC-loaded suspensions is most probable due to a combination of grain size reduction

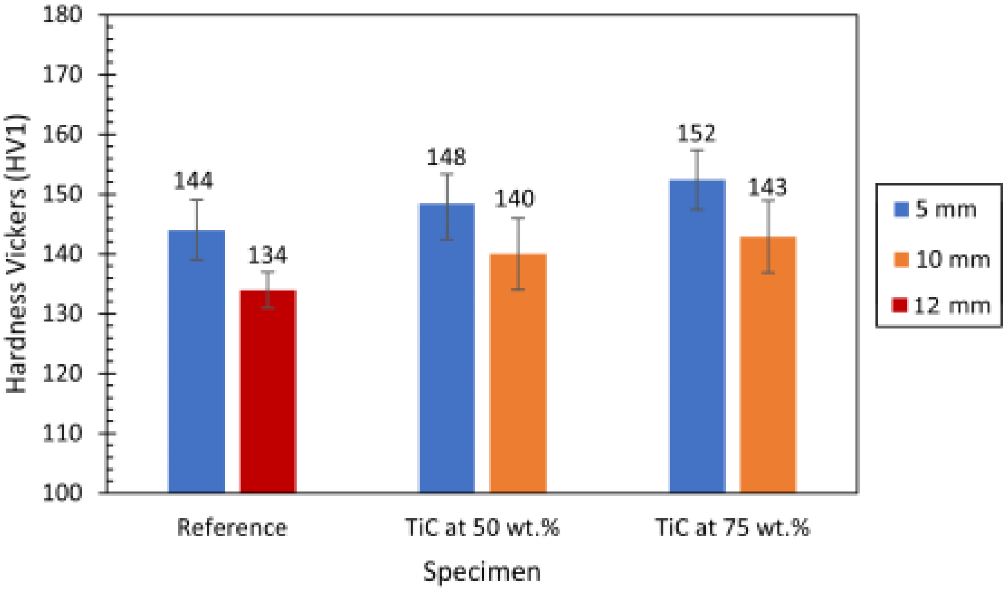

Figure 4.20: Average Hardness of Invar 36 inoculated with TiC-loaded suspensions compared to the reference sample. Reference hardness values were extracted from [16].

and hindered dislocations slip due to the presence of TiC particles [99].

5

Conclusions & future recommendations

5.1. Conclusions

In this work, the development of a script for the implementation of the E2EM model was carried out. The selection of inoculants was based on the implemented model. Invar 36 cuboidal specimens with added inoculants were deposited using GTAW-based WAAM with a heat input of 550 J mm^{-1}. The effects of the inoculant addition on the microstructure, crack formation, and hardness measurements were studied. The main conclusions, together with their corresponding research objective, are presented below.

1- Implementation of the E2EM model for the selection of possible inoculants for Invar 36.

- The script developed by combining the fundamentals of the E2EM model with the equal-ratio method for the determination of the interatomic distance showed good agreement with the results reported from the literature. The incorporation of the equal-ratio method further simplified the use of the E2EM model.
- NbC and TiC were selected as suitable inoculants according to the model implemented. For the NbC only one possible orientation relationship was identified. In contrast, six possible orientation relationships were identified for TiC. With the increased number of possible orientation relationships, TiC was identified as a more potent inoculant than NbC for Invar 36.

2- Implementation of inoculation as grain refinement strategy during the deposition of Invar 36 using GTAW-based WAAM.

- The use of an organic carrier mixed with the powders as a method for incorporating the inoculants during the deposition process did not affect the quality of the deposited specimens. The reported effects of the inoculants were consistent throughout the whole deposit, indicating that a uniform distribution of the inoculants was accomplished.

- Both inoculants, NbC and TiC, were able to induce grain refinement on the specimens deposited. The Specimens inoculated with TiC-loaded suspensions at 75 wt.% achieved the localized formation of equiaxed. The specimen inoculated with NbC-loaded suspension at 75wt.% presented the largest grain size reduction on the plane normal to the build direction.

3- Characterization of the microstructure to determine the effects of the added inoculants on the grain morphology, grain size, presence of defects, and phases present.

- Addition of NbC-loaded suspension at 75 wt.% resulted in a Nb content of 0.46 ± 0.02 on the specimens deposited. NbC was found to crystallize along the SGBs and SSGBs forming a eutectic of lamellar morphology. The findings suggest that the grain refinement mechanism was solute redistribution rather than heterogeneous nucleation.
- A change of GB character from straight to tortuous was observed and correlated to the formation of the FeNi-NbC eutectic constituent along the GBs. DDC mitigation was also observed and attributed to GB pinning due to the presence of the eutectic constituent.
- Addition of TiC-loaded suspension at 75 wt.% resulted in Ti content of 0.14 ± 0.01 on the specimens deposited. Microstructural analysis revealed the formation of a single phase with particles identified as TiC. PArticles with a size below 1 µm were found distributed across the matrix and no particles were found on the GBs. Based on the results, the refining mechanism is presumed to be a combination of solute redistribution and heterogeneous nucleation.
- A slight change in grain boundary character, from straight to tortuous, was observed on the specimens inoculated with TiC-loaded suspension at 75 wt.%. The most probable cause was GB pinning owing to the presence of precipitates. This could not be confirmed, it is believed that the concentration and size of some precipitates could have been below the detection limits of the equipment employed.
- DDC mitigation was observed in the specimens inoculated with TiC-loaded suspension at 75 wt.%. The presence of precipitates and the increase in GB tortuosity suggest that the responsible mechanism corresponds to a combination of GB pinning hindering the formation of straight MGBs and mechanical interlocking produced by the GB tortuosity.
- EBSD inverse pole figure maps showed that samples with added inoculant-loaded suspensions at 75 wt.% experienced a significant reduction in grain size, and revealed the presence of different grain morphologies across the transverse direction.
- Grain size measurements estimated, on the plane normal to the build direction, showed a grain size reduction on the sample inoculated with NbC-loaded suspension at 75 wt.% ranging from approximately 216% up to 1500% with respect to the reference sample. On the same plane, the sample inoculated with TiC-loaded suspension at 75 wt.% showed a grain size reduction ranging from approximately 32% up to 478%.

In addition to the specific conclusions above mentioned, the following general conclusions were drawn:

- With addition of inoculant-loaded suspensions at 75 wt.%, defect free depositions using a heat input of 550 J mm^{-1} were accomplished.

- Specimens inoculated with NbC-loaded suspensions showed an increase in hardness with respect to the reference sample of approximately 4.7% for the specimen with loaded suspension at 50 wt.% and 10.0% for the specimen with loaded suspension at 75 wt.%. The mechanisms for the increase in hardness were most likely a combination of grain refinement and second phase strengthening owing to the presence of the eutectic constituent.
- Specimens inoculated with TiC-loaded solutions presented an increase in hardness values, compared to the reference sample, of approximately 3.6% and 5.9% on the specimens with 50 wt.% and 75 wt.% loaded suspensions accordingly. This increase in the specimens inoculated with TiC-loaded suspensions was most probably caused by a combination of grain refinement and hindered dislocations slip caused by the presence of precipitates.

5.2. Future recommendations

The implementation of the model showed good agreement when compared with results reported by other authors. However, as it was commented in chapter 4.1, some of the values were overestimated. Further refining of the model should be performed to accurately describe the systems studied. Moreover, the solubility of the species is not accounted for in this model. Albeit part of the criteria during the selection was the thermal stability at high temperatures, the dissolution of the NbC particles and the size reduction of the TiC particles demonstrated how relevant solubility is when selecting inoculants. Future research should include methods to determine the solubility of inoculants in the substrate, either by thermodynamic modeling or direct experimentation.

Creating the inoculant-loaded suspensions proved to be a feasible and relatively easy method to incorporate the inoculants during the manufacturing process. The major limitation encountered was the difficulty in achieving concentrations higher than 75 wt.%. This could limit the amount of inoculant added to the material. For higher concentrations either the use of a different carrier that could easily incorporate higher quantities of inoculant or the use of a completely different method of incorporating the inoculants, as could be the direct projection of the inoculants into the weld pool, should be explored.

The deposition strategy employed in this work led to localized regions experiencing higher grain refinement. For future research, the use of alternative strategies such as bidirectional deposition and alternating the starting position during successive layer depositions could give rise to more homogeneous grain refinement effects throughout the whole manufactured components.

The results and effects described in this study are limited to the technique and the processing parameters. For a complete understanding of the interaction between the different process parameters, different inoculants, and different concentrations, the implementation of design of experiments (DOE) techniques is recommended.

Finally, this study focused on the effect of the added inoculants on the microstructure, crack formation, grain size, and hardness of Invar 36. As was highlighted, the main characteristic of Invar 36 is its extremely low coefficient of thermal expansion. Reports from the literature have shown that changes to the Invar composition produce different effects depending on the nature and quantity of the changes. Complementary research should be performed on the effect of the added inoculants on the thermal properties, especially on the coefficient of thermal expansion, and mechanical properties to ensure the structural integrity of components manufactured.

References

[1] ISO/ASTM International. “ISO/ASTM 52900: Additive manufacturing - General principles and Terminology”. In: *International Standard* 5.978-84-9042-335-6 (2015), pp. 1–26.

[2] X. Zhang and F. Liou. “Introduction to additive manufacturing”. In: *Additive Manufacturing*. Elsevier Inc., 2021. Chap. 1, pp. 1–31. ISBN: 9780128184110. DOI: `10.1016/b978-0-12-818411-0.00009-4`.

[3] S. A. Kumar and R. Prasad. “Basic principles of additive manufacturing: different additive manufacturing technologies”. In: *Additive Manufacturing*. LTD, 2021. Chap. 2, pp. 17–35. DOI: `10.1016/b978-0-12-822056-6.00012-6`.

[4] S. R. Singh and P. Khanna. “Wire arc additive manufacturing (WAAM): A new process to shape engineering materials”. In: *Materials Today: Proceedings* 44 (2021), pp. 118–128. ISSN: 22147853. DOI: `10.1016/j.matpr.2020.08.030`.

[5] N. A. Rosli et al. “Review on effect of heat input for wire arc additive manufacturing process”. In: *Journal of Materials Research and Technology* 11 (2021), pp. 2127–2145. ISSN: 22387854. DOI: `10.1016/j.jmrt.2021.02.002`.

[6] S. Jhavar. “Wire arc additive manufacturing: approaches and future prospects”. In: *Additive Manufacturing*. LTD, 2021, pp. 183–208. ISBN: 9780128220566. DOI: `10.1016/b978-0-12-822056-6.00004-7`.

[7] S. Singh, S. kumar Sharma, and D. W. Rathod. “A review on process planning strategies and challenges of WAAM”. In: *Materials Today: Proceedings* 47 (2021), pp. 6564–6575. ISSN: 22147853. DOI: `10.1016/j.matpr.2021.02.632`.

[8] P. Ramakrishnan. *Welding Metallurgy*. Vol. 4. 3. 1972, p. 89. ISBN: 3175723993. DOI: `10.22486/iwj.v4i3.150243`.

[9] T. Yuan, S. Kou, and Z. Luo. “Grain refining by ultrasonic stirring of the weld pool”. In: *Acta Materialia* 106 (2016), pp. 144–154. ISSN: 13596454. DOI: `10.1016/j.actamat.2016.01.016`.

[10] C. Wang et al. “Effect of heat treatment temperature on microstructure and tensile properties of austenitic stainless 316L using wire and arc additive manufacturing”. In: *Materials Science and Engineering: A* 832 (Jan. 2022), p. 142446. ISSN: 0921-5093. DOI: `10.1016/J.MSEA.2021.142446`.

[11] “Effect of ultrasonic vibration and interpass temperature on microstructure and mechanical properties of Cu-8Al-2Ni-2Fe-2Mn alloy fabricated by wire arc additive manufacturing”. In: *Metals* 10.2 (2020). ISSN: 20754701. DOI: `10.3390/met10020215`.

[12] Y. Nakamura. “The Invar Problem”. In: *IEEE Transactions on Magnetics* 12.4 (1976), pp. 278–291. ISSN: 19410069. DOI: `10.1109/TMAG.1976.1059049`.

[13] C. Qiu, N. J. Adkins, and M. M. Attallah. “Selective laser melting of Invar 36: Microstructure and properties”. In: *Acta Materialia* 103 (Jan. 2016), pp. 382–395. ISSN: 1359-6454. DOI: `10.1016/J.ACTAMAT.2015.10.020`.

[14] J. Fowler et al. “Wire-arc additive manufacturing: Invar deposition characterization”. In: *Solid Freeform Fabrication 2019: Proceedings of the 30th Annual International Solid Freeform Fabrication Symposium - An Additive Manufacturing Conference, SFF 2019* (2019), pp. 616–624.

[15] F. Veiga et al. “Wire arc additive manufacturing of invar parts: Bead geometry and melt pool monitoring”. In: *Measurement: Journal of the International Measurement Confederation* 189.June 2021 (2022), p. 110452. ISSN: 02632241. DOI: `10.1016/j.measurement.2021.110452`.

[16] A. Sood et al. “Directed energy deposition of Invar 36 alloy using cold wire pulsed gas tungsten arc welding: Effect of heat input on the microstructure and functional behaviour”. In: *Journal of Materials Research and Technology* 25 (2023), pp. 6183–6197. ISSN: 22387854. DOI: `10.1016/j.jmrt.2023.06.280`.

[17] J. Schimmel. “Deposition of Low Thermal Expansion Invar Alloys Using Wire Arc Additive Manufacturing”. MA thesis. Delft University of Technology, 2022, p. 100.

[18] C. Sreerag et al. “Additive manufacturing: a thrive for industries”. In: *Additive Manufacturing*. 2021. Chap. 1, pp. 1–16. DOI: `10.1016/b978-0-12-822056-6.00011-4`.

[19] T. Wohlers. “Developments in additive manufacturing”. In: *Manufacturing Engineering*. Vol. 144. 1. LTD, 2020. Chap. 3, pp. 37–62. ISBN: 9780128220566. DOI: `10.1016/b978-0-12-822056-6.00002-3`.

[20] O. Alheib et al. “3D bioprinting”. In: *Additive Manufacturing*. Elsevier Inc., 2021, pp. 599–633. ISBN: 9780128184110. DOI: `10.1016/b978-0-12-818411-0.00016-1`.

[21] I. Seoane-Viaño, F. J. Otero-Espinar, and Á. Goyanes. “3D printing of pharmaceutical products”. In: *Additive Manufacturing*. 2021, pp. 569–597. ISBN: 9780128184110. DOI: `10.1016/b978-0-12-818411-0.00022-7`.

[22] N. Harshavardhana. *Review on 3D printing of medical parts*. LTD, 2021, pp. 63–84. DOI: `10.1016/b978-0-12-822056-6.00005-9`.

[23] P. B.A et al. “A comprehensive review of emerging additive manufacturing (3D printing technology): Methods, materials, applications, challenges, trends and future potential”. In: *Materials Today: Proceedings* (2021). ISSN: 22147853. DOI: `10.1016/j.matpr.2021.11.059`.

[24] J. C. Vasco. *Additive manufacturing for the automotive industry*. Elsevier Inc., 2021, pp. 505–530. ISBN: 9780128184110. DOI: `10.1016/b978-0-12-818411-0.00010-0`.

[25] “Additive manufacturing using space resources”. In: *Additive Manufacturing*. 2021, pp. 661–683. ISBN: 9780128184110. DOI: `10.1016/b978-0-12-818411-0.00018-5`.

[26] C. L. Cramer et al. “Additive manufacturing of ceramic materials for energy applications: Road map and opportunities”. In: *Journal of the European Ceramic Society* (Feb. 2022). ISSN: 0955-2219. DOI: `10.1016/J.JEURCERAMSOC.2022.01.058`.

[27] P. Stavropoulos and P. Foteinopoulos. “Modelling of additive manufacturing processes: A review and classification”. In: *Manufacturing Review* 5 (2018). ISSN: 22654224. DOI: `10.1051/mfreview/2017014`.

[28] P. D. Murugan et al. “Materials Today : Proceedings A current state of metal additive manufacturing methods : A review”. In: *Materials Today: Proceedings* xxxx (2021). ISSN: 2214-7853. DOI: `10.1016/j.matpr.2021.11.503`.

[29] X. Xiong, H. Zhang, and G. Wang. “Metal direct prototyping by using hybrid plasma deposition and milling”. In: *Journal of Materials Processing Technology* 209.1 (Jan. 2009), pp. 124–130. ISSN: 0924-0136. DOI: `10.1016/J.JMATPROTEC.2008.01.059`.

[30] Hubs. *Surface finishes for CNC machining*. URL: `https://www.hubs.com/knowledge-base/surface-finishes-cnc-machinining/` (visited on 04/24/2022).

[31] Y. Huang et al. “Breaking the mould: Achieving High Volume Production Output with Additive Manufacturing”. In: *Machinery* 175.4259 (2017), pp. 45–46. ISSN: 0024919X.

[32] M. X. Zhang et al. “Crystallographic study of grain refinement in aluminum alloys using the edge-to-edge matching model”. In: *Acta Materialia* 53.5 (Mar. 2005), pp. 1427–1438. ISSN: 1359-6454. DOI: `10.1016/J.ACTAMAT.2004.11.037`.

[33] A. Queguineur et al. “Evaluation of wire arc additive manufacturing for large-sized components in naval applications”. In: *Welding in the World 2017 62:2* 62.2 (Dec. 2017), pp. 259–266. ISSN: 1878-6669. DOI: `10.1007/S40194-017-0536-8`.

[34] A. Busachi et al. “Designing a WAAM Based Manufacturing System for Defence Applications”. In: *Procedia CIRP* 37 (Jan. 2015), pp. 48–53. ISSN: 2212-8271. DOI: `10.1016/J.PROCIR.2015.08.085`.

[35] E. Brandl et al. “Additive manufactured Ti-6Al-4V using welding wire: comparison of laser and arc beam deposition and evaluation with respect to aerospace material specifications”. In: *Physics Procedia* 5.PART 2 (Jan. 2010), pp. 595–606. ISSN: 1875-3892. DOI: `10.1016/J.PHPRO.2010.08.087`.

[36] C. Buchanan and L. Gardner. “Metal 3D printing in construction: A review of methods, research, applications, opportunities and challenges”. In: *Engineering Structures* 180 (Feb. 2019), pp. 332–348. ISSN: 0141-0296. DOI: `10.1016/J.ENGSTRUCT.2018.11.045`.

[37] T. Abe and H. Sasahara. “Dissimilar metal deposition with a stainless steel and nickel-based alloy using wire and arc-based additive manufacturing”. In: *Precision Engineering* 45 (July 2016), pp. 387–395. ISSN: 0141-6359. DOI: `10.1016/J.PRECISIONENG.2016.03.016`.

[38] A. R. McAndrew et al. “Interpass rolling of Ti-6Al-4V wire + arc additively manufactured features for microstructural refinement”. In: *Additive Manufacturing* 21 (May 2018), pp. 340–349. ISSN: 2214-8604. DOI: `10.1016/J.ADDMA.2018.03.006`.

[39] D. Jafari, T. H. Vaneker, and I. Gibson. “Wire and arc additive manufacturing: Opportunities and challenges to control the quality and accuracy of manufactured parts”. In: *Materials and Design* 202 (2021), p. 109471. ISSN: 18734197. DOI: `10.1016/j.matdes.2021.109471`.

[40] A. Smith et al. “An Investigation of Creep Resistance in Grade 91 Steel through Computational Thermodynamics”. In: *Engineering* 6.6 (2020), pp. 644–652. ISSN: 20958099. DOI: `10.1016/j.eng.2019.12.004`.

[41] S. P. Tewari, A. Gupta, and J. Prakash. “Effect of Welding Parameters on the Weldability of Material”. In: *International Journal of Engineering Science and Technology* 2.4 (2010), pp. 512–516. ISSN: 0975-5462.

[42] J. Tapiola. “Cold Metal Transfer cladding of wear and corrosion resistant coatings in engine applications COLD METAL TRANSFER CLADDING OF WEAR AND CORRoSION RESISTANT COATINGS IN ENGINE APPLICATIONS”. PhD thesis. 2017, p. 149. DOI: `10.13140/RG.2.2.15573.52963`.

[43] T. A. Rodrigues et al. “Current Status and Perspectives on Wire and Arc Additive Manufacturing (WAAM)”. In: *Materials* 12.7 (2019). ISSN: 1996-1944. DOI: `10.3390/ma12071121`.

[44] M. A. Wahab. “Manual Metal Arc Welding and Gas Metal Arc Welding”. In: *Comprehensive Materials Processing*. Vol. 6. Elsevier, 2014. Chap. 6.03, pp. 49–76. ISBN: 9780080965338. DOI: `10.1016/B978-0-08-096532-1.00610-5`.

[45] W. Lucas and S. Westgate. “Welding and Soldering”. In: *Electrical Engineer’s Reference Book: Sixteenth Edition*. 2003. Chap. 10, pp. 1–51. ISBN: 9780750646376. DOI: `10.1016/B978-075064637-6/50010-1`.

[46] R. P. Martukanitz. “Directed-Energy Deposition Processes”. In: *Additive Manufacturing Processes* 24 (2020), pp. 220–238. DOI: `10.31399/asm.hb.v24.a0006549`.

[47] M. Brennan, J. Keist, and T. Palmer. “Defects in Metal Additive Manufacturing Processes”. In: *Additive Manufacturing Processes* 24 (2020), pp. 277–286. DOI: `10.31399/asm.hb.v24.a0006557`.

[48] D. Ding et al. “Wire-feed additive manufacturing of metal components: technologies, developments and future interests”. In: *International Journal of Advanced Manufacturing Technology* 81.1-4 (2015), pp. 465–481. ISSN: 14333015. DOI: `10.1007/s00170-015-7077-3`.

[49] M. M. Kirka and O. Ridge. “Additive Manufacturing of Nickel-Base Superalloys”. In: 24.c (2020). DOI: `10.31399/asm.hb.v24.a000658`.

[50] A. Sahoo and V. R. Medicherla. “Fe-Ni Invar alloys: A review”. In: *Materials Today: Proceedings* 43 (2020), pp. 2242–2244. ISSN: 22147853. DOI: `10.1016/j.matpr.2020.12.527`.

[51] C.-É. Guillaume. “Invar and elinvar”. In: *Nobel Lectures, Physics 1901-1921,* (1920), pp. 444–473.

[52] R. D. James and M. Wuttig. “Magnetostriction of martensite”. In: *Philosophical Magazine* 77.5 (2009), pp. 1273–1299. ISSN: 01418610. DOI: `10.1080/01418619808214252`.

[53] E. P. Wohlfarth. “Invar behaviour in crystalline and amorphous alloys”. In: *Journal of Magnetism and Magnetic Materials* 10.2-3 (1979), pp. 120–125. ISSN: 03048853. DOI: `10.1016/0304-8853(79)90162-8`.

[54] E. F. Wassermann. “The Invar problem”. In: *Journal of Magnetism and Magnetic Materials* 100.1-3 (1991), pp. 346–362. ISSN: 03048853. DOI: `10.1016/0304-8853(91)90828-X`.

[55] S. Chikazumi et al. “The invar problem”. In: *Journal of Applied Physics* 39.2 (1968), pp. 939–944. ISSN: 00218979. DOI: `10.1063/1.1656337`.

[56] C. Qiu, Y. Liu, and H. Liu. “Influence of addition of TiAl particles on microstructural and mechanical property development in Invar 36 processed by laser powder bed fusion”. In: *Additive Manufacturing* 48 (Dec. 2021), p. 102457. ISSN: 2214-8604. DOI: `10.1016/J.ADDMA.2021.102457`.

[57] Ansys. *Granta EduPack 2020*. version 20.1.1. Accessed on 2021-06.

[58] B. L. Bramfitt and A. O. Benscoter. “Introduction to Steels and Cast Irons”. In: *Metallographer’s Guide* (2019), pp. 1–21. DOI: `10.31399/asm.tb.mgppis.t60400001`.

[59] N. J. Harrison, I. Todd, and K. Mumtaz. “Thermal expansion coefficients in Invar processed by selective laser melting”. In: *Journal of Materials Science* 52.17 (2017), pp. 10517–10525. ISSN: 15734803. DOI: `10.1007/s10853-017-1169-4`.

[60] K. Wei et al. “Mechanical properties of Invar 36 alloy additively manufactured by selective laser melting”. In: *Materials Science and Engineering A* 772.December 2019 (2020), p. 138799. ISSN: 09215093. DOI: `10.1016/j.msea.2019.138799`.

[61] Q. Yang et al. “Microstructures and unique low thermal expansion of Invar 36 alloy fabricated by selective laser melting”. In: *Materials Characterization* 166.March (2020), p. 110409. ISSN: 10445803. DOI: `10.1016/j.matchar.2020.110409`.

[62] H. Li et al. “Microstructure evolution and mechanical properties of laser metal deposition of Invar 36 alloy”. In: *Optics and Laser Technology* 125.November 2019 (2020), p. 106037. ISSN: 00303992. DOI: `10.1016/j.optlastec.2019.106037`.

[63] Q. Tan et al. “A novel method to 3D-print fine-grained AlSi10Mg alloy with isotropic properties via inoculation with LaB6 nanoparticles”. In: *Additive Manufacturing* 32 (Mar. 2020), p. 101034. ISSN: 2214-8604. DOI: `10.1016/J.ADDMA.2019.101034`.

[64] M. X. Zhang and P. M. Kelly. “Crystallographic features of phase transformations in solids”. In: *Progress in Materials Science* 54.8 (Nov. 2009), pp. 1101–1170. ISSN: 0079-6425. DOI: `10.1016/J.PMATSCI.2009.06.001`.

[65] M. Li et al. “A New Grain Refiner for Ferritic Steels”. In: *Metallurgical and Materials Transactions B* 48 (). DOI: `10.1007/s11663-017-1101-y`.

[66] G. Langelandsvik et al. “Wire arc additive manufacturing of AA5183 with TiC nanoparticles”. In: (). DOI: `10.1007/s00170-021-08287-6`.

[67] W. Zhai, W. Zhou, and S. M. L. Nai. “Grain refinement of 316L stainless steel through in-situ alloying with Ti in additive manufacturing”. In: *Materials Science and Engineering: A* 840 (Apr. 2022), p. 142912. ISSN: 0921-5093. DOI: `10.1016/J.MSEA.2022.142912`.

[68] X. Yin et al. “Effect of tungsten particles on microstructure and properties of 316 L stainless steel manufactured by selective laser melting”. In: *Journal of Manufacturing Processes* 68 (Aug. 2021), pp. 210–221. ISSN: 15266125. DOI: `10.1016/J.JMAPRO.2021.05.039`.

[69] M. X. Zhang and P. M. Kelly. “Edge-to-edge matching and its applications: Part I. Application to the simple HCP/BCC system”. In: *Acta Materialia* 53.4 (2005), pp. 1073–1084. ISSN: 13596454. DOI: `10.1016/j.actamat.2004.11.007`.

[70] A. J. Allen and Q. Fan. “A new method of calculating interatomic spacing: the equal-ratio method”. In: *Journal of Applied Crystallography* 52.2 (Apr. 2019), pp. 289–295. ISSN: 1600-5767. DOI: `10.1107/S1600576719001018`.

[71] P. F. Fewster. *A.2 Interplanar Spacings*. 2003.

[72] M. Bermingham, S. McDonald, and M. Dargusch. “Effect of trace lanthanum hexaboride and boron additions on microstructure, tensile properties and anisotropy of Ti-6Al-4V produced by additive manufacturing”. In: *Materials Science and Engineering: A* 719 (2018), pp. 1–11. ISSN: 0921-5093. DOI: `https://doi.org/10.1016/j.msea.2018.02.012`.

[73] J. Kennedy et al. “The potential for grain refinement of Wire-Arc Additive Manufactured (WAAM) Ti-6Al-4V by ZrN and TiN inoculation”. In: *Additive Manufacturing* 40 (2021), p. 101928. ISSN: 2214-8604. DOI: `https://doi.org/10.1016/j.addma.2021.101928`.

[74] ASTM. “Standard Test Methods for Determining Average Grain Size”. In: *ASTM International E112-13* (2010), pp. 1–27. DOI: `10.1520/E0112-13R21.1.4`.

[75] Y. Yu, W. Chen, and H. Zheng. “Effects of Ti-Ce refiners on solidification structure and hot ductility of Fe-36Ni invar alloy”. In: *Journal of Rare Earths* 31.9 (2013), pp. 927–932. ISSN: 10020721. DOI: `10.1016/S1002-0721(12)60381-0`.

[76] Z. Hong-Guang, Y. Li-Jiang, and X. Heng. “Effect of two kinds of refiners on the solidification structure and property of invar alloy”. In: *High Temperature Materials and Processes* 32.4 (2013), pp. 375–381. ISSN: 03346455. DOI: `10.1515/htmp-2012-0153`.

[77] Y. C. Yu, W. Q. Chen, and H. G. Zheng. “Effect of y and Mg on the solidification structure of Fe-36Ni invar alloy”. In: *High Temperature Materials and Processes* 33.1 (2014), pp. 65–70. ISSN: 03346455. DOI: `10.1515/htmp-2013-0023`.

[78] C. Chen et al. “Refinement mechanism and physical properties of arc melted invar alloy with different modifiers”. In: *Materials Chemistry and Physics* 227.June (2019), pp. 138–147. ISSN: 02540584. DOI: `10.1016/j.matchemphys.2019.02.006`.

[79] M. G. D. V. Cuppari and S. F. Santos. “Physical Properties of the NbC Carbide”. In: *Metals* 6.10 (2016). ISSN: 2075-4701. DOI: `10.3390/met6100250`.

[80] J. C. Lippold. *Welding Metallurgy and Weldability*. Vol. 9781118230701. 2014, pp. 1–400. ISBN: 9781118960332. DOI: `10.1002/9781118960332`.

[81] M. S. Pham et al. “The role of side-branching in microstructure development in laser powder-bed fusion”. In: *Nature Communications* 11.1 (2020), pp. 1–12. ISSN: 20411723. DOI: `10.1038/s41467-020-14453-3`.

[82] A. L. da Silva, A. H. de Oliveira, and M. L. S. Fernandes. “Influence of preferred orientation of minerals in the mineralogical identification process by X-ray diffraction”. In: *2011 International Nuclear Atlantic Conference - INAC 2011* (2011), p. 11.

[83] T. Osuki, K. Ogawa, and H. Hirata. “Analysis of the solidification process in Fe–36%Ni weld metal with NbC crystallization”. In: *Welding International* 20.2 (2006), pp. 116–126. ISSN: 0950-7116. DOI: `10.1533/wint.2006.3544`.

[84] X. Zhang et al. “A three-dimensional cellular automaton model for dendritic growth in multi-component alloys”. In: *Acta Materialia* 60.5 (2012), pp. 2249–2257. ISSN: 13596454. DOI: `10.1016/j.actamat.2011.12.045`.

[85] F. Gao and Z. Fan. “Solute Effect on Grain Refinement of Al- and Mg-Alloys: An Overview of the Recent Advances Made by the LiME Research Hub”. In: *Metals* 12.9 (2022). ISSN: 20754701. DOI: `10.3390/met12091488`.

[86] X. W. Liu et al. “Columnar to equiaxed transition and grain refinement of cast CrCoNi medium-entropy alloy by microalloying with titanium and carbon”. In: *Journal of Alloys and Compounds* 775 (2019), pp. 1068–1076. ISSN: 09258388. DOI: `10.1016/j.jallcom.2018.10.187`.

[87] A. L. Greer et al. “Modelling of inoculation of metallic melts: application to grain refinement of aluminium by Al-Ti-B”. In: *Acta Materialia* 48.11 (2000), pp. 2823–2835. ISSN: 13596454. DOI: `10.1016/S1359-6454(00)00094-X`.

[88] Q. Han. “The role of solutes in grain refinement of hypoeutectic magnesium and aluminum alloys”. In: *Journal of Magnesium and Alloys* 10.7 (2022), pp. 1846–1856. ISSN: 22139567. DOI: `10.1016/j.jma.2022.01.013`.

[89] J. C. Lippold and D. J. Kocteki. “Inroduction”. In: *Welding Metallurgy and Weldability of Stainless Steels*. De Gruyter, Dec. 2000. Chap. 1, pp. 39–155. ISBN: 0471473790. DOI: `10.1515/9783110800487.39`.

[90] F. Li et al. “Interfacial microstructure and mechanical properties of Fe-36Ni invar alloy GTAW joint”. In: *Indian Journal of Engineering and Materials Sciences* 24.4 (2017), pp. 290–294. ISSN: 09751017.

[91] M. G. Collins and J. C. Lippold. “An investigation of ductility dip cracking in nickel-based filler materials - Part I”. In: *Welding Journal (Miami, Fla)* 82.10 (2003), pp. 288–295. ISSN: 00432296.

[92] T. Liu, Q. Wang, and K. Guan. “Analysis of the ductility dip cracking in the nickel-base alloy welding overlay on heat exchanger tube sheet”. In: *Engineering Failure Analysis* 147.October 2022 (2023), p. 107158. ISSN: 13506307. DOI: `10.1016/j.engfailanal.2023.107158`.

[93] A. J. Ramirez and J. C. Lippold. “High temperature behavior of Ni-base weld metal Part II - Insight into the mechanism for ductility dip cracking”. In: *Materials Science and Engineering: A* 380.1-2 (2004), pp. 245–258. ISSN: 09215093. DOI: `10.1016/j.msea.2004.03.075`.

[94] A. J. Ramirez and J. C. Lippold. “New insight into the mechanism of ductility-dip cracking in Ni-base weld metals”. In: *Hot Cracking Phenomena in Welds* Ddc (2005), pp. 19–41. DOI: `10.1007/3-540-27460-X_2`.

[95] S. J. Luther et al. “Correlation of imposed mechanical energy with ductility-dip cracking in a highly restrained weld of Alloy 52”. In: *Journal of Manufacturing Processes* 79.March (2022), pp. 767–788. ISSN: 15266125. DOI: `10.1016/j.jmapro.2022.05.027`.

[96] R. Marassi and F. Nobili. “Measurement Methods | Structural and Chemical Properties: Scanning Electron Microscopy”. In: *Encyclopedia of Electrochemical Power Sources* (2009), pp. 758–768. DOI: `10.1016/B978-044452745-5.00071-X`.

[97] X. Llovet. “Microscopy | Electron Probe Microanalysis”. In: *Encyclopedia of Analytical Science (Third Edition)*. Ed. by P. Worsfold et al. Third Edition. Oxford: Academic Press, 2019, pp. 30–38. ISBN: 978-0-08-101984-9. DOI: `https://doi.org/10.1016/B978-0-12-409547-2.14369-0`.

[98] S. Pennycook. “Transmission Electron Microscopy”. In: *Encyclopedia of Condensed Matter Physics*. Ed. by F. Bassani, G. L. Liedl, and P. Wyder. Oxford: Elsevier, 2005, pp. 240–247. ISBN: 978-0-12-369401-0. DOI: `https://doi.org/10.1016/B0-12-369401-9/00582-9`.

[99] D. Hull and D. J. Bacon. *Introduction to dislocations*. Butterworth-Heinemann, 2001.

A

Source Code E2EM model

A.1. Main routine Used

```

% the edge to edge mismatch model utilizes the interatomic distance between close
% packed rows that belong to close packed planes. It also utilizes the
% interplanar distance of relevant planes.

%beginning of the code
clear all ;
clc ;

%% Initialization of empty vectors and variables to store the relevant information
CPD= []; %close packed directions
CPP = []; %CLose packed vectors
r = 0;
d_m = [];
d_i = [];
c=0;

%% first section for the matrix
% inputs for the seleccion of the systems
disp= 'matrix parameters'
[CPD_m,CPP_m,a_m,c_m,structure]= system_selection () ;

d_m = interatomic_spacing(CPD_m,a_m,c_m,structure); % determination of the interatomic distance
p_m = interplanar_spacing(CPP_m,a_m,c_m,structure);

%% second section for the inoculat
%inputs for the seleccion of the systems

%% Initialization of empty vectors and variables to store the relevant information

disp= 'inoculant parameters'
```

```
[CPD_in,CPP_in,a_in,c_in,structure]= system_selection () ;

% determination of the interatomic and interplanar distance

d_in = interatomic_spacing(CPD_in,a_in,c_in,structure);
p_in = interplanar_spacing(CPP_in,a_in,c_in,structure);

%% mismatch determination
mismatch_dir=[];
mismatch_plane=[];

%ineratomic distance
for i = 1:length(d_m)
    for j = 1:length(d_in)

        %extra conditional to solve for double atomic spacing


        deltaI= (d_m(i)-d_in(j))/d_m(i)*100;
%         deltaII= (d_m(i)-(2*d_in(j)))/d_m(i)*100; %doubles the
%         interatomic distance of inc
        deltaII= (2*d_m(i)-(d_in(j)))/(2*d_m(i))*100; %doubles interatomic distance matrix

        if abs(deltaI) < abs(deltaII)
            delta= deltaI ;
        else
            delta=deltaII ;
        end

        mismatch_dir= [mismatch_dir,delta ];
    end
end

%interplanar distance
for i = 1:length(p_m)
   for j = 1:length(p_in)

        deltaI= (p_m(i)-p_in(j))/p_m(i)*100;
%         deltaII=(p_m(i)-(2*p_in(j)))/(p_m(i))*100;
        deltaII=(2*p_m(i)-p_in(j))/(2*(p_m(i)))*100;%double interplanar distance

%extra line to determine the misfit direction

   if abs(deltaI) < abs(deltaII)
            delta= deltaI ;
        else
            delta=deltaII ;
        end

        mismatch_plane= [mismatch_plane, delta];

    end
end

%% section to determine if the posisble directions that match the criterion are contained in the planes that match the criterion

```

```
%various necessary variables
resultsmtrx=[];
cntmtrx=0;
possible_dir=[];
possible_pln=[];

%reorganization of the data
for i = 1:height(CPD_m)
    for j = 1:height(CPD_in)
        cntmtrx=cntmtrx+1;
        resultsmtrx(cntmtrx,1:width(CPD_m))=CPD_m(i,:);
        resultsmtrx(cntmtrx,width(CPD_m)+1:width(CPD_m)+width(CPD_in))=CPD_in(j,:);
        resultsmtrx(cntmtrx,width(CPD_m)+width(CPD_in)+1)=mismatch_dir(cntmtrx); %mismatch direction
        s=width(CPD_m)+width(CPD_in)+1;
        resultsmtrx(cntmtrx,s+1:s+width(CPP_m))=CPP_m(i,:);
        resultsmtrx(cntmtrx,s+1+width(CPP_m):s+width(CPP_m)+width(CPP_in))=CPP_in(j,:);
        resultsmtrx(cntmtrx,s+width(CPP_m)+width(CPP_in)+1) = mismatch_plane(cntmtrx); %mismatch plane
        end
end

%%
possible_dir=[];
possible_pln=[];
cntdir=0;
cntpln=0;
for i = 1:height(resultsmtrx)

%This first two conditionals isolate the condition compliant results to
%determine if the directions belong to the planes.

if abs(resultsmtrx(i,s)) <= 10 %threshold for direction mismatch
        cntdir=cntdir+1;
        possible_dir(cntdir,:)= resultsmtrx(i,1:width(CPD_m)+width(CPD_in)+1);
    end

if abs(resultsmtrx(i,s+width(CPP_m)+width(CPP_in)+1)) <= 10 %threshold for plane mismatch
    cntpln=cntpln+1;
    possible_pln(cntpln,:)= resultsmtrx(i,s+1:s+width(CPP_m)+width(CPP_in)+1);
    end


end
%%
mat_dir=[];
inc_dir=[];
mat_pln=[];
inc_pln=[];
predictionmtrx=[];
cntprd=0;
for i = 1:height(possible_pln)
    for j = 1:height(possible_dir)

        mat_dir(1,:)=  possible_dir(j,1:width(CPD_m));
        inc_dir(1,:)=  possible_dir(j,width(CPD_m)+1:width(CPD_m)+width(CPD_in));
        mat_pln(1,:)=  possible_pln(i,1:width(CPP_m));
```

```
        inc_pln(1,:)=  possible_pln(i,width(CPP_m)+1:width(CPP_m)+width(CPP_in));

%with the vectors stablished, the permutator function can be called.
%this function tries the permutes among the families of planes an
%directions and determines if there is an existing direction contained in
%the plane.

        [perm_mat_dir,perm_mat_pln] = permutatorII(mat_dir,mat_pln);
        [perm_inc_dir,perm_inc_pln] = permutatorII(inc_dir,inc_pln);

if norm(perm_mat_dir) ~= 0 && norm(perm_mat_pln) ~= 0 && norm(perm_inc_dir) ~= 0 && norm(
    perm_inc_pln) ~= 0
cntprd=cntprd+1;
predictionmtrx(cntprd,:) = [perm_mat_dir,perm_inc_dir,possible_dir(j,width(possible_dir)),
    perm_mat_pln,perm_inc_pln,possible_pln(i,width(possible_pln))];
end

    end
end


%         [perm_mat_dir,perm_mat_pln] %witness to verify
%         [perm_inc_dir,perm_inc_pln]


%% section for reporting the results


%vectors to store the directions as string arrays
mat_dir= string(zeros(1,height(CPD_in)));
inc_dir= string(zeros(1,height(CPD_in)));

for h = 1:height(CPD_in)
    mat_dir(h)= string(num2str(CPD_m(h,:)));
    inc_dir(h)= string(num2str(CPD_in(h,:)));
end

%sequence to make a table
DIRMISMATCH= string();
cnt=0;
for i = 1:length(mat_dir)
    for j = 1:length(inc_dir)
        cnt=cnt+1 ;
        DIRMISMATCH(1,cnt)=mat_dir(i);
        DIRMISMATCH(2,cnt)=inc_dir(j);
        DIRMISMATCH(3,cnt)=num2str(mismatch_dir(cnt),3);
    end
end

        DIRMISMATCH;

        mat_plane= string(zeros(1,height(CPP_in)));
        inc_plane= string(zeros(1,height(CPP_in)));

for h = 1:height(CPP_in)
    mat_plane(h)= string(num2str(CPP_m(h,:)));
    inc_plane(h)= string(num2str(CPP_in(h,:)));
```

```
end

%sequence to make a table
PLANEMISMATCH= string();
cnt=0;
for i = 1:length(mat_plane)
    for j = 1:length(inc_plane)
        cnt=cnt+1 ;
        PLANEMISMATCH(1,cnt)=mat_plane(i);
        PLANEMISMATCH(2,cnt)=inc_plane(j);
        PLANEMISMATCH(3,cnt)=num2str(mismatch_plane(cnt),3);
    end
end

PLANEMISMATCH;

%% sequence to exportresults to a file


name= 'results_XX.txt';

fileID = fopen(name, 'w+');
fprintf(fileID,'Direction Mismatch\n\n');
fprintf(fileID,'%10s %10s\n' ,'MATRIX', 'INOCULANT');
fprintf(fileID, '%10s %10s %10s\n\n',DIRMISMATCH)
fprintf(fileID,'Plane Mismatch\n\n');
fprintf(fileID,'%10s %10s\n' ,'MATRIX', 'INOCULANT');
fprintf(fileID, '%10s %10s %10s\n\n',PLANEMISMATCH);
fclose(fileID);
```

A.2. Functions employed in the main routine

A.2.1. System_selection

```

function [CPD,CPP,a,c,structure]= system_selection ()

%initialization of empty variables to avoid errors
a=0;
c=0;

%relevant parameters for the different systems
CPD_BCC = [1 1 1 ; 1 1 0 ; 1 0 0 ; 1 1 3];
CPP_BCC = [1 1 0 ; 1 1 2 ; 1 2 3 ; 0 2 1 ; 1 1 1 ; 2 0 0];

CPD_FCC_NACL = [1 0 0 ; 1 1 0 ; 1 1 1];
CPP_FCC_NACL = [2 0 0 ; 2 2 0 ; 1 1 1];

CPD_FCC = [ 1 1 0 ; 1 0 0 ; 1 1 2];
CPP_FCC = [  1 1 1 ;2 0 0 ; 2 2 0] ;

% CPD_HCP = [1 1 -2 0 ; 0 0 0 1 ; 1 1 -2 3 ; 1 0 -1 0]; %Miller Bravais
CPD_HCP = [1 1 0 ; 0 0 1 ; 1 1 1 ; 2 1 0 ]; %Miller

% CPP_HCP = [1 0 -1 1 ; 1 0 -1 0 ; 0 0 0 1 ; 1 1 -2 0]; %Miller Bravais
```

```
CPP_HCP = [1 0 1 ; 1 0 0 ; 0 0 1 ; 1 1 0 ]; %Miller

txt= ('Indicate the crystalline structure 1 = FCC , 2 = BCC , 3 = HCP , 4 = rocksalt ');
txt2= ('Enter the lattice parameter "a" in nm ');
txt3= ('Enter the lattice parameter "c" in nm ');

structure = input(txt) ;

if structure == 1
  CPD = CPD_FCC ;
  CPP = CPP_FCC ;

  a = input (txt2);

elseif structure == 2
  CPD = CPD_BCC ;
  CPP = CPP_BCC ;

  a = input (txt2);

elseif structure == 4

  CPD = CPD_FCC_NACL ;
  CPP = CPP_FCC_NACL ;

  a = input (txt2);

elseif structure == 3 %change to an elseif when the other statements are in

    CPD = CPD_HCP ;
    CPP = CPP_HCP ;

    a = input (txt2);
    c = input (txt3);
end
```

A.2.2. Interatomic_spacing

```
function [d]= interatomic_spacing (CPD,a,c,structure)

%as in the system selection, tehre are some differences between different
%structures regarding how to determine the parameter r and the proper
%distance between atoms.

%% determination of the interatomic distance

d= [] ; %empty vector to store the values

%initiates with an if statement to determine the proper structure

if structure == 1 %FCC

    for i = 1:height(CPD)
    cnt=0 ; %counter reset
    for j = 1:width(CPD)

```

```
        if rem(CPD(i,j),2)== 0
            cnt=cnt+1;
        end
    end

        if cnt == 1
            r = 2;
        else
            r = 1;
        end

        u = CPD(i,1);
        v = CPD(i,2);
        w = CPD(i,3);

    d_i = sqrt(u^2+v^2+w^2)*a*(1/r) ;

    d= [d , d_i];

    end
end

 if structure == 2 %BCC

    for i = 1:height(CPD)
    cnt=0 ; %counter reset
    for j = 1:width(CPD)

        if rem(CPD(i,j),2)== 0
            cnt=cnt+1;
        end
    end

        if cnt ~= 0
            r = 1;
        else
            r = 2;
        end

        u = CPD(i,1);
        v = CPD(i,2);
        w = CPD(i,3);

    d_i = sqrt(u^2+v^2+w^2)*a*(1/r) ;

    d= [d , d_i];

    end

elseif structure == 3 %HCP

for i = 1:height(CPD)

        u = CPD(i,1);
        v = CPD(i,2);
        w = CPD(i,3);

```

```
A= [6 0 0 ; 0 6 0 ; 0 0 6];
B1= [u-4 ; v-2 ; w-3];
B2= [u-2 ; v-4 ; w-3];

XI=linsolve(A,B1);
XII=linsolve(A,B2);

if norm(XI)==0 || norm(XII)==0
r=6;
else
r=1;
end

d_i = sqrt(((u^2+v^2-u*v)*a^2)+(w^2*c^2)) *(1/r) ;

    d= [d , d_i];


end





elseif structure == 4 %FCC rocksalt

    for i = 1:height(CPD)
    cnt=0 ; %counter reset
    for j = 1:width(CPD)
%
        if rem(CPD(i,j),2)~= 0
            cnt=cnt+1;
        end
    end
%
%         if cnt == 1 %this portion is used wheter the atomic direction
%         contemplates both atoms.
%             r = 1;
%         else
%             r = 2;
%         end
        r=2;
        u = CPD(i,1);
        v = CPD(i,2);
        w = CPD(i,3);

    d_i = sqrt(u^2+v^2+w^2)*a*(1/r) ;


    d= [d , d_i];

    end

end
```

A.2.3. Interplanar_spacing

```
function [p] = interplanar_spacing(CPP,a,c,structure)

p = [] ; %vector for storage of distances

if structure == 3

       for i = 1:height(CPP)

        u = CPP(i,1);
        v = CPP(i,2);
        w = CPP(i,3);

    p_i = sqrt(1/(((4/3)*(u^2+v^2+u*v)/(a^2))+(w^2/c^2)));
          p= [p, p_i];
       end

elseif structure == 1 || structure==2 || structure==4

     for i = 1:height(CPP)

        u = CPP(i,1);
        v = CPP(i,2);
        w = CPP(i,3);

%      d_i = sqrt(u^2+v^2+w^2)*a*(1/r) ;

        p_i = a/sqrt(u^2+v^2+w^2);
        p= [p , p_i];


     end





end
end
```

A.2.4. PermutatorII

```
function [rslt_dir,rslt_pln]=permutatorII(dir,pln)

cnt=0; %counters
cntI=0;
y=0;%similar variable to Z to add an extra counter
for i = 1:factorial(length(pln))+1

     pln_i=pln;%reset of the vector for each loop
    if cntI == 0
        pln_i;
    elseif cntI <= length(pln)
        pln_i(i-1)=-pln_i(i-1);
        pln_i;
```

```
    elseif cntI > length(pln) && cntI < factorial(length(pln))
                pln_i(i-cntI)=-pln_i(i-cntI);
        pln_i(i-cntI+1+y)=-pln_i(i-cntI+1+y);
        y=y+1;
        pln_i;
    elseif cntI == factorial(length(pln))
        pln_i=-pln ;
    end
    cntI=cntI+1;

     z=0; %additional counter to set the last condition for the direction
     cnt=0; %counter reset for succesive iterations
    for j = 1:factorial(length(dir))+1

    dir_i=dir;%reset of the vector for each loop
    if cnt == 0
        dir_i;
    elseif cnt <= length(dir)
        dir_i(j-1)=-dir_i(j-1);
        dir_i;
    elseif cnt > length(dir) && cnt < factorial(length(dir))
                dir_i(j-cnt)=-dir_i(j-cnt);
        dir_i(j-cnt+1+z)=-dir_i(j-cnt+1+z);
        z=z+1;
        dir_i;
    elseif cnt == factorial(length(dir))
        dir_i=-dir ;

    end
    cnt=cnt+1;
%     end %remove
% end %remove
%     Once for each iteration we get the perutations and calculate the dot
%     product

    perm_dir=perms(dir_i);
    perm_pln=perms(pln_i);

%     double loop to determine the dot product
    for k = 1:height(perm_pln)
        for l = 1:height(perm_dir)

        dotproduct=dot(perm_pln(k,:),perm_dir(l,:));

        if dotproduct == 0
        rslt_dir=perm_dir(l,:);
        rslt_pln=perm_pln(k,:);
        return
        end
        end
    end

    end %uncomment later
end %uncomment later

if dotproduct ~= 0 %if it is not contained then return only a vector with zeroes.
rslt_dir=zeros(1,length(dir));
```

```
rslt_pln=zeros(1,length(pln));
end

end %for the function
```